

MELT PRODUCTION AND RIDGE GEOMETRY OVER THE PAST 10 MYR ON  
THE SOUTHERN KOLBEINSEY RIDGE, ICELAND

by

ALI VALETTA FURMALL

A THESIS

Presented to the Department of Geological Sciences  
and the Graduate School of the University of Oregon  
in partial fulfillment of the requirements

for the degree of  
Master of Science

March 2010

“Melt Production and Ridge Geometry Over the Past 10 Myr on the Southern Kolbeinsey Ridge, Iceland,” a thesis prepared by Ali Valetta Furmall in partial fulfillment of the requirements for the Master of Science degree in the Department of Geological Sciences.

This thesis has been approved and accepted by:

---

Eugene Humphreys, Chair of the Examining Committee

*March 9, 2010*  
Date

Committee in Charge: Eugene Humphreys, Chair  
Emilie Hooft  
Mark Reed

Accepted by:

---

Dean of the Graduate School

© 2010 Ali Valetta Furmall

## An Abstract of the Thesis of

Ali Valetta Furmall for the degree of Master of Science

in the Department of Geological Sciences to be taken March 2010

Title: MELT PRODUCTION AND RIDGE GEOMETRY OVER THE PAST 10 MYR  
ON THE SOUTHERN KOLBEINSEY RIDGE, ICELAND

Approved: \_\_\_\_\_  
Emilie Hooft

Excess melt production due to the interaction between the northern Mid-Atlantic Ridge and the Iceland mantle plume generates anomalously thick oceanic crust. Observed V-shaped gravity anomalies on the Reykjanes Ridge south of Iceland are inferred to reflect changes in melting with a periodicity of 5-6 Ma. A 2-D tomographic inversion of travel times recorded on a seismic refraction line on the Kolbeinsey Ridge north of Iceland constrains crustal velocity and Moho depth. I do not find increased melt production on a 5-6 Ma period, but with a period of ~8-9 Ma, with Moho depth varying from  $7.8 - 12.5 \pm 0.5$  km. Unlike the Reykjanes Ridge, the thickest crust does not correspond with a high gravity anomaly. However, it is a region of slow *p-wave* velocities and significant decay of magnetic signal. I interpret the V-shaped anomaly in this region to record the northward migration of a ridge segment offset.

## CURRICULUM VITAE

NAME OF AUTHOR: Ali Furmall

PLACE OF BIRTH: Louisville, KY

DATE OF BIRTH: June 12, 1972

## GRADUATE AND UNDERGRADUATE SCHOOLS ATTENDED:

University of Oregon, Eugene, Oregon

University of South Florida, Tampa, Florida

## DEGREES AWARDED:

Master of Science, Geological Sciences, March, 2010, University of Oregon

Bachelor of Science, Geology, August, 2007, University of South Florida

## AREAS OF SPECIAL INTEREST:

## Seismology

I am particularly interested in the application of seismic methods to constrain variations in crustal structure.

## Convergent margin dynamics

How variability in oceanic crustal geometry contributes to changes in the geometry and behavior of subduction zones.

## PROFESSIONAL EXPERIENCE:

Graduate Teaching Fellow, University of Oregon, 2007 - 2009

## ACKNOWLEDGMENTS

I would like to express my immense gratitude to Emilie Hooft for her unfailing support and patience during the completion of this project. In addition, I would like to thank Gene Humphreys, Mark Reed, Doug Toomey, and Ray Weldon for sharing their expertise in their respective fields. Bryndís Brandsdóttir of the University of Iceland has been an indispensable resource in developing my understanding of the history of the interaction between the Iceland plume and the adjacent ridges.

The extensive data processing necessary for this project was enabled by the computing facility purchased with support of National Science Foundation award number EAR-0651123. I offer my sincerest gratitude to Craig Thornley, both for keeping the computing cluster operational, and for always finding a solution to any problem I brought to him.

I would also like to thank USF professors Len Vacher, Chuck Connor, Paul Wetmore, Peter Harries, and Diana Roman for their guidance and encouragement during my undergraduate studies. They were all instrumental in fostering my curiosity about geologic processes and my decision to pursue a graduate degree.

I offer my greatest measure of gratitude to my family and friends. Their support and levity make all things possible.

I would like to dedicate this manuscript to my mother,  
for showing me that new beginnings can be found around any corner.

## TABLE OF CONTENTS

| Chapter   | Page |
|---|------|
| I. INTRODUCTION .....   | 1    |
| Section 1.1 The Kolbeinsey Ridge Iceland Seismic Experiment ..... | 1    |
| Section 1.2 Oceanic Crust Generation .....                        | 3    |
| Section 1.3 Regional History .....                                | 6    |
| Section 1.4 Plume-Ridge Interaction .....                         | 8    |
| Section 1.5 V-shaped Ridges .....                                 | 10   |
| II. PREVIOUS STUDIES OF TEMPORAL CHANGES IN PLUME                 |      |
| INFLUENCED RIDGE NORTH AND SOUTH OF ICELAND.....                  | 16   |
| Section 2.1 Smallwood and White (1998).....                       | 16   |
| Section 2.2 Kodaira et al (1997).....                             | 19   |
| III. METHODS .....  | 21   |
| Section 3.1 Experiment Details - Instrumentation.....             | 21   |
| Section 3.2 Data Analysis.....                                    | 23   |
| Seismic.....  | 23   |
| Inversion Details.....  | 31   |
| Gravity Data.....   | 34   |
| Magnetic Data.....  | 36   |



| Chapter   | Page |
|---|------|
| IV.RESULTS .....  | 39   |
| Section 4.1 Seafloor Details.....                             | 39   |
| Section 4.2 Crustal Thickness.....                            | 43   |
| Section 4.3 Velocity Model .....                              | 46   |
| Section 4.4 Gravity Inversion .....                           | 56   |
| Section 4.5 Magnetic Signal .....                             | 57   |
| V. DISCUSSION .....   | 62   |
| Section 5.1 Crustal Velocity Structure.....                   | 62   |
| Section 5.2 Topographic Support .....                         | 69   |
| Section 5.3 V-shaped Ridges .....                             | 72   |
| Section 5.4 Melt Flux Associated With Crustal Thickness ..... | 79   |
| Section 5.5 Non-transform Offsets .....                       | 80   |
| VI. CONCLUSION.....   | 84   |
| REFERENCES .....  | 88   |

## LIST OF FIGURES

| Figure  | Page |
|---|------|
| 1.1. Bathymetric and topographic map of the North Atlantic .....                    | 4    |
| 1.2. Bathymetry and magnetics of the Kolbeinsey Ridge .....                         | 9    |
| 1.3. Gravity anomalies north and south of Iceland.....                              | 13   |
| 1.4. Magnetic anomalies north and south of Iceland.....                             | 14   |
| 1.5. Short-wavelength component of satellite gravity field .....                    | 15   |
| 2.1. Smallwood and White (1998) experiment geometry .....                           | 17   |
| 2.2. Final velocity models for Smallwood and White's CAM 72 and CAM 74 .....        | 18   |
| 2.3. Magnetic anomalies and crustal velocities along Kodaira et al's L3 transect... | 20   |
| 3.1. Bathymetric and topographic map of the Kolbeinsey Ridge .....                  | 22   |
| 3.2. Record section from OBS 15.....  | 24   |
| 3.3. Record sections from OBS 16 and OBS 17 .....                                   | 25   |
| 3.4. Record sections from OBS 18 and OBS 20 .....                                   | 26   |
| 3.5. Record sections from OBS 21 and OBS 22 .....                                   | 27   |
| 3.6. A portion of the record sections from OBS 15 and OBS 17 .....                  | 28   |
| 3.7. A portion of the record sections from OBS 20 and OBS 21 .....                  | 29   |
| 3.8. Starting velocity-depth profile.....   | 33   |
| 3.9. Starting 2-D velocity model, sheared according to bathymetry .....             | 33   |
| 3.10. Simple crustal density model used for gravity prediction .....                | 35   |

| Figure   | Page |
|--|------|
| 3.11. Maps of magnetic lineations based on the 2004 geomagnetic polarity timescale.....  | 38   |
| 4.1. Bathymetry and reflection profile .....   | 40   |
| 4.2. Comparison of the final Moho depth from two inversions with different starting Moho depths .....  | 44   |
| 4.3. Final Moho topography .....   | 45   |
| 4.4. Final velocity model and velocity perturbations using only <i>Pg</i> arrivals.....  | 47   |
| 4.5. Contours of standard deviation of average velocity model.....   | 48   |
| 4.6. Final 2-D velocity model with free air gravity and bathymetry.....  | 49   |
| 4.7. Perturbations to the starting velocity model, with free air gravity and bathymetry .....  | 50   |
| 4.8. Final velocity model created by averaging the five best-fitting results, with select rays .....   | 51   |
| 4.9. Travel time residuals for final velocity model .....  | 52   |
| 4.10. Starting velocity model used for <i>Pn</i> inversion .....   | 55   |
| 4.11. Observed and predicted gravity.....  | 59   |
| 4.12. Gravity anomalies.....   | 60   |
| 4.13. Observed magnetic anomalies on the southern Kolbeinsey Ridge plotted over two magnetic models created with different spreading rates ..... | 61   |
| 5.1. Plot of change in velocity with depth for final velocity model.....   | 63   |

| Figure  | Page |
|---|------|
| 5.2. The 2-D velocity model with gravity and bathymetry for 200 km of<br>Kodaira et al's L3 transect on the northern Kolbeinsey Ridge ..... | 66   |
| 5.3. The 2-D velocity model with gravity and bathymetry for Smallwood<br>and White (1998) CAM 72 .....                                      | 67   |
| 5.4. The 2-D velocity model with gravity and bathymetry for Smallwood<br>and White (1998) CAM 74 .....                                      | 68   |
| 5.5. Observed, predicted, and anomalous bathymetry .....  | 70   |
| 5.6. Crustal thickness predicted from bathymetry and crustal velocity .....   | 70   |
| 5.7. Gravity anomalies on the Kolbeinsey Ridge .....  | 74   |
| 5.8. A schematic model for plume behavior beneath Iceland and the<br>adjacent ridges .....  | 75   |
| 5.9. Tectonic reconstruction of the Kolbeinsey Ridge segments over the<br>last 10 Ma .....  | 76   |
| 5.10. Gravity anomalies on the Kolbeinsey Ridge with the angle between<br>the ridge and the V-shaped features highlighted .....             | 78   |
| 5.11. Magnetic anomalies on the Kolbeinsey Ridge .....  | 82   |

## LIST OF TABLES

| Table   | Page |
|---|------|
| 3.1 OBS locations showing original (drop) and adjusted location .....   | 31   |
| 4.1 Details of five best fitting models that were used to create the final<br>average 2-D model of crustal thickness and velocity ..... | 45   |

## CHAPTER I

### INTRODUCTION

#### **Section 1.1 The Kolbeinsey Ridge Iceland Seismic Experiment**

Mantle plume interaction with nearby mid-oceanic spreading centers affects both the melt production at the ridge and the geometry of the spreading axis (Hooft et al, 2006; Smallwood and White, 1998; Abelson and Agnon, 2001). This project addresses whether the Iceland mantle plume interaction with the Mid-Atlantic Ridge (MAR) has varied through time to the north of the plume source. Off axis oceanic crustal thickness is a measure of melt production at a mid-ocean ridge at the location and time of crustal generation (White et al, 1992). Interaction of the MAR with the Iceland mantle plume has resulted in a broad platform (Iceland) with crustal thickness  $>30$  km as well as the generation of thicker than average oceanic crust at both the Kolbeinsey and Reykjanes Ridges, north and south of Iceland, respectively (Hooft et al, 2006; Smallwood and White, 1998; Weir et al, 2001). Topography and basalt lava compositions indicate an asymmetry in plume influence, with a greater proportion of the plume material being

diverted south to the Reykjanes (Hooft et al, 2006; Mertz et al, 1991). Variations in oceanic crustal thickness in excess of 2 km are thought to be the result of fluctuations in influence of the plume on melting in the upper mantle. This fluctuation in plume material supplied to the spreading center may be due to a change in the flux of material from the plume's source (Jones et al, 2002) or due to impairment of the plume material's access to the crust due to lithospheric reorganization (Hardarson et al, 1997). The variation in melt flux generated by the plume may be attributed to temperature or compositional variations in the plume stem over time (Jones et al, 2002).

The Kolbeinsey Ridge Iceland Seismic Experiment (KRISE) was performed to constrain temporal variations in thickness of oceanic crust generated on the southern Kolbeinsey Ridge section of the Mid-Atlantic Ridge system. KRISE featured three transects north of Iceland: two that are nearly perpendicular to the spreading axis, Line 4 and Line 7, and one parallel to the ridge, Line 1 (**Figure 1.1**). I present here the results of Line 4; results from Line 1 have been previously published in Hooft et al (2006). I compare these results to previous seismic refraction and reflection experiments on the northern Kolbeinsey Ridge and the Reykjanes Ridge south of Iceland (discussed below). This work will address variability in the nature of plume-ridge interaction and will lend insight into the dynamics of crust generation in this region.

## Section 1.2 Oceanic crust generation

The generation of new crust at oceanic spreading centers is the result of continuous separation of tectonic plates. This separation leads to partial decompression melting and upwelling of the underlying mantle. While the mechanisms of melt delivery to the crust are still under investigation, and appear to vary in different ridge systems, it is accepted that this partial melt of mantle material cools shallowly to form new oceanic crust. As a consequence, the thickness of oceanic crust reflects the amount of melt delivered.

Typical oceanic crust is a combination of extrusive and intrusive materials. The upper oceanic crust is typically comprised of lava flows and pillow basalts, although portions of some slow and very slow spreading ridges appear to lack volcanic rocks. This extrusive layer, referred to as seismic layer 2A, is typically a few hundred meters thick and has a low *p-wave* velocity,  $< 2.5$  km/s in zero age crust near the surface, and 10-30% porosity due to voids and fractures. As the crust ages and moves away from the spreading axis, *p-wave* velocities increase due to the closure of fractures by compaction and precipitation of hydrothermal minerals. There is a steep velocity gradient in layer 2A with velocities increasing to  $\sim 5$  km/s within only a few hundred meters (Carbotte and Scheirer, 2004). Below the extrusive layer is a zone of sheeted dikes that serve as the mechanism of transport of magma through the crust. This intrusive layer, seismic layer 2B, has low porosity and higher *p-wave* velocities than layer 2A. It may extend to 2-3 kilometers depth and is characterized by a moderate velocity gradient from  $\sim 5 - 6.5$  km/s.



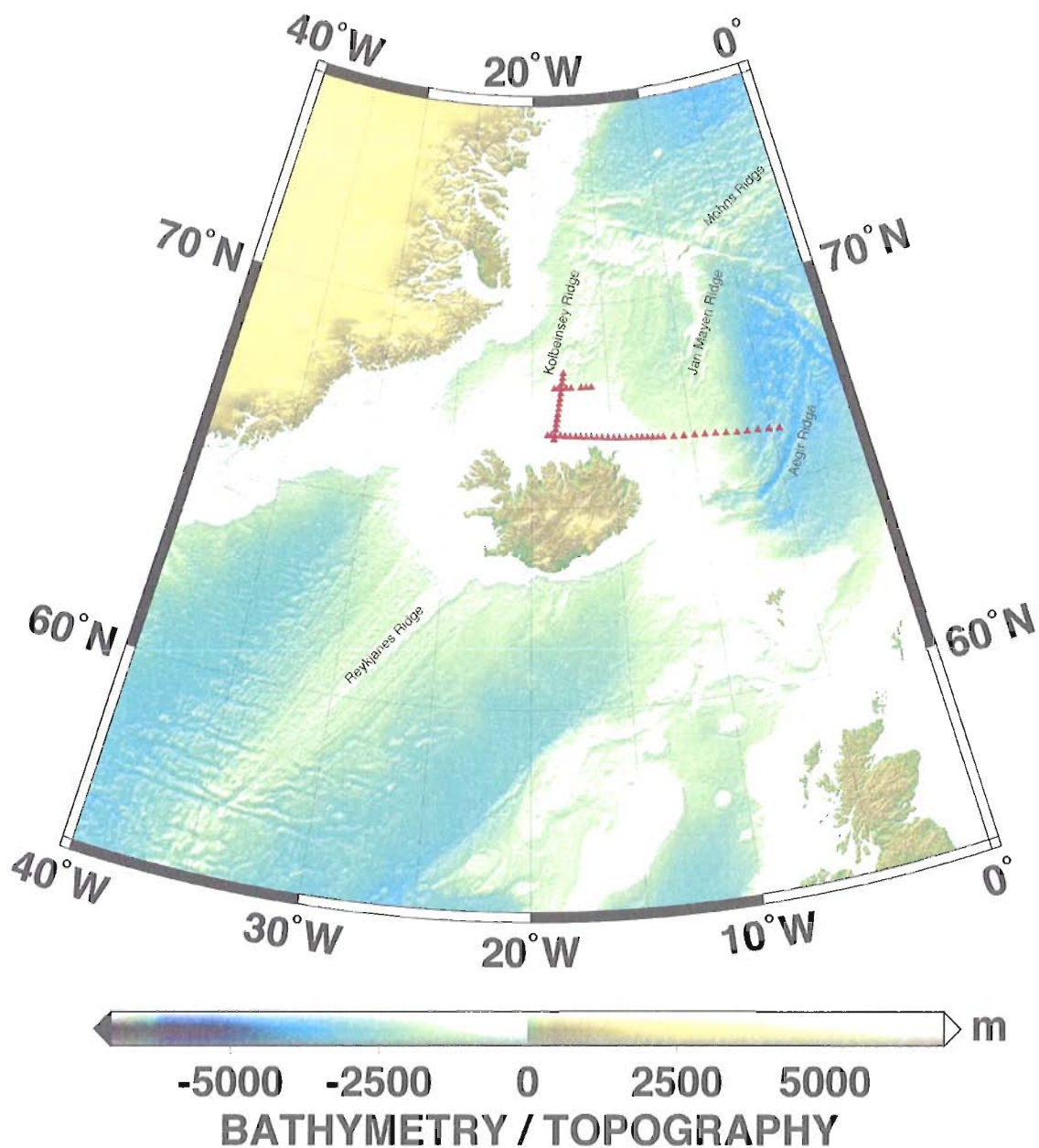


**Figure 1.1:** Bathymetric and topographic map of the North Atlantic. KRISE OBS (ocean bottom seismometer) locations are shown as red triangles. The currently spreading Reykjanes, Kolbeinsey, and Mohr's sections of the Mid-Atlantic Ridge are labeled. Prior to the inception of the Kolbeinsey Ridge, spreading between Iceland and the Mohr's Ridge was accommodated on the now-extinct Aegir Ridge.

Below layer 2B, seismic layer 3 features a change to a low velocity gradient beginning in the mid-crust and extending to the base of the crust, with velocities ranging from ~6.5 – 7.2 km/s.

The boundary between layer 2 and 3 has traditionally been attributed to a transition from a predominance of sheeted dikes to gabbroic rocks, however some workers associate it with a change in metamorphic grade within the dikes (Carlson and Herrick, 1990) or to the depth limit of hydrothermal cracking (Shaw, 1994). Observations in various locations suggest that the seismically recognized transition between layer 2 and 3 does not always correlate with the mechanical transition from dikes to gabbro (Christeson et al, 1996).

The transition from crust to upper mantle is usually recognized by a sharp jump in *p-wave* velocity from ~7.2 to 8 km/s or more. This sharp transition results in a reflected *p-wave* arrival, *PmP*, which can be used in conjunction with crustal velocity structure to estimate Moho depth. *Pn* phases travel below the Moho and, if their arrivals are clear, may be used to derive upper mantle *p-wave* velocities.

The spreading ridges are offset by a variety of discontinuities that are characterized by their length scale and geometry. First order discontinuities are the large transform faults separating the ends of two ridge segments by distances of tens to hundreds of kilometers (Macdonald et al, 1988). Another style of ridge segmentation is a non-transform offset (NTO), where two ridge segments are offset but are not separated by a transform fault with ridge-perpendicular motion. Instead the separation is

accommodated by bookshelf faulting, where the rocks between the ridge tips are rotated and sheared obliquely to spreading (Wetzel et al, 1993; Hey et al 2002). One form of non-transform offset is the overlapping spreading center (OSC). In this case the ends of two ridge segments are offset but they overlap for a distance, spreading along side one another. The ridge segments bounding an OSC tend to have a j-shaped geometry with the curve of each segment defining the overlapping region and, usually surrounding an overlap basin. These basins rotate as spreading continues on either side and they may also deform internally by faulting. The location of the OSC on the spreading axis changes through time, propagating in one direction along the ridge and moving relict ridge tips and overlap basins off axis often forming a V-shaped wake (Canales et al, 2003). A similar wake may be formed by the propagation of a NTO along a spreading axis, however the active ridge tips typically lack the j-shaped geometry.

### **Section 1.3 Regional history**

Iceland is part of the North Atlantic Igneous Province, which has been attributed to the Iceland hotspot. The Iceland plume is thought by some to have arrived at the lithosphere around 130 Ma although its track is not well defined prior to ~65 Ma (Forsyth et al, 1986; Kharin, 1991). Many workers identify the onset of volcanism even more recently at 62 – 61 Ma (e.g. Smallwood and White, 2002). Rifting began in the North Atlantic about 125 Ma and continued to propagate northward reaching the northeastern Atlantic basin by about 55 Ma (Smallwood and White, 2002). The Mid-Atlantic Ridge

intersected the plume about ~20 Ma (Trønnes, 2002; Mosar et al, 2002). The excess material supplied to the ridge by the plume has resulted in formation of the Iceland-Greenland and Iceland-Færoe Ridge, a region of thickened crust that extends perpendicular to the Mid-Atlantic Ridge from the eastern Greenland margin to northern Scotland. As the spreading center moved northwest away from the plume source, the rift zones on Iceland have jumped to the east to remain near the plume (Sæmundsson, 1974, 1978; Vink, 1984). The present day Reykjanes-Kolbeinsey plate boundary is 150-200 km west of the plume center (Trønnes, 2002). These episodes of rift relocation may also correspond to periods in which the supply of material from the Iceland plume was impeded or redirected (Abelson and Agnon, 2001).

Prior to 30 Ma. spreading north of the Reykjanes segment was accommodated on the Aegir Ridge (**Figure 1.1**). The rift axis then jumped to the eastern Greenland margin and a part of the margin was separated and moved east as spreading progressed, forming the present day Jan Mayen Ridge (Kodaira et al, 1997). The spreading axis jumped west again to the present day Kolbeinsey Ridge. The exact timing of the jump to the Kolbeinsey Ridge is debated but it is clear in the magnetic record that spreading was occurring on the Kolbeinsey by chron 6, ~19.6 Ma and may have begun as early as 26 Ma (Mosar et al, 2002; Talwani and Eldholm, 1977). Applegate (1997) presents a model for structural evolution of the Kolbeinsey Ridge, focusing on axial reorganization since 10 Ma. Based on the continuity of the magnetic lineations, Applegate proposes that the Kolbeinsey Ridge was an unsegmented spreading axis prior to chron 4, ~7.5 Ma. He

identifies three segments separated by two non-transform offsets on the present day Kolbeinsey Ridge, the Spar offset at  $69^{\circ}$  N and the  $68^{\circ}34'$ N offset, and notes that the magnetic lineations are offset and/or have attenuated amplitudes in a V-shaped pattern moving away from these offsets (**Figure 1.2**). He further notes that the margins of these discontinuities correspond with anomalously deep sea floor that marks the location of the discontinuity through time. He proposed that the  $68^{\circ}43'$ N offset between segments 1 and 2 has been propagating northward at a rate of 100 mm/yr due to gravitational spreading as a result of the positive relief of the southern Kolbeinsey Ridge, leaving a wake of disrupted magnetic fabric.

#### **Section 1.4 Plume-ridge interaction**

The interaction between mid-ocean ridges and mantle plumes is dependent on the proximity of the plume to the ridge and the spreading rate at the ridge. The lithosphere overlying the mantle plume is thermally weakened. If the plume intersects the oceanic lithosphere at too great a distance from the spreading axis, there will be no interaction between them, as in the case of Hawaii. However, there is both morphologic and geochemical evidence of plume interaction with ridges that are up to 500 km away (Ito and Lin, 1995). If the spreading center approaches the hotspot due to plate motion, the zone of weakened lithosphere may extend to the spreading center. At a slow spreading ridge, the same region of lithosphere has a longer residence time near the plume's higher

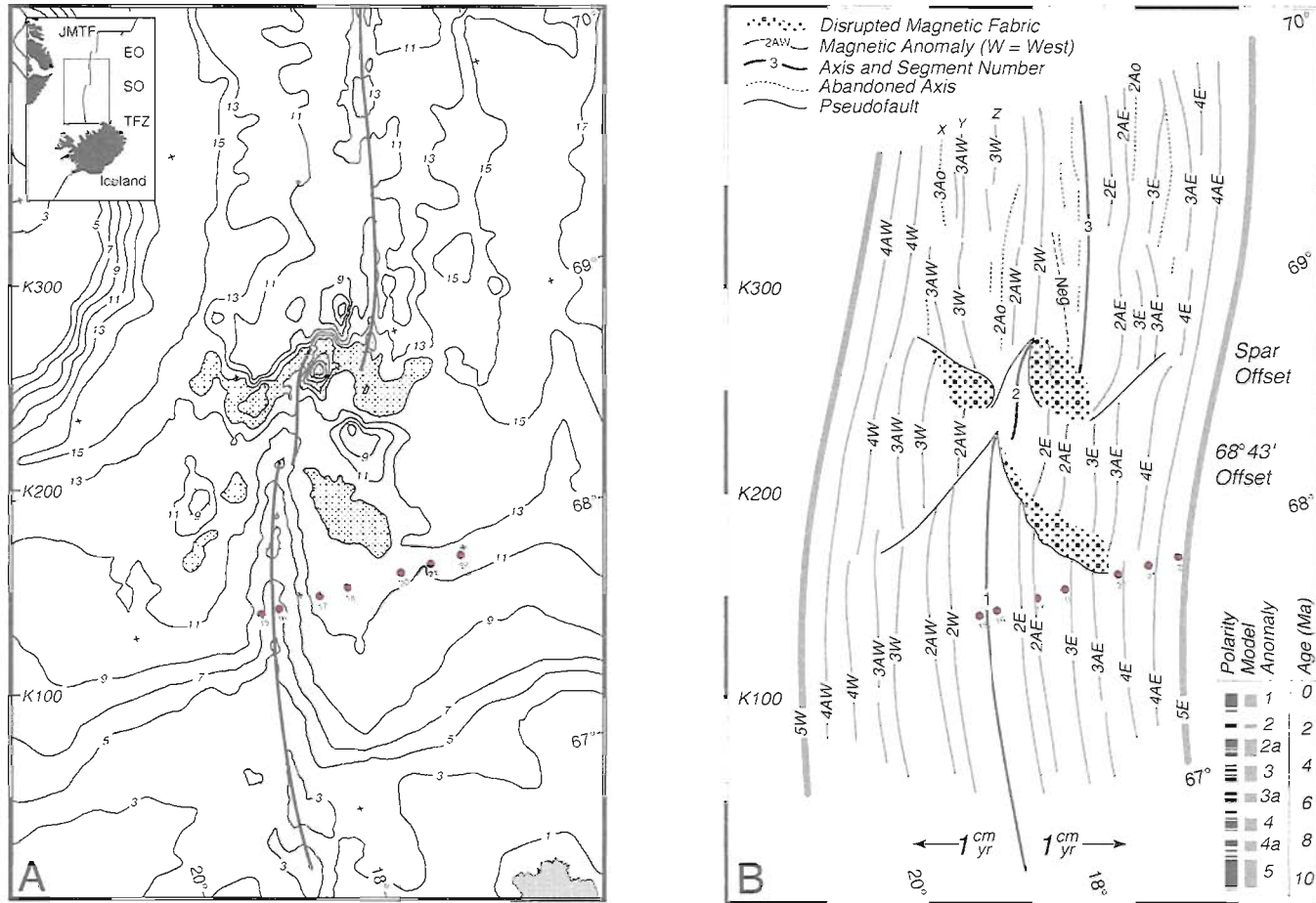


**Figure 1.2:** Bathymetry and magnetics of the Kolbeinsey Ridge. Spreading axis is interrupted at 68°34'N and 69°N (Spar Offset) by non-transform offsets. Approximate location of KRISE line 4 OBSs shown as red dots. **a)** Stippled areas show basins associated with off-axis traces of axial discontinuities. Isobaths are labeled in hundreds of meters and positive magnetic anomalies are shaded. **b)** Schematic representation of magnetic fabric for Kolbeinsey Ridge. Magnetic anomalies are labeled and disrupted magnetic fabric is stippled. The segments of the ridge are also labeled. Reproduced from Applegate (1997).

temperature and should experience a greater degree of weakening. This often results in a ridge “jump” where spreading begins to occur over the plume and ceases on that section of the ridge. As the plate margin continues to move in relation to the plume, subsequent ridge jumps occur to maintain spreading over the plume. These sections of the spreading center are typically separated from the rest of the ridge by transform faults.

### **Section 1.5 V-shaped ridges**

The influx of material from the Iceland plume has resulted in a 19-40 km thick crust beneath Iceland and in the generation of thicker crust along the spreading centers to the north and south (Kodaira et al, 1998; Smallwood and White, 1998; Weir et al, 2001). Material from the plume is believed to migrate along the ridge axis for a great distance, particularly to the south along the Reykjanes Ridge, resulting in a gradually diminishing geochemical signature along with progressively thinner crust (Hooft et al, 2006). Vogt (1971) first recognized a series of V-shaped ridges formed by bathymetric undulations sub-parallel to the Reykjanes Ridge. V-shaped features are also prominent in the free-air gravity on the Reykjanes but they are not present in magnetic field measurements (**Figure 1.3, 1.4**). These features are thought to record the migration of a pulse of excess plume material along the spreading axis away from the source. It has also been suggested that the ridges reflect an interruption of plume material delivered to the crust due to a lithospheric reorganization, perhaps the onset of a ridge jump (Georgen and Lin, 2003; Johnson, 1972). There is also some evidence of these V-shaped features along the

Kolbeinsey Ridge to the north but it is much more subtle and it is believed that a majority of plume material is preferentially diverted to the south (Hooft et al, 2006; Sandwell and Smith, 1997). The eastern side of the northern Kolbeinsey Ridge has four prominent free-air gravity anomalies similar to those on the Reykjanes, but the southern segment has only one such feature. The V-shaped features are most easily discerned in the free-air gravity and workers infer that these are the result of bathymetric highs that are isostatically supported by thicker crust (Jones et al, 2002). One study (Smallwood and White, 1998) presents seismic evidence that these undulations in gravity are the result of variations in crustal thickness on the Reykjanes Ridge.

Jones et al (2002) present the results of an analysis of the V-shaped free-air gravity anomalies on the Reykjanes and Kolbeinsey Ridges. The authors plot the short wavelength component of gravity in terms of age versus distance from the Iceland mantle plume. South of Iceland, they are able to identify seven gravity highs in the Irminger Basin west of the Reykjanes and four highs in the Iceland basin to the east (**Figure 1.5**). They also identify four high gravity anomalies on the eastern side of the northern Kolbeinsey Ridge (**Figure 1.3, 1.5**). Unlike the gravity ridges on the Reykjanes, the ridges on the Kolbeinsey do not appear to originate at the transfer zone marking the transition from the Iceland region to oceanic spreading ridge; rather, they appear to begin at the transition from the southern to northern Kolbeinsey Ridge segments. On the southern Kolbeinsey Ridge there is only one clear free air high gravity anomaly and it terminates at the Spar offset rather than continuing to the northern Kolbeinsey segment.



The plot of short wavelength gravity reveals additional gravity anomalies east of the spreading axis. These do not have the linear appearance of the other features and are not continuous from the southern to northern ridge segments. Jones et al do not discuss these features on the southern Kolbeinsey Ridge.

On the Reykjanes Ridge, Jones et al identify a primary periodicity of 5-6 Ma for the gravity ridges. They suggest a secondary periodicity of 2-3 Ma due to bifurcations in some of the gravity ridges. They use the gravity anomalies to evaluate the nature of plume material flow in the mantle. They attribute the formation of these V-shaped features to increased melt production at the ridge due to pulses in temperature in the Iceland mantle plume head. In this case, the term plume head is being used to describe the broad region of plume material ponding radially beneath the lithosphere, rather than the initial phase of plume intersection with the crust. These variations in the plume head may be the result of temperature variations within the plume stem or the interaction between the plume stem and head may be interrupted by lithospheric reorganization such as a jump in the spreading axis (Jones et al, 2002; Geoggin and Lin, 2003). The distribution of lava flows in the region may also be explained by a model that requires two hot sheets of asthenospheric mantle that intersect at the plume conduit (Smallwood and White, 2002).

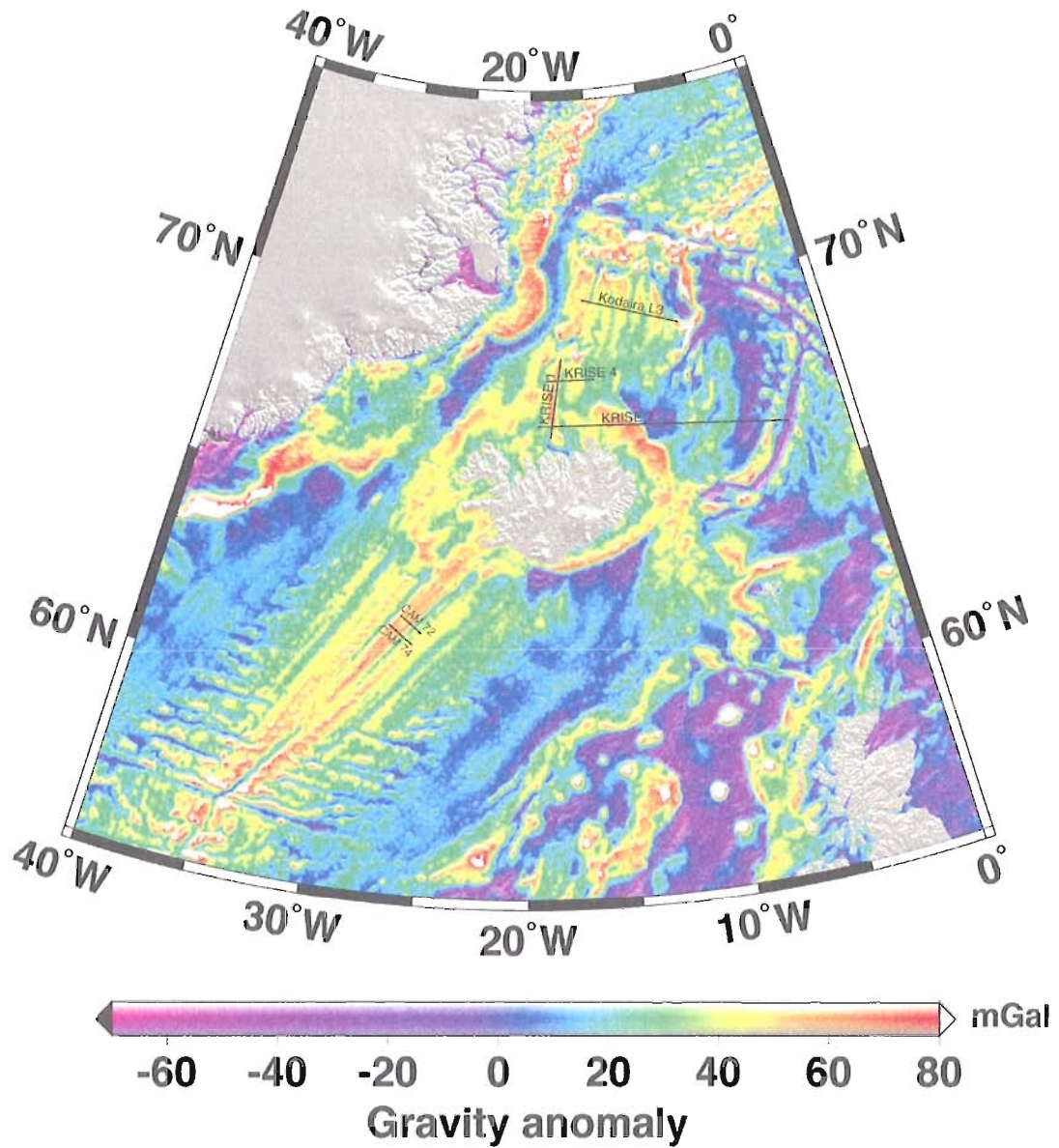


**Figure 1.3:** Gravity anomalies north and south of Iceland. The locations of the three KRISE seismic profiles are labeled. Also included are the locations of two previous seismic experiments discussed in the text: CAM 72 and CAM 74 (Smallwood and White, 1998) and Kodaira L3 (Kodaira et al, 1998).

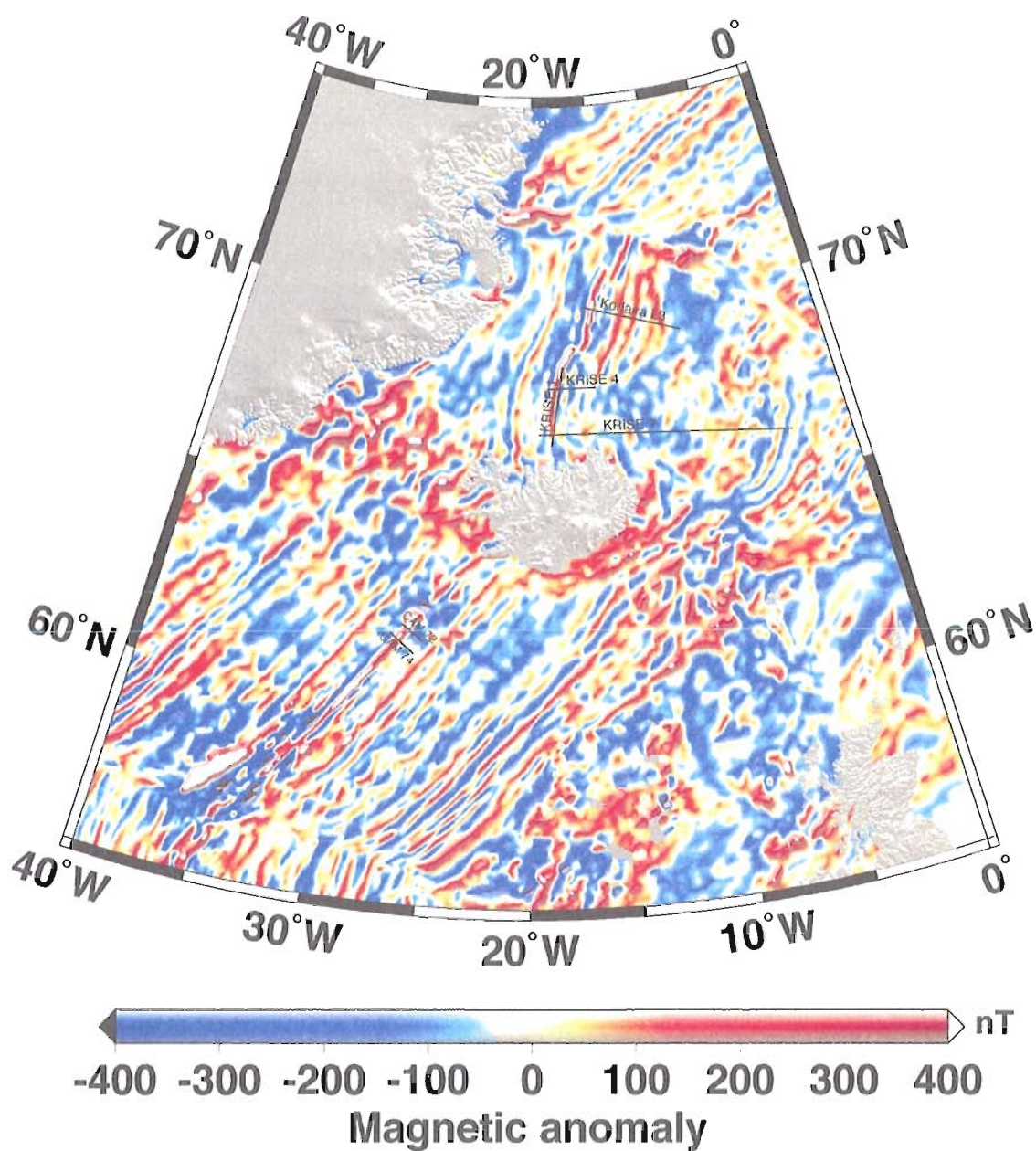


**Figure 1.4:** Magnetic anomalies north and south of Iceland. The locations of the three KRISE seismic profiles are labeled. Also included are the locations of two previous seismic experiments discussed in the text: CAM 72 and CAM 74 (Smallwood and White, 1998) and Kodaira's L3 (Kodaira et al, 1998). Magnetic data from Maus et al, (2009).

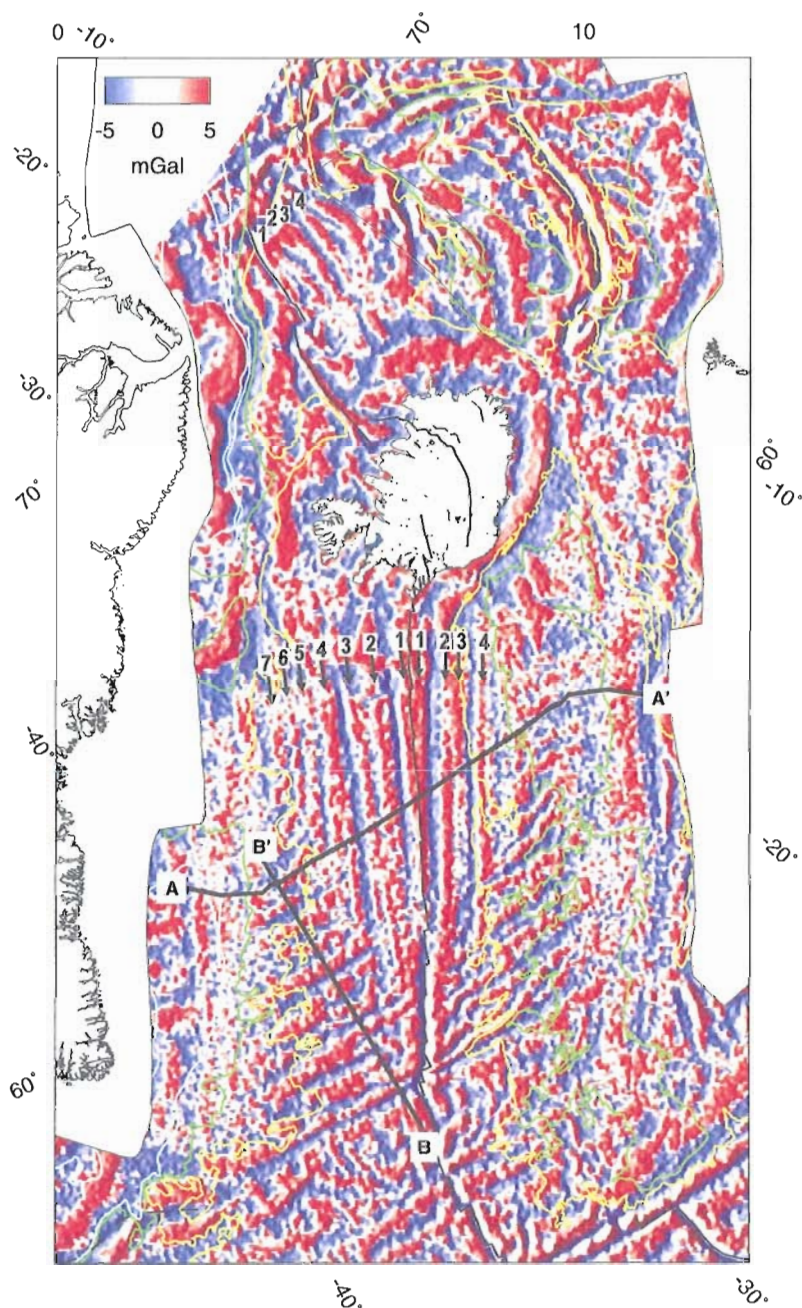


**Figure 1.5:** Short-wavelength component of satellite gravity field. The long wavelength field was calculated using a Gaussian filter of radius 100 km and subtracted from the original field to give the short-wavelength field. Numbered arrows refer to V-shaped ridges identified by Jones et al. Colored lines indicate sediment thickness: yellow = 500 m; green = 1 km; blue = 1.5 km, 2 km, and 2.5 km. Lines A-A' and B-B' mark locations of profiles discussed by Jones et al. Reproduced from Jones et al (2002). I have moved the labels on the Kolbeinsey Ridge from the authors' original placement.

## CHAPTER II

### PREVIOUS STUDIES OF TEMPORAL CHANGES IN PLUME INFLUENCED RIDGE NORTH AND SOUTH OF ICELAND

#### Section 2.1 Smallwood and White (1998)

Smallwood and White (1998) is the primary study that provides evidence for thicker crust associated with gravity and bathymetric highs on the eastern flank of the Reykjanes Ridge. They present the results of a seismic, gravity, and magnetic survey of the Reykjanes Ridge between  $61^{\circ}$  -  $62^{\circ}$  N. This study features five intersecting seismic lines. CAM 71 and CAM 73 are parallel to the ridge with CAM 71 positioned along the ridge axis and CAM 73 positioned in the trough between two bathymetry and gravity highs. CAM 72, CAM 74, and CAM 75 are orthogonal to the ridge, beginning on the west side and crossing the ridge to the east to 7 Ma crust (CAM 72 and CAM 74 only). **(Figure 2.1, 2.2)** These are each defined by two ocean-bottom seismometers (OBS) with ~50 km spacing. They interpret these results as a change in crustal thickness from 10 km at the ridge to 7.8 km thick in 5 Ma crust in the gravity trough. It should be noted that

crustal thickness is only well constrained in the central portions of CAM 71 and CAM 74 because the reflected arrivals on CAM 72 and CAM 73 do not appear to have been used in the ray tracing. If a fairly planar geometry is assumed for the Moho at this scale, then it is reasonable to suggest that the thinner crust coincides with the location of the bathymetric troughs. The authors are able to successfully model the magnetization along CAM 71 by treating layer 2A as a variable thickness magnetic layer with a constant magnetization of 25 A/m. Gravity modeling for CAM 72 and CAM 74 shows that this seismic structure is consistent with the observed free air anomalies, both with and without mantle thermal contribution.

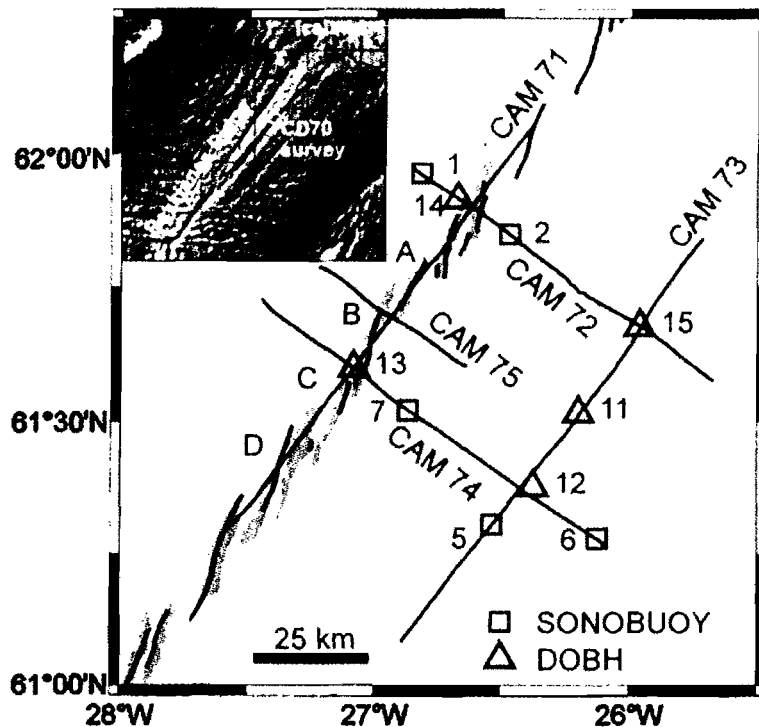


**Figure 2.1:** Smallwood and White (1998) experiment geometry. Lines CAM 72 and CAM 74 cross the ridge and extend southeast to 7 Ma age crust. CAM 73 is located in a trough between two bathymetric highs. Reproduced from Smallwood and White (1998).

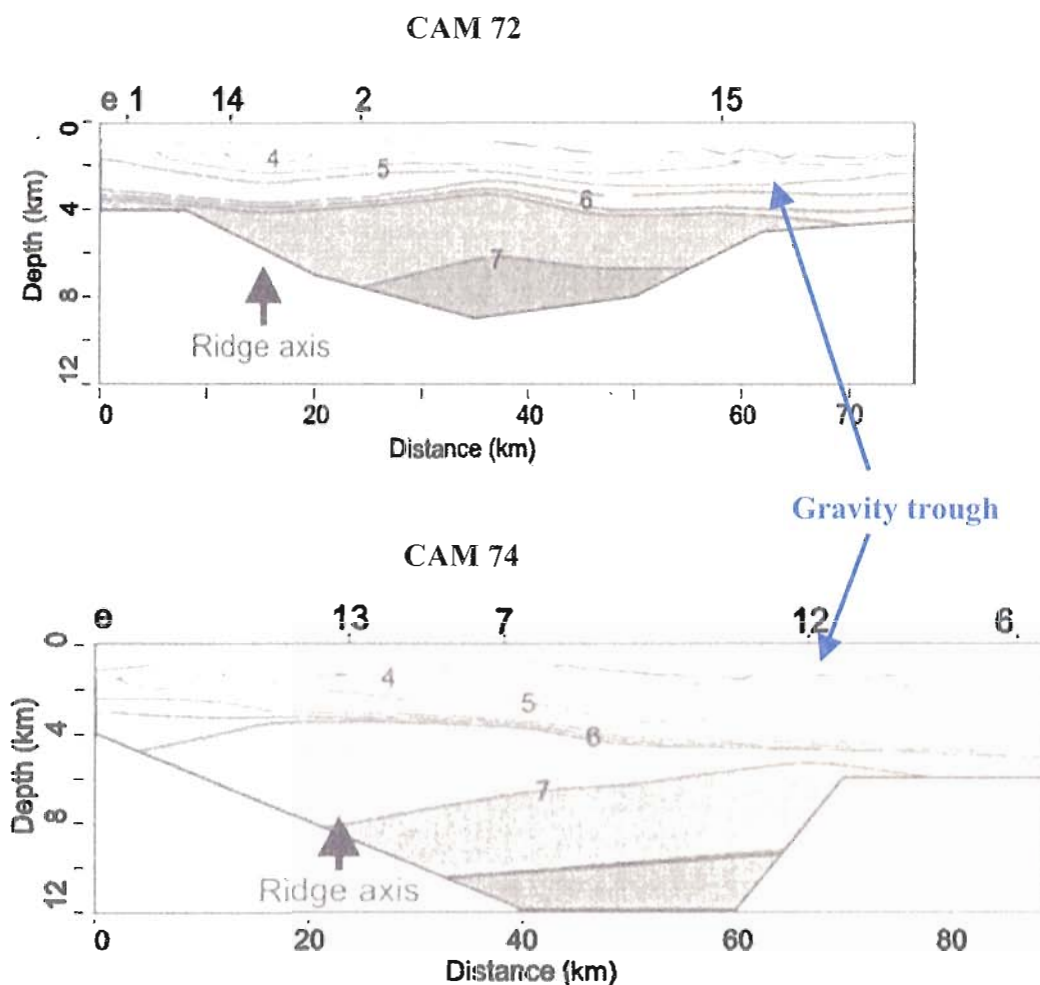


**Figure 2.2:** Final velocity models for Smallwood and White's CAM 72 and CAM 74. Selected velocities are labeled, in km/s. Numbers 12 – 15 represent the locations of OBSs. The other numbers show the locations of sonobuoys. In CAM 74, the darker line indicates the modeled location of the Moho. The Moho is not reached in CAM 72. OBSs 12 and 15 are placed in the gravity trough. I have scaled the images so that the distance is approximately the same in both images. Reproduced from Smallwood and White (1998).

## Section 2.2 Kodaira et al (1997)

Kodaira et al (1997) detail the crustal structure of the eastern side of the northern Kolbeinsey Ridge at 70°N. This study featured three transects: L1 - along the ridge, L2 - parallel to the ridge 12 km east of the spreading axis, and L3 - perpendicular to the ridge, beginning west of the spreading center and continuing ESE to 7 Ma age crust. Kodaira et al (1998) extends L3 using previously published seismic data (Kodaira et al, 1998). This profile begins west of the spreading center and continues east to the Jan Mayen basin for a total length of ~275 km. This extended profile was created using refracted and reflected arrivals from a total of 12 OBSs, 6 of which were used in the study reported in the 1997 publication. This data set has good ray coverage and Moho depth is well constrained along 200 km of the profile.

This profile crosses four of the high gravity ridges identified by Jones et al (2002). The authors see thicker than usual crust generated at the spreading center and attribute this to the influence of the Iceland plume (**Figure 2.3**). The crustal thickness varies <1.5 km along the entire length of the profile out to the Jan Mayen basin, where there is rapid thinning and a change in *p-wave* velocity at the transition from oceanic to extended continental crust. Unlike Smallwood and White (1998), they do not see the dramatic change in crustal thickness in the region of these high gravity ridges. Kodaira et al (1998) also displays the magnetic anomaly along this profile, with higher amplitudes out to chron 5 followed by a rapid decay in signal strength.



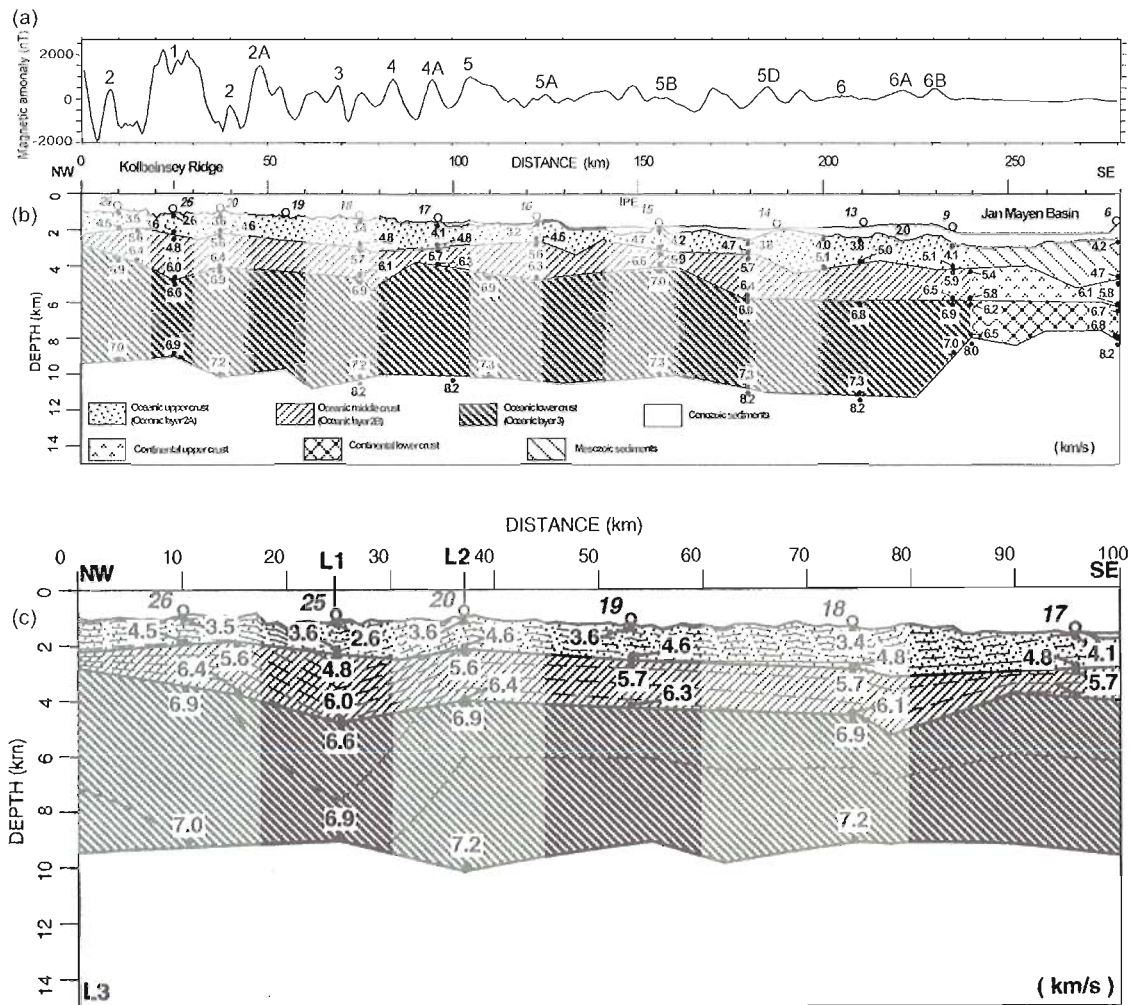


**Figure 2.3:** Magnetic anomalies and crustal velocities along Kodaira et al's L3 transect. **a)** Magnetic anomalies; major identifying magnetic chrons are labeled. **b)** Velocity model for entire profile from the Kolbeinsey Ridge to the Jan Mayen Basin. Layers are shaded according to oceanic crustal layers associated with observed *p-wave* velocities. Numbers in white boxes indicate velocities on either side of the interface between crustal layers. Distance along profile in km is indicated at the top of the figure. **c)** Final velocity model of western 100 km of L3. Features are indicated in the same manner as **b**, with the addition of the locations of profiles L1 and L2 added. Colored bands indicate the approximate locations of high free air gravity anomalies. Reproduced from Kodaira et al (1997, 1998).

## CHAPTER III

### METHODS

#### Section 3.1 Experiment details - instrumentation

KRISE Line 4 consisted of a combination of 8 digital and analog ocean bottom seismometers (OBSs) numbered west to east, OBS 15 through OBS 22, with 9-23 km spacing, beginning just west of the ridge and continuing east to ~12 Ma old crust (**Figure 3.1**). Due to an instrument failure, the data collected on OBS 19 was unusable. The sources were 691 shots from a 4800 in<sup>3</sup> airgun array shot from east to west with 180 m spacing. Even shot spacing was facilitated by shipboard GPS. Both the deployment of the instruments and the source shots were from the University of Bergen's *Håkon Mosby* research vessel. In addition to the shot instants and locations, gravity, magnetometer, and ministreamer reflection data was collected by the *Håkon Mosby*. The instruments were recovered by the *Ægir*, an Icelandic Coast Guard vessel.

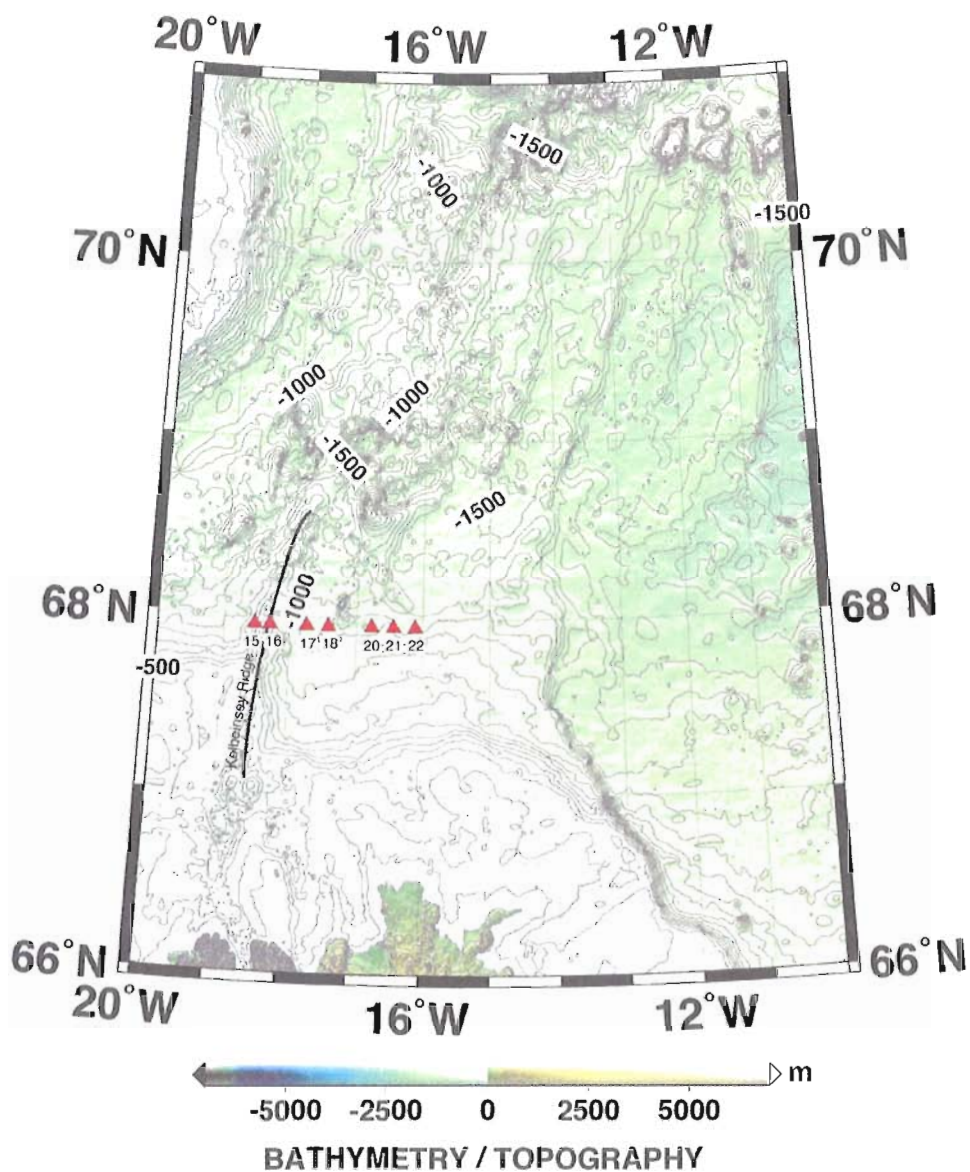


**Figure 3.1:** Bathymetric and topographic map of the Kolbeinsey Ridge. Contour interval is 100 m; select contours are labeled. Line 4 OBS locations are shown as red triangles. The ridge axis of the southern segment of the Kolbeinsey Ridge is shown as a black line.

Wide angle arrivals were recorded on OBSs. The waveforms were Butterworth bandpass filtered from 5-17 Hz and 3-12 Hz, for  $Pg$  and  $PmP$ , respectively. We see  $Pg$  and  $PmP$  arrivals with good signal to noise ratios out to distances of 35-50 km and 50-60 km, respectively (**Figures 3.2 – 3.5**). There are clear  $Pn$  arrivals on OBSs 15, 17, 20, and 21 at distances that vary from 40 to 65 km from the station (**Figures 3.6, 3.7**). Single channel reflection data was also collected.

I picked a total of 2161  $Pg$  and 1422  $PmP$  arrivals on seven OBS record sections. I have an unusually large number of  $PmP$  arrivals largely due to the central location of OBS 18; there are clear arrivals out to both ends of the profile. I also picked 102  $Pn$  arrivals on four of the stations. Picks were made manually using the Upicker MATLAB scripts written by William Wilcock at University of Washington. Errors were manually assigned based on the clarity of the arrivals; the average errors assigned were 0.017, 0.020, and 0.022 ms for  $Pg$ ,  $PmP$ , and  $Pn$ , respectively.

## **Section 3.2 Data analysis**

### **Seismic**

The travel times of the picked arrivals were used to perform a 2-D tomographic inversion for crustal velocity and Moho depth using the methods described in Korenaga et al (2002). The tomographic inversion solves for the  $p$ -wave velocity structure and Moho depth that best fit the travel times for all shot and receiver geometries. The  $Pg$

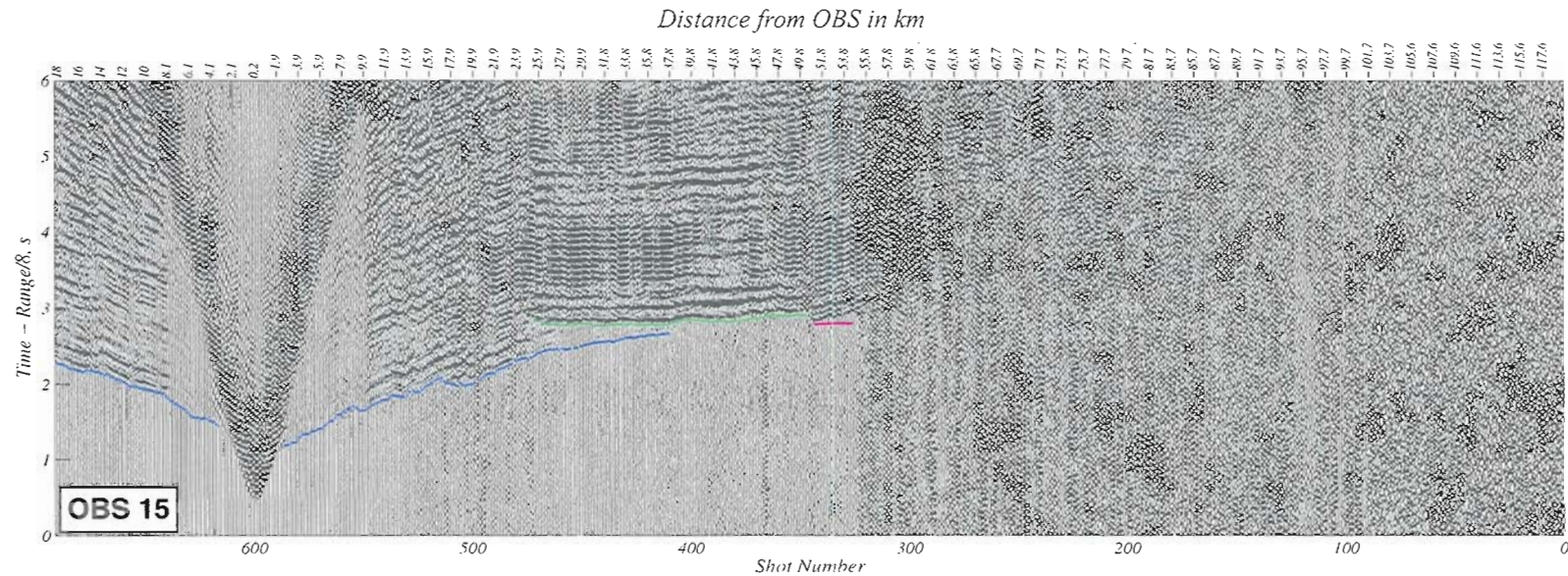


**Figure 3.2:** Record section from OBS 15. This shows the first six seconds of data recorded for each of the 691 shots. The traces are sorted by shot number from west to east. Shot number is on the lower horizontal axis, distance from the station in kilometers is on the upper horizontal axis. Time is on the vertical axis and has been corrected for a moveout of 8 km/s. This serves to reduce the height of the traces and causes arrivals with an apparent velocity near 8 km/s to appear horizontal on the section. Traces have been bandpass filtered with lower and upper bounds of 3 Hz and 17 Hz, respectively. The amplitudes have been scaled in order to show earlier and later arrivals similarly. Picked arrivals are shown, without the assigned errors:  $P_g$  in blue,  $P_{mP}$  in green, and  $P_n$  in magenta. The same scheme applies to the record sections on the following pages. The prominent V-shaped series of arrivals beginning above shot 600 represent the arrival of the direct wave through the water column.

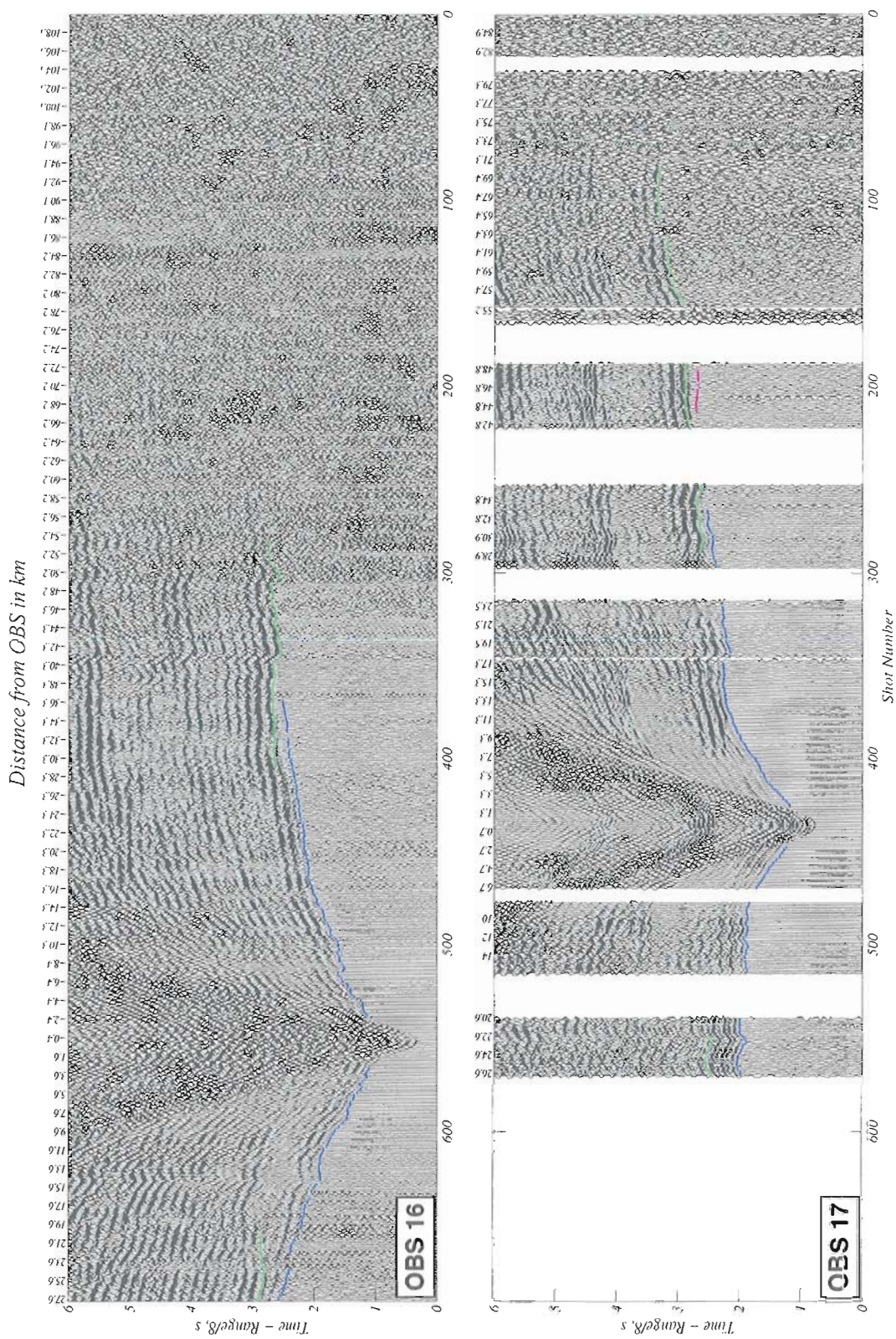
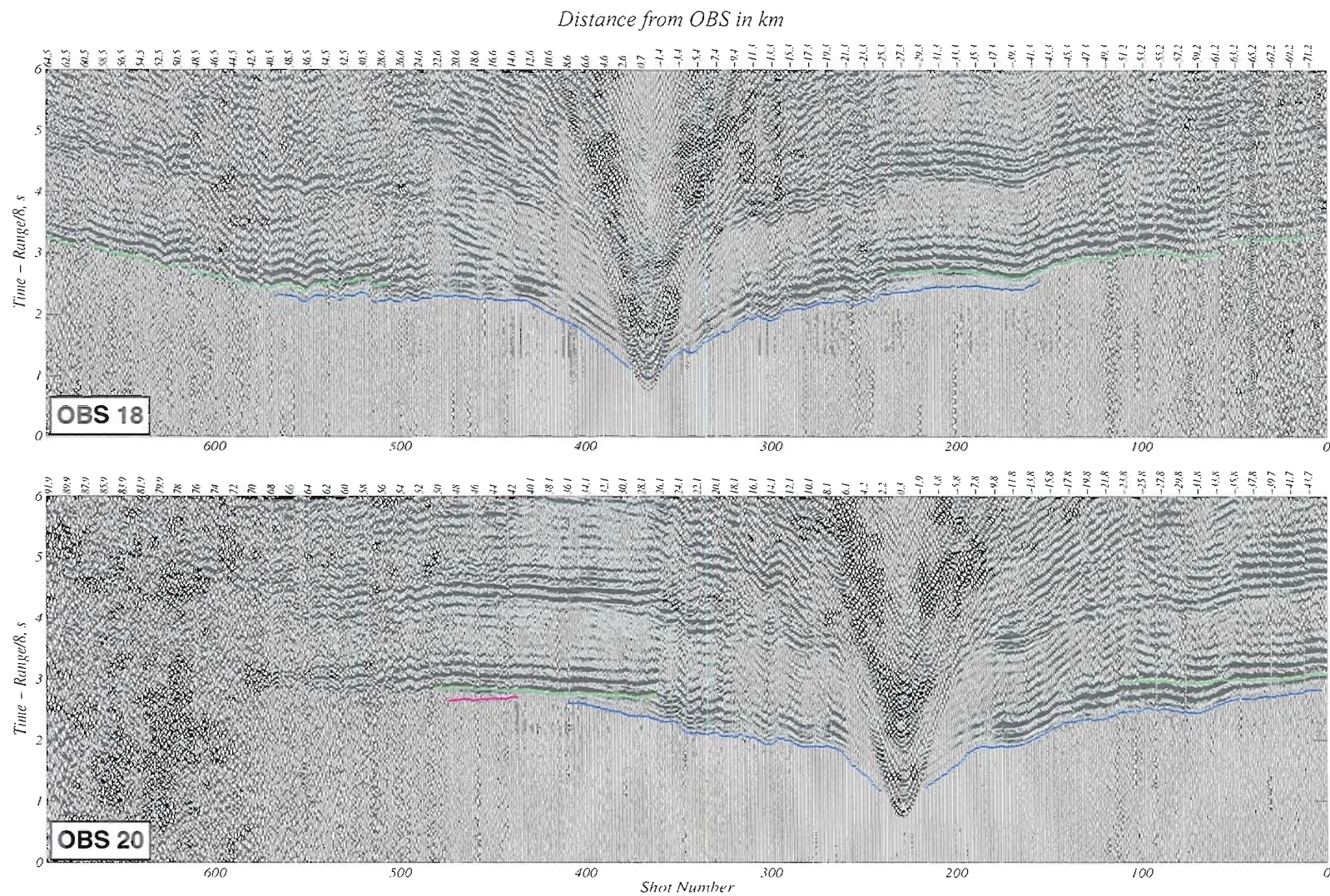


Figure 3.3: Record sections from OBS 16 and OBS 17. See Figure 3.2 for description.



**Figure 3.4:** Record sections from OBS 18 and OBS 20. See Figure 3.2 for description.

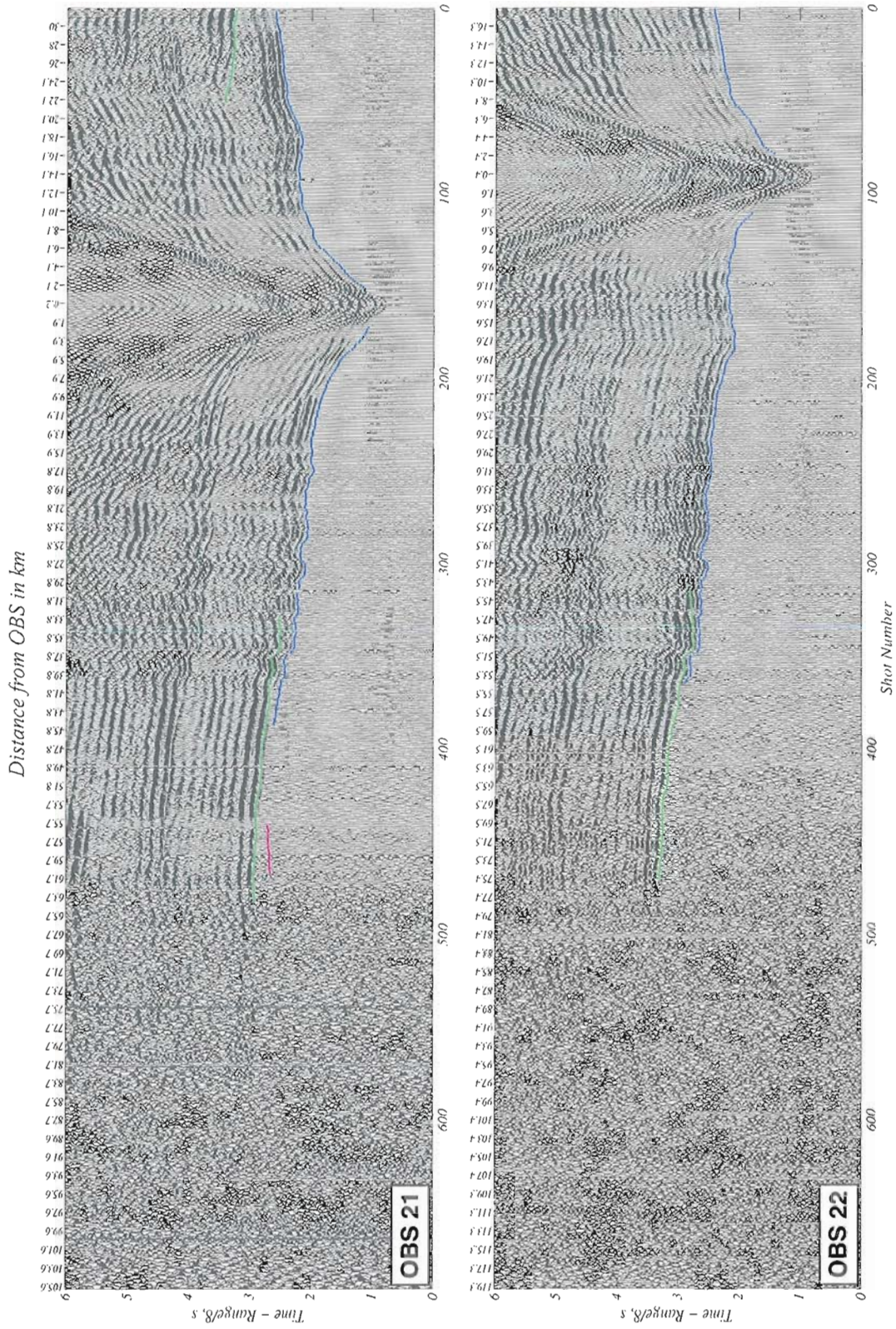
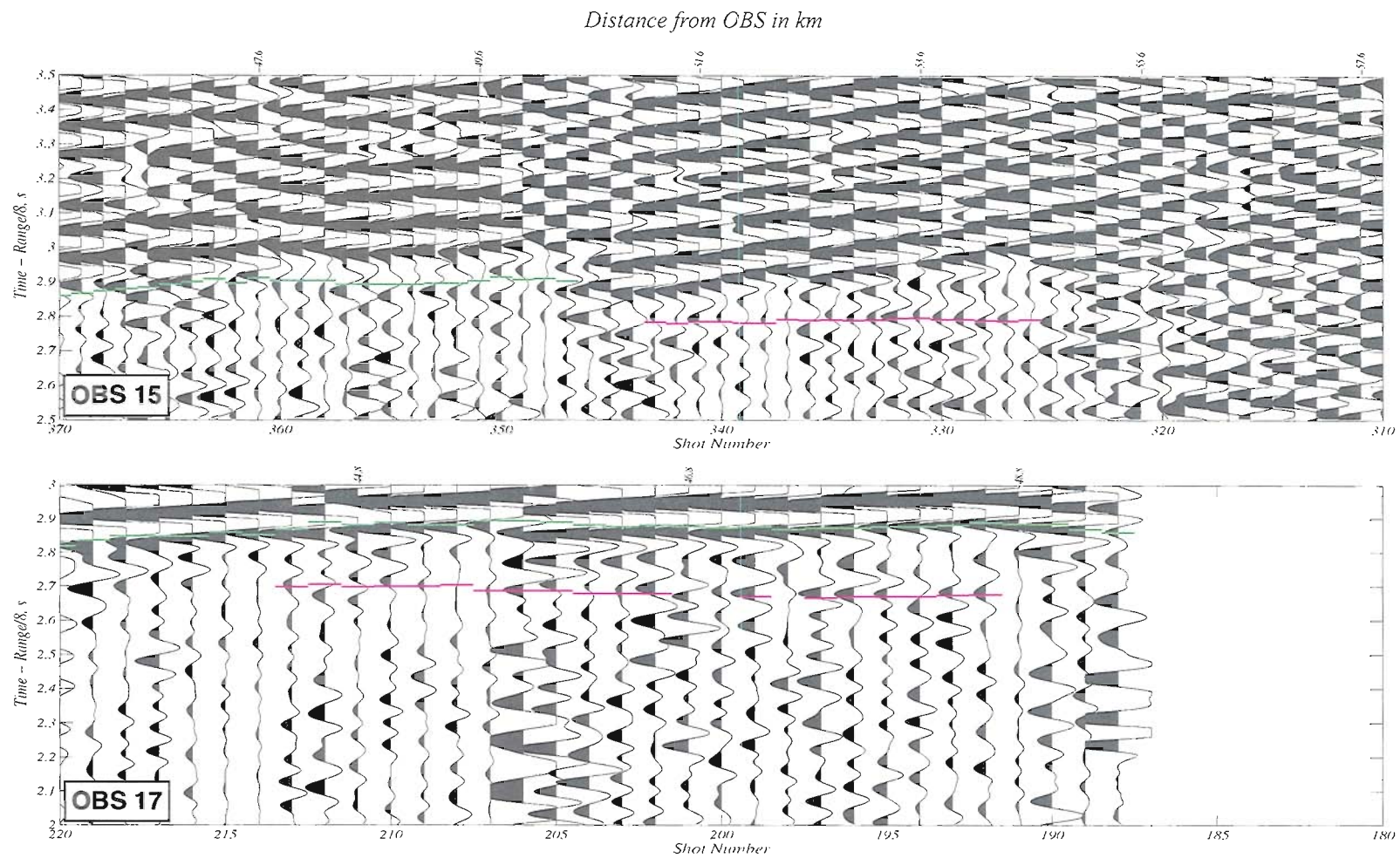
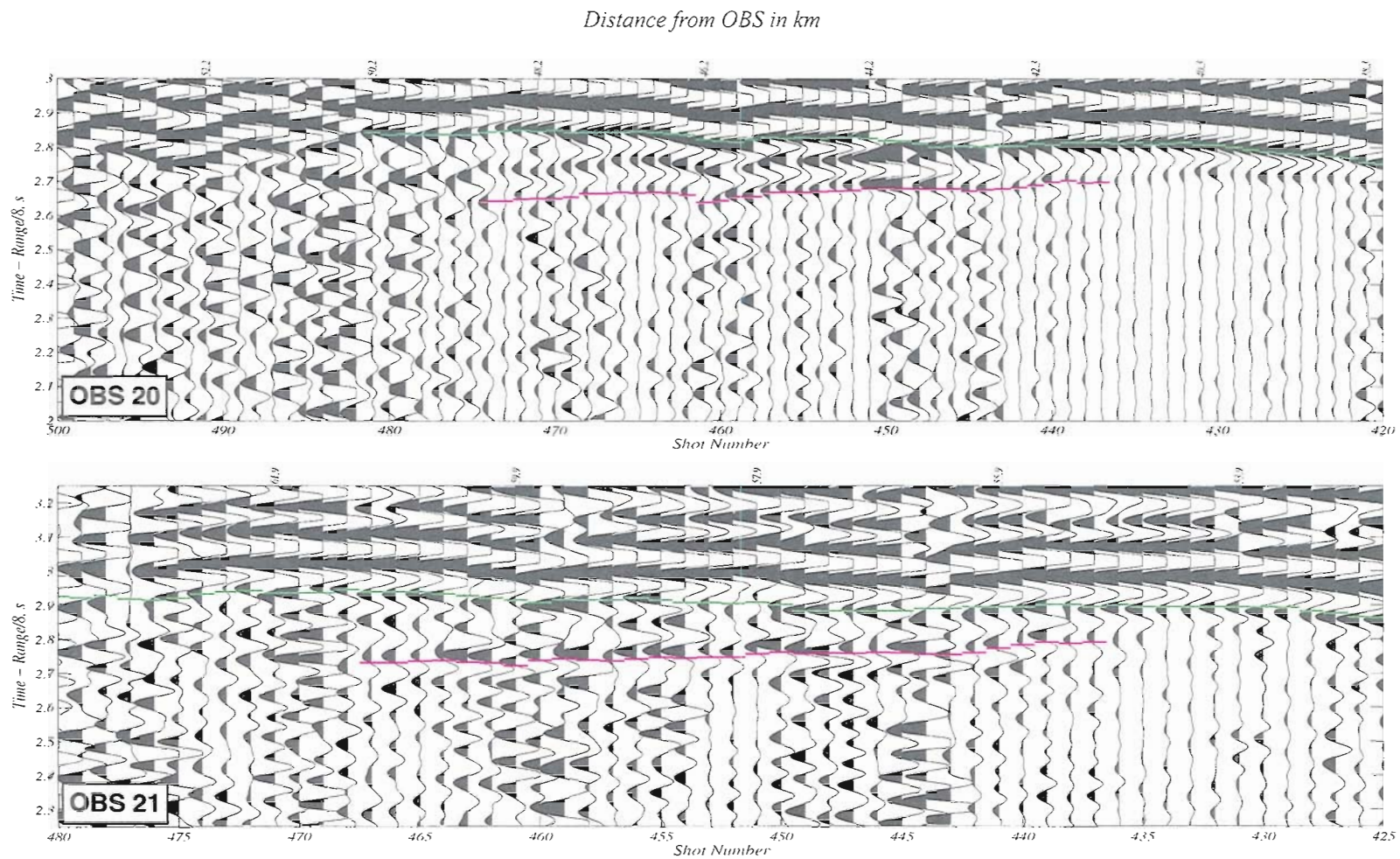


Figure 3.5: Record sections from OBS 21 and OBS 22. See Figure 3.2 for description.





**Figure 3.6:** A portion of the record sections for OBS 15 and OBS 17.  $PmP$  and  $Pn$  arrivals are shown in green and magenta, respectively.



**Figure 3.7:** A portion of the record sections for OBS 20 and OBS 21.  $PmP$  and  $Pn$  arrivals are shown in green and magenta, respectively.

arrivals were utilized to resolve velocity structure in the upper 5 km of crust. The *PmP* arrivals were used in conjunction with the well-resolved upper crustal velocities to determine the velocity structure of the lower crust and the depth of the Moho. *Pn* arrivals, where present, were used to estimate upper mantle *p-wave* velocities. The *Pn* arrivals were traced through the final velocity model generated using *Pg* and *PmP* arrivals. In order to ensure that all modeled *Pn* rays turned below the Moho, a constant velocity of 8 km/s was initially used for every node with a depth greater than the final predicted Moho.

Shot and station locations were converted from latitude-longitude to a Cartesian coordinate system with 0 at the west end of the profile. Shot 691 and OBS 15 were the source and station furthest west. Initial station locations are known only by the location at which they are dropped from the ship. Station locations were corrected using the predicted travel times for the direct wave traveling through the water column (Hooft et al, 2006). I used a constant velocity of 1.45 km/s for seawater. The arrival of the direct wave was picked on each station out to a distance of 10 km on each side. On the station nearest to the spreading axis, OBS 16, the water wave arrival was picked out to a distance of 20 km due to high levels of noise on the closest arrivals. All stations were relocated laterally along the profile (**Table 3.1**). A timing correction was also applied to each station; this will also accommodate any off-profile shift in station location.

| Station ID | Drop Latitude | Drop Longitude | Drop Depth (m) | Relocated Latitude | Relocated Longitude | Relocated Depth (m) | Distance (km) | Location diff (km) | Time shift (s) |
|------------|---------------|----------------|----------------|--------------------|---------------------|---------------------|---------------|--------------------|----------------|
| 15         | 67.9517       | -18.5353       | 659            | 67.9517            | -18.5359            | 664                 | 18.139        | -0.026             | 0.033          |
| 16         | 67.9517       | -18.3072       | 537            | 67.9517            | -18.3051            | 510                 | 27.775        | 0.089              | -0.033         |
| 17         | 67.9517       | -17.7525       | 1138           | 67.9517            | -17.7525            | 1138                | 50.839        | 0.001              | -0.007         |
| 18         | 67.9517       | -17.4242       | 1146           | 67.9517            | -17.4243            | 1146                | 64.538        | -0.003             | -0.011         |
| 20         | 67.9517       | -16.7673       | 1108           | 67.9517            | -16.7676            | 1108                | 91.947        | -0.013             | -0.006         |
| 21         | 67.9518       | -16.4392       | 1150           | 67.9518            | -16.4395            | 1150                | 105.643       | -0.012             | -0.005         |
| 22         | 67.9518       | -16.1108       | 1208           | 67.9518            | -16.1118            | 1209                | 119.321       | -0.041             | -0.008         |

**Table 3.1:** OBS locations showing original (drop) and adjusted location. Distance is from west end of profile.

### Inversion details

I began with a one-dimensional model of velocity as a function of depth. There were 50 vertical nodes ranging from 0 – 16.3 km depth, with closer spacing at shallower depths and velocities ranging from 2.13 km/s at the seafloor to 7.37 km/s at 16.3 km depth. The starting model has a steep velocity gradient in the upper kilometer consistent with oceanic layer 2A. The velocities increased rapidly to 6.5 km/s within the first 3.5 km, increased linearly to 7.3 km/s by 10 km depth, and only increased slightly within the final 6 km (**Figure 3.8**).

This 1-D profile was converted into a laterally homogeneous 2-D velocity mesh with nodes in the horizontal direction every 200 meters. The zero point of the velocity grid is chosen to coincide with the western most bathymetric measurement. The horizontal locations are extended west to -5 km and east to 140 km to accommodate all shot locations, resulting in 726 horizontal nodes. An additional node is added at the horizontal location of each of the seven stations along the profile resulting in a 733 horizontal x 50 vertical node velocity grid. This velocity mesh is then sheared to “hang”

from the seafloor so that the starting velocity is the same everywhere at equal depth.

**(Figure 3.9)** In addition to the velocity mesh, I supplied a starting Moho depth at horizontal nodes with one kilometer spacing.

I performed the inversion for velocity using the 2-D tomography code of Korenaga et al (2002). This method uses a combination of the ray-bending method and the graph method, which is also known as the shortest path method (Moser, 1991). Korenaga's method first runs a forward model by calculating travel time and ray paths through the initial velocity model for each source-receiver pair. It then subtracts the calculated travel times from the observed travel times given in the input file to create an array of travel time residuals. The method then runs an inverse model, which determines adjustments to velocities at each node to minimize the difference between the observed and predicted travel time. This process is repeated for a user-defined number of iterations in order to minimize the misfit between observed and predicted travel times. Because there is not data for a large number of the nodes, the inversion uses a correlation length in both horizontal and vertical directions that smoothes the velocity perturbations over adjacent nodes and a weighting is applied to these correlation lengths (Korenaga et al, 2002). These correlation lengths are much shorter in the shallow crust, due to the denser ray coverage, and lengthen with depth.

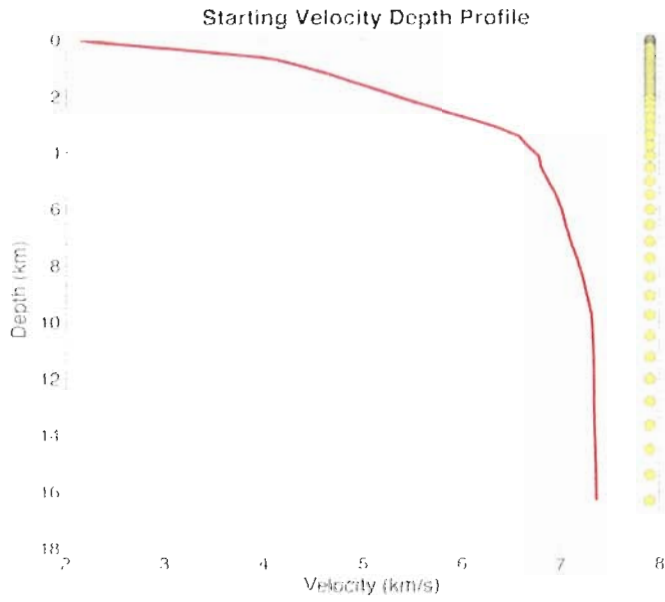


**Figure 3.8:** Starting velocity-depth profile. Depth node spacing is represented by yellow circles.

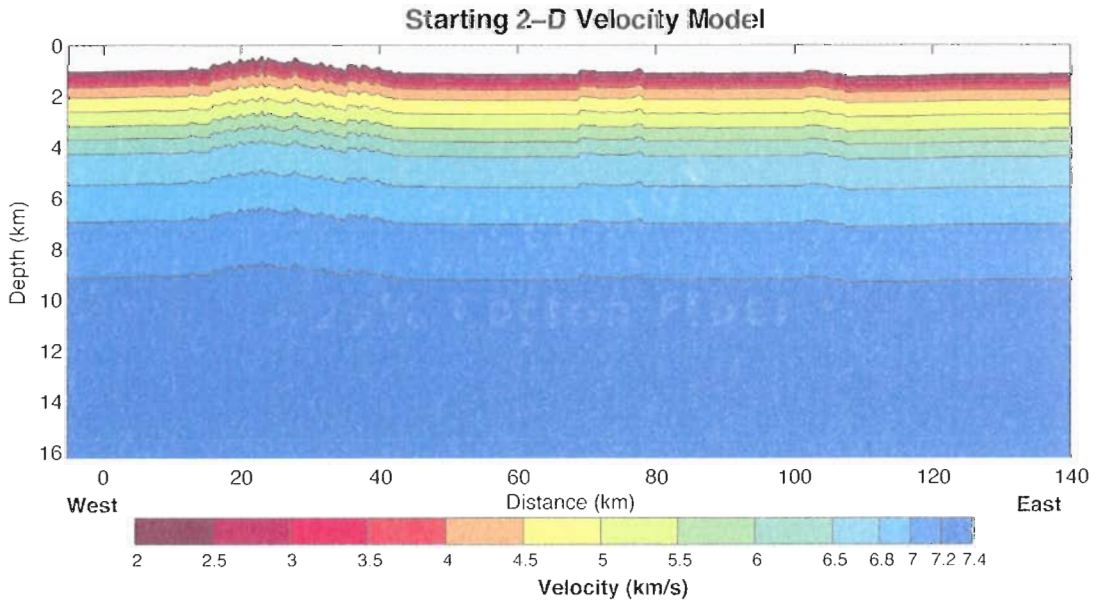


**Figure 3.9:** Starting 2-D velocity model, sheared according to bathymetry.

The Moho is represented by a floating reflector. The inversion also solves for perturbations in Moho depth that minimize the misfit to the travel times of the *PmP* phase. The reflected arrivals can be given a greater weight than the *Pg* arrivals in the inversion. The Korenaga code builds a velocity profile including the water column, making it necessary that the Moho depth be from the sea surface rather than the seafloor. A correlation length and weight are also applied to the depth perturbations.

### **Gravity data**

Gravity measurements were recorded along the profile at 165 m increments for a total of 819 data points. The predicted gravity fields due to bathymetry and crustal thickness, given by my final model of Moho depth, were estimated using a Parker 2-D approximation (Parker, 1973). This method requires that the gravity field be calculated over an area so my profile is repeated for 300 km to the north and south and padded by 100 km to the east and west. I used typical values for density of 1000, 2300, 2900, and 3300 kg/m<sup>3</sup> for the seawater, upper crust, lower crust, and mantle, respectively. This resulted in a simple model of the crust that does not account for lateral variations in crustal density (**Figure 3.10**). I also created a laterally varying crustal model to make a more detailed gravity prediction using a method developed by Korenaga et al (2002). This method used my final 2-D velocity model to select *p-wave* velocity contours at 4.0 and 6.5 km/s to represent the boundaries between upper, middle, and lower crust. These velocities were converted to density using the relationships for upper crust and lower crust described by Carlson and Raskin (1984) and Carlson and Herrick (1990),

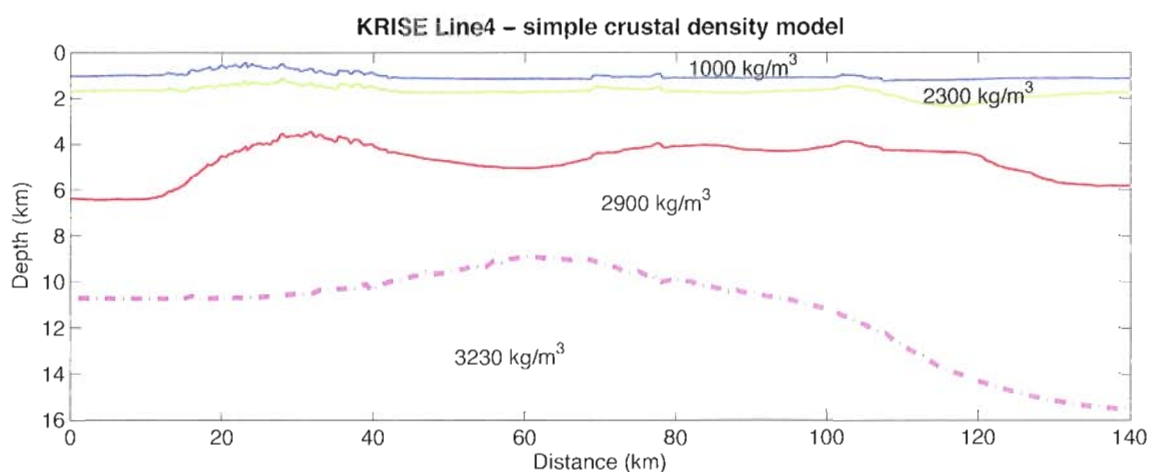


**Figure 3.10:** Simple crustal density model used for gravity prediction. Contours represent boundaries between water and seafloor (blue), upper and mid-crust (green), mid and lower crust (red), and crust and mantle (magenta dashes). Densities are given for each layer: sea water, upper crust, lower crust, and mantle.

respectively, and were used in conjunction with bathymetry and Moho depth to predict the gravity signal due to the crust. Two different predictions were created, one using only upper crustal density values for the entire thickness of crust and one that uses both upper and lower crustal density values. Measured free-air gravity was corrected for bathymetry to give Bouguer gravity anomaly. Mantle Bouguer gravity anomaly was calculated by removing the gravity signal predicted by a mantle with topography determined by the modeled Moho depth (this differs from the conventional use of the term mantle Bouguer anomaly). A lithospheric cooling model was applied to predict the effects of thermal contraction as the material moves away from the ridge (Turcotte and Schubert, p 175).



## Magnetic data

Magnetic measurements were collected at 5 – 6 second intervals for a total of 10,044 data points. The orientation and strength of the magnetic field during data collection was calculated using the online calculator provided by NOAA (<http://www.ngdc.noaa.gov/geomagmodles/IGRFWMM.jsp>) using the current International Geomagnetic Reference Field, based on IGRF10. I used MATLAB scripts created by Maurice Tivey (WHOI) to create a prediction of the magnetic field along my profile using fast fourier transforms and linear filtering techniques after Schouten (1971). A magnetic reversal map was created using spreading rate to predict the width of each magnetic anomaly, using a constant magnetization of  $\pm 10$  A/m. I produced two different magnetic lineation maps. The first was created using varying half spreading rates in order to match the peaks of the observed magnetic anomalies; the rates used were 10 km/Ma for 0 - 1.2 Ma, 8.3 km/Ma for 1.2 – 7 Ma, 10.5 km/Ma for 7 – 8 Ma, and 6.5 km/Ma beyond 8 Ma (**Figure 3.11a**). The second was created using a constant half spreading rate of 8.5 km/Ma (**Figure 3.11b**). The published spreading rates on the Kolbeinsey Ridge are quite variable; many workers suggest it has been  $\sim 10$  km/Ma for the last 10 Ma (Applegate, 1997; Kodaira et al, 1998). Others report variable rates between 7.5 – 11 km/Ma from 20 Ma to the present (Mosar et al, 2002; Litvin et al, 1980). A model of the expected magnetic anomalies along the profile is created using the orientation of the profile with respect to the magnetic field and to the magnetic remanence of the rocks with a flat-lying 1 km thick magnetic layer positioned at 1 km depth. The measured magnetic

signal is compared to the model by subtracting the average total field along the profile. I mirrored the predicted magnetic signal about the ridge axis in order to compare the magnetic anomalies on both sides of the ridge.

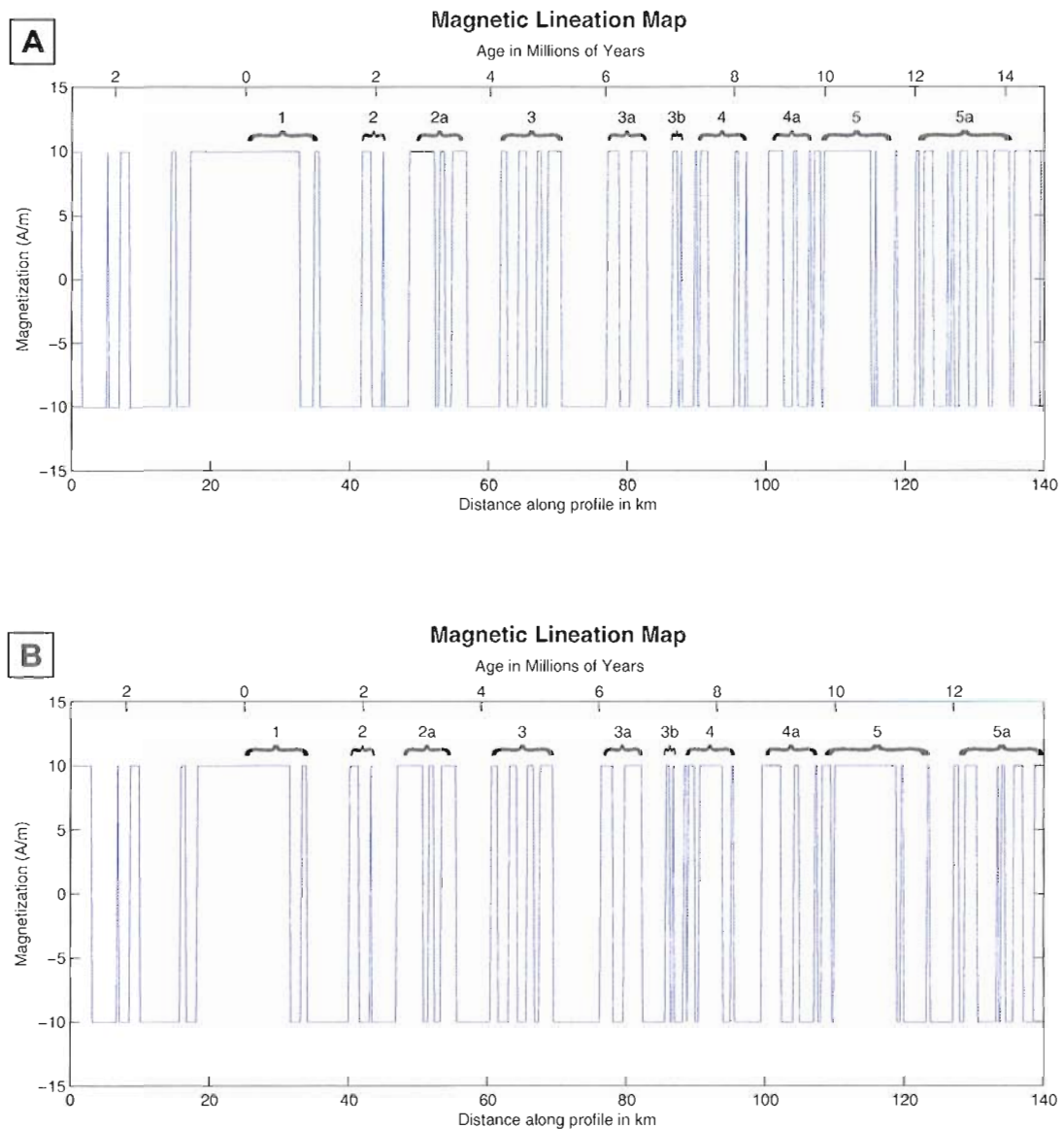


**Figure 3.11:** Maps of magnetic lineations based on the 2004 Geomagnetic polarity timescale. A constant field strength  $\pm 10$  A.m is used for a 1 km thick layer extending from 1 - 2 km depth. Major magnetic chrons are labeled. **a)** Magnetic lineations based on variable spreading rate of: 10 km/Ma for 0-1.2 Ma; 8.3 km/Ma for 1.2 - 7 Ma; 10.5 km/Ma for 7 - 8 Ma; and 6.5 km/Ma beyond 8 Ma. **b)** Magnetic lineations based on a constant spreading rate of 8.5 km/Ma. The upper horizontal axis shows time in millions of years and the lower axis shows corresponding distance along the profile.

## CHAPTER IV

### RESULTS

#### Section 4.1 Seafloor details

The bathymetric profile created from ship soundings shows the spreading center to be a broad region of shallow seafloor extending from 15 to 45 km along the profile, with a minimum depth of ~ 500 m (**Figure 4.1a**). Depth on the western side of the ridge quickly increases to 1 km at lateral distance of <10 km, while, on the east side a similar increase in depth is achieved at distance of nearly 20 km. East of the ridge axis depths stay relatively constant to the eastern end of the profile. This relatively constant depth is interrupted by offsets in three locations – 68, 77, and 108 km along the profile (or 43, 52, and 83 km east of the spreading axis.) These offsets may be due to faulting or they may represent relict axial volcanic centers that have been moved off-axis.

The reflection section also depicts the asymmetry of the spreading axis and the rapid changes in bathymetry (**Figure 4.1b**). Additionally, it reveals a morphological

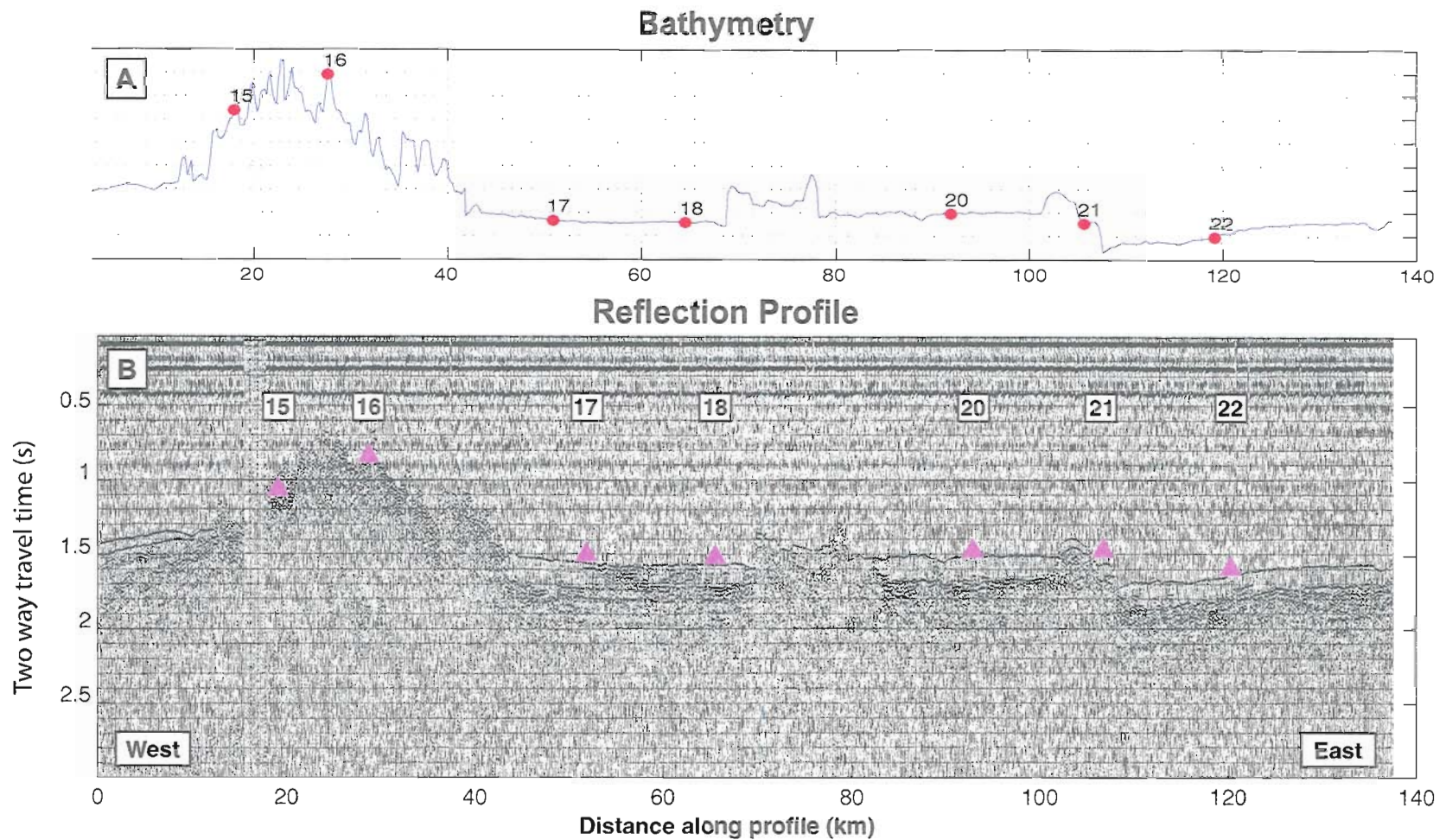


**Figure 4.1:** Bathymetry and reflection profile. **a)** Measured bathymetry along seismic refraction profile, distance along profile in kilometers, and sea floor depth in meters. Station locations are denoted by red stars. **b)** Reflection profile showing two-way travel times of reflections recorded shipboard. Approximate station locations are annotated by pink triangles, with station ID noted in white boxes above.

difference between the two faults in the center of the profile and the easternmost fault. The two central faults appear to be high angle features and form an almost horst and graben structure with the adjoining seafloor. The region between the two faults is slightly recessed. The easternmost bathymetric offset is also fairly high angle dropping about ~200 m over a horizontal distance of 6 km. This fault appears to be on the eastern flank of a rounded intrusion.

In the areas on either side of these faults reflection data shows a second reflector below the seafloor. These areas are low lying relative to adjacent structure and are inferred to represent areas where a thin layer of sediment is overlying the extrusive upper oceanic crust. The maximum two-way travel time (TWTT) of this layer is ~160 ms. Using a *p-wave* velocity of 1.8 km/s, I estimate a maximum sediment thickness of 144 m. In most areas the sediments are thinner than this, with an average thickness of ~120 m. The reflection from the upper layer in most of these areas mimics the underlying reflector and has no visible internal layering suggesting that the sediment cover is fairly homogeneous. There are exceptions, for example between OBS 17 and OBS 18, where there appears to be uneven intrusions of bedrock into the overlying sediment layer. The lack of internal layering may indicate that this thin layer is a lava flow rather than sediment cover, but its even coverage out more than 100 km from the ridge and the interruption by faulting make this determination only speculative with the given information. The lower reflections are of varying thickness and amplitude, as expected for a heterogeneous complex of extrusive material. The uplifted area between the two

central faults may also have a sediment pocket but it is not clear. An additional reflector is visible below the basement at 45-65 km and 85-100 km and is assumed to represent the boundary between extrusive and intrusive material. This reflector has a TWTT below the seafloor of ~300 ms. Assuming a *p-wave* velocity of 3 km/s, this layer is estimated to be ~450 m thick.

There are also multiple reflectors on the flanks of the ridge. Layering is visible in these areas, particularly on the western flank where two bright reflectors overlie the uneven bedrock. The uppermost reflection on the eastern flank resembles those found east of the faults in amplitude, but it is followed by a second, weaker reflection above the bedrock. The reflections on the western flank are much stronger and may be successive lava flows rather than sediments. The sediments on the west side of the ridge are expected to be different due to oceanographic currents and the proximity to Greenland.

Seafloor topography is evident on the OBS record sections as well (**Figures 3.2 - 3.5**). Arrivals from shots over rapid bathymetric changes are clearly offset, particularly between shots 300 and 345 and shots 170 and 200. Arrivals from shots over the ridge are generally more noisy than arrivals from other locations. Many *Pg* and *PmP* arrivals are followed closely by a second arrival of the same amplitude. These arrivals correspond with shots over areas with a sediment cover and are inferred to be a reflection off the sediment – bedrock interface. OBSs 18 – 21 have a region of earlier, higher amplitude *Pg* arrivals between 120 and 130 km, shot numbers 50 – 100, along the profile, coincident with higher amplitude reflections on the reflection section.

## Section 4.2 Crustal thickness

In my series of tomographic inversions I varied the depth and inclination of the starting Moho. While the depth of the initial reflector did have an influence on the final depth of the Moho, the geometry of the Moho and the resultant variations in crustal thickness were similar in every inversion regardless of the starting reflector depth. When comparing the results of two inversions, one with a flat starting Moho at 6 km below the seafloor and the other at 10 km depth, the difference in the estimation of crustal thickness is most pronounced in the center of the profile, with the result from the 6 km starting Moho ~1.5 km shallower (**Figure 4.2**). The model accommodates the observed reflected travel times through this thin crust by putting low velocities in the lower crust. The final RMS and  $\chi^2$  values for the inversion using a 6 km depth starting Moho are 63.5 ms and 8. The deeper starting Moho provides a significantly better fit to the observed travel times (**Table 4.1**) and is in agreement with the previously published estimation of Moho depth at this location on the Kolbeinsey Ridge (Hooft et al, 2006).

The Moho depth varies significantly moving away from the spreading center. My final estimation of Moho depth is the average of the depths generated by the five best-fitting models, with typical errors between 100 – 300 m everywhere except the eastern end of the profile where it exceeds 700 m (**Figure 4.3**). The starting Moho in these models was either flat at 10 km depth or inclined west to east from 10 to 12 km depth (**Table 4.1**).



At the ridge the crust is  $\sim 9.5$  km thick but it quickly shallows to the east, reaching a thickness of  $\sim 7.8$  km in 3.3 Ma crust, about 35 km from the spreading axis. The crust maintains this thickness for  $\sim 20$  km before beginning to thicken again at 5 Ma. The crust continues to thicken to the eastern end of the profile, reaching a maximum estimated thickness of  $12.6 \pm 0.5$  km. This almost 5 km increase in crustal thickness is not accompanied by any bathymetric expression and it may represent a reflector in the upper mantle rather than the Moho.

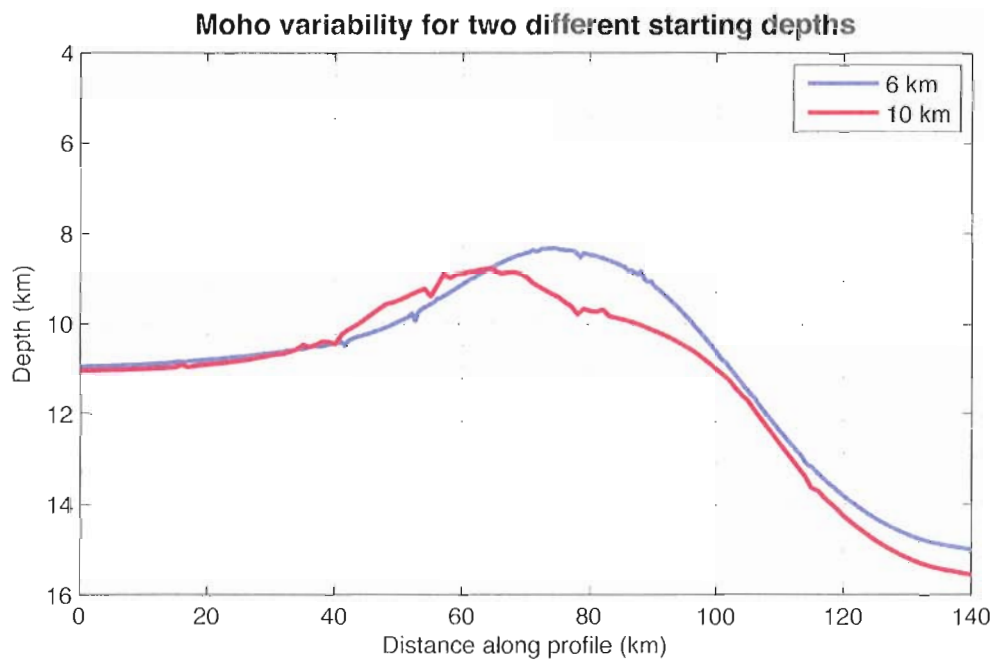


**Figure 4.2:** Comparison of the final Moho depth from two inversions with different starting Moho depths. The initial depths are given in the legend. The inversion shown by the 10 km line is run 155. (See Table 4.1)

| Run       | Starting<br>Moho | Initial rms |            |             | Best-fit rms |            |             | Initial $\chi^2$ |            |             | Best-fit $\chi^2$ |            |             |
|-----------|------------------|-------------|------------|-------------|--------------|------------|-------------|------------------|------------|-------------|-------------------|------------|-------------|
|           |                  | <i>Pg</i>   | <i>PmP</i> | <i>Both</i> | <i>Pg</i>    | <i>PmP</i> | <i>Both</i> | <i>Pg</i>        | <i>PmP</i> | <i>Both</i> | <i>Pg</i>         | <i>PmP</i> | <i>Both</i> |
| 154       | 10 - 12 km       | 98          | 136        | 115         | 36           | 52         | 43          | 43.1             | 57.5       | 49          | 5.6               | 7.1        | 6.2         |
| 155       | 10 km            | 98          | 154        | 123         | 36           | 45         | 40          | 43.2             | 53.7       | 47.3        | 5.6               | 5.1        | 5.4         |
| 156       | 10 - 12 km       | 98          | 136        | 115         | 35           | 44         | 39          | 43.1             | 57.5       | 49          | 5.6               | 4.8        | 5.3         |
| 158       | 10 km            | 33          | 139        | 91          | 30           | 45         | 37          | 4.6              | 42.5       | 19.6        | 3.9               | 5.1        | 4.4         |
| 162       | 10 km            | 98          | 154        | 123         | 32           | 43         | 37          | 43.2             | 53.7       | 47.3        | 4.5               | 4.4        | 4.5         |
| 173 (avg) | N/A              | 33          | 44         | 38          | 32           | 42         | 36          | 4.7              | 4.7        | 4.7         | 4.4               | 4.2        | 4.3         |

**Table 4.1:** Details of five best fitting models that were used to create the final average 2-D model of crustal thickness and velocity. Run 173 was performed using the resultant average velocity structure and average Moho depth. Run 158 used the final velocity model from a *Pg* only inversion for velocity as its starting model. Run 162 used the creeping method, rather than pure jump, to perturb the velocity model.

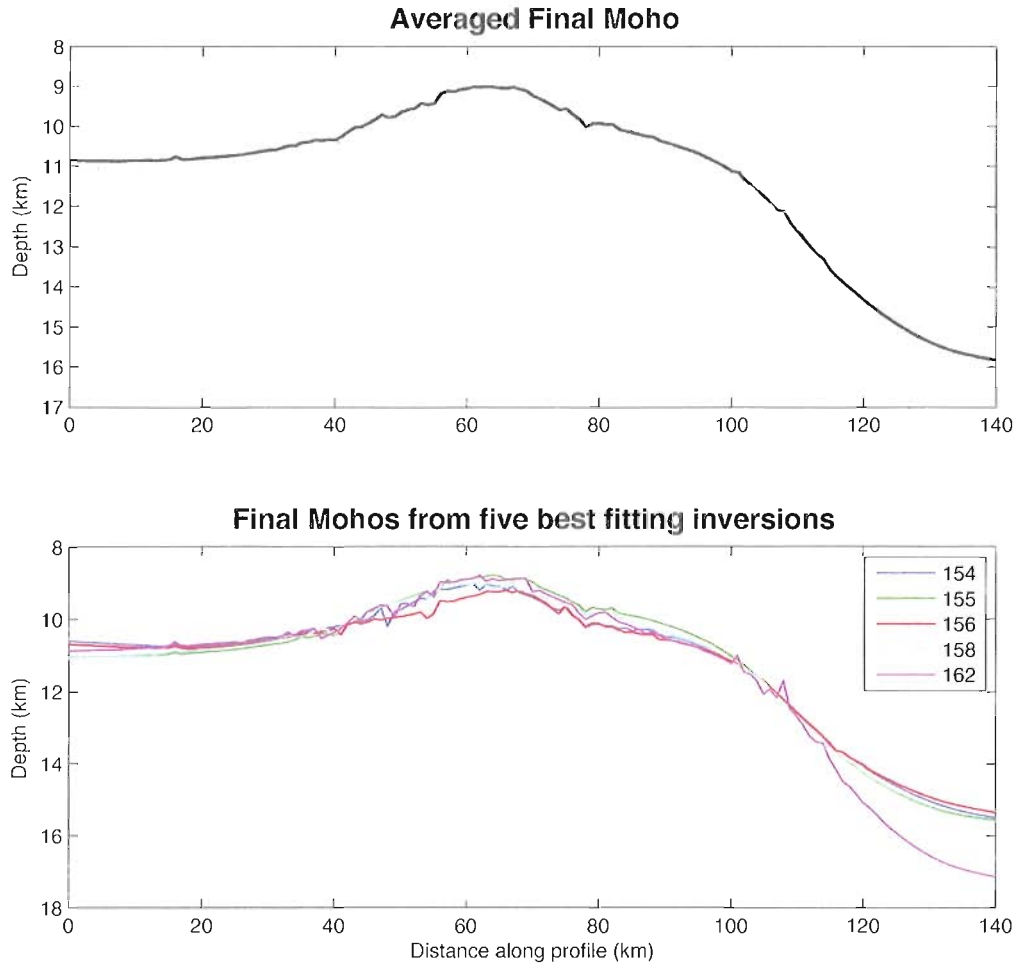


**Figure 4.3:** Final Moho topography. **a)** Final Moho in thick line with standard deviation from best-fitting models shown with gray dashes. **b)** Final Moho from the five best-fitting inversions. Inversion number is given in legend.

### Section 4.3 Velocity model

Over 150 tomographic inversions were performed for velocity structure, using a variety of velocity and depth smoothing weights, velocity and depth correlation lengths, *PmP* weight, and number of iterations, as well as a few different starting velocity models. Several inversions were performed using a starting model that included the sediment layer shown on the reflection section. I varied the velocities of both the sediments and the underlying bedrock, however, the model compensated for the addition of the very slow layer by inserting a thin, anomalously high velocity layer ( $>4$  km/s) directly beneath. There is no geologic evidence to support the presence of this layer. Additionally, a better fit to the data was achieved without the sediments, so they are not included in my starting velocity model. In the uppermost crust the final velocity model is  $\sim 0.2$  km/s slower than the starting model where these sediments are present and faster where there are no sediments. I believe this is a reasonable approximation of the velocity contrast between the sediments and the fractured upper crust.

I first performed the inversion using only *Pg* arrivals to constrain the upper and mid-crustal velocity structure (**Figure 4.4**). The character of the region sampled by *Pg* phases changes very little when the *PmP* arrivals are included. My final velocity model is the average of the five models that best fit the data. These models are all slightly different in small-scale features but the general structure is the same. A contour plot of the standard deviation of the input velocity models from the final averaged model shows that there is only a small misfit between the models, with the greatest value  $\sim 0.06$  km/s

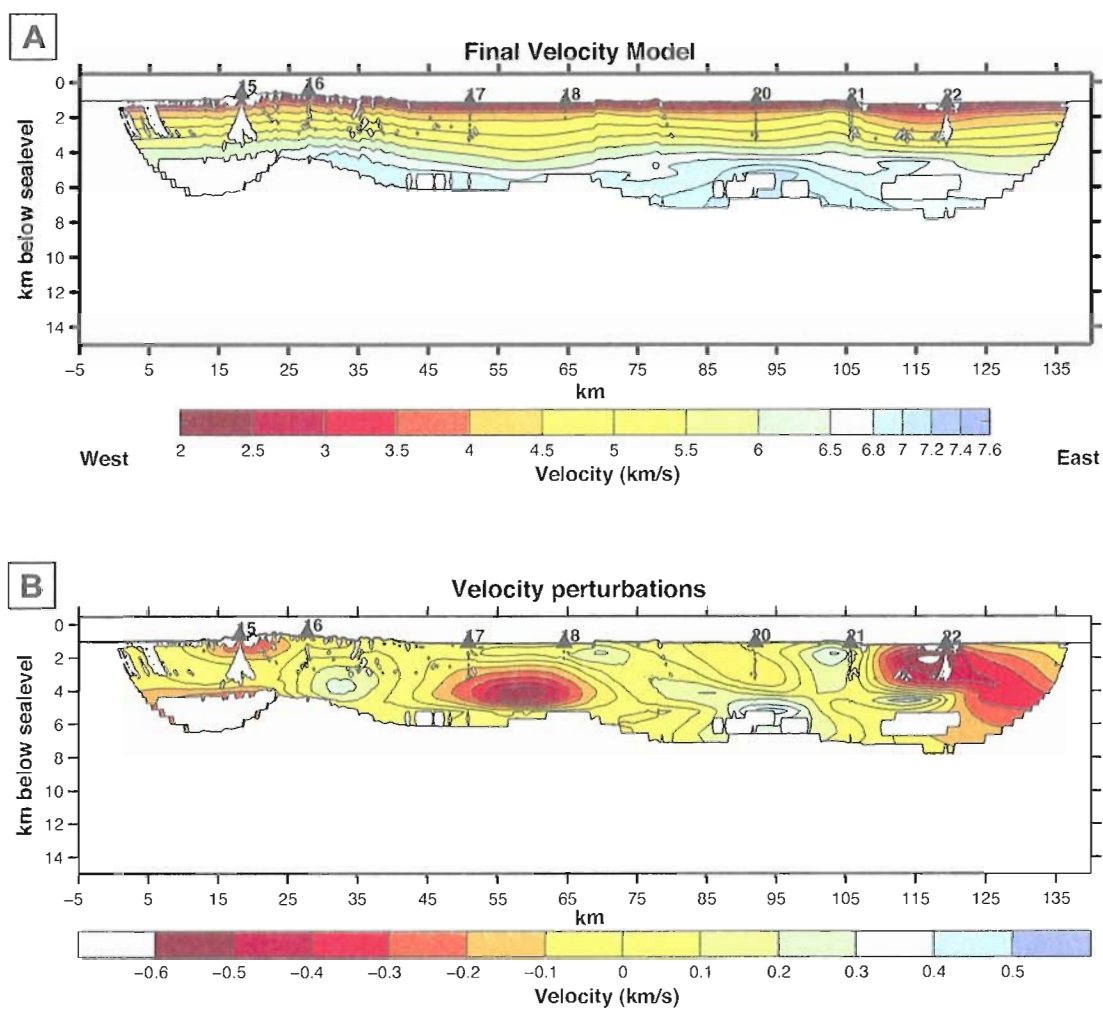


**Figure 4.4:** Final velocity model and velocity perturbations using only  $P_g$  arrivals. **a)** Final upper and mid-crustal velocity model from  $P_g$  arrivals. **b)** Perturbations to starting model. OBS locations are shown with black triangles and bathymetry is given as a thin black line. Both figures have been masked to show only nodes with DWS values greater than 3. See text for discussion.

(Figure 4.5). I used this averaged 2-D velocity profile as the starting model for an additional inversion in order to trace rays through the model. The inversion details and data misfits are shown in Table 4.1. My final velocity model and the perturbations to the starting model are shown in Figures 4.6, 4.7, and 4.8. The travel time residuals for the final velocity model are shown in Figure 4.9. In order to display only the region of the model for which we have sufficient data, these plots have been masked to show nodes that have a derivative weight sum (DWS) value greater than two. The DWS is a measure of the sampling of nodal locations and is a weighted sum of the length of ray paths that influence a given velocity node (Toomey and Foulger, 1989). The resolution above 5 km 5-6 km depth the velocity structure is determined by *PmP* arrivals exclusively. The central area between OBS 16 and 21, 25 – 105 km along the profile, has the best

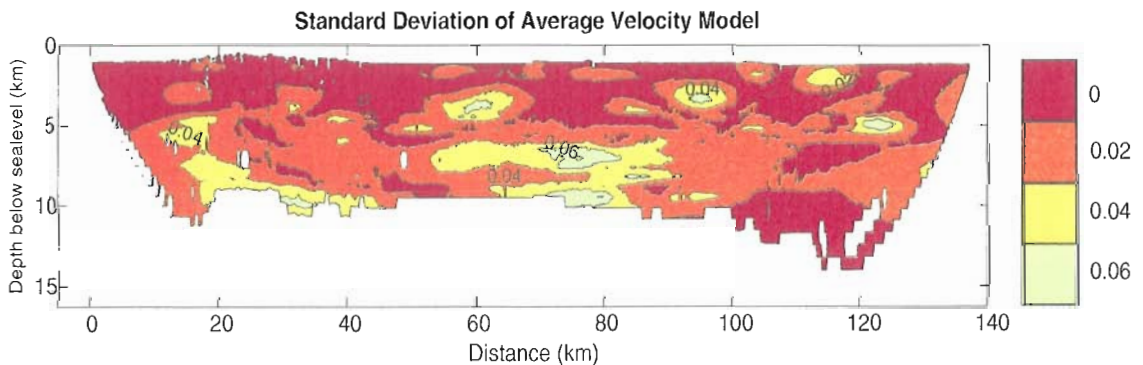


**Figure 4.5:** Contours of standard deviation of average velocity model. The velocity mesh shown has been masked so that only nodes with DWS values greater than two are shown. See text for discussion.

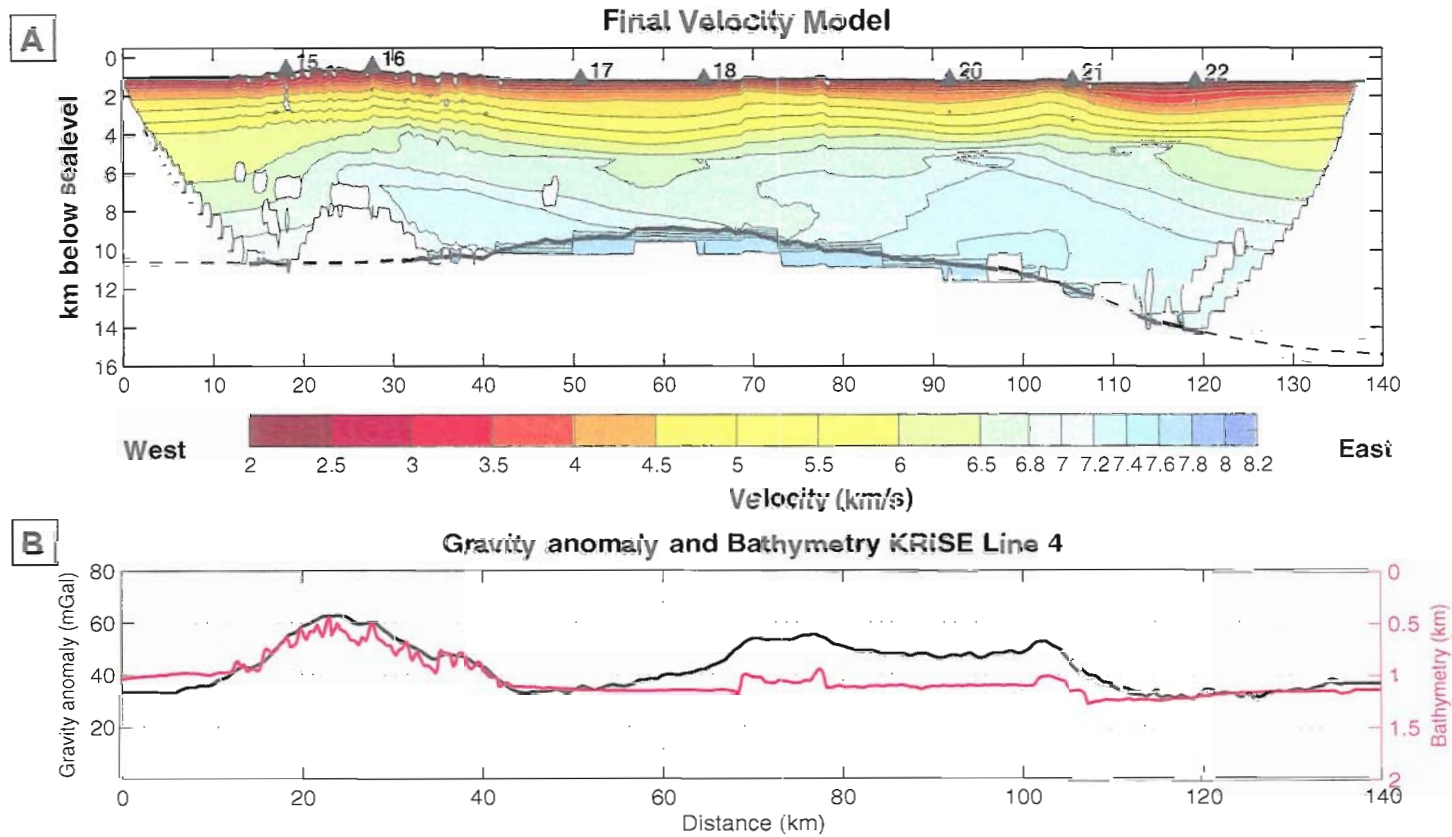


**Figure 4.6:** Final 2-D velocity model with free air gravity and bathymetry. **a)** Final velocity model created by averaging the 5 best fitting models. Station locations are indicated by black triangles. Bathymetry is shown by a thin, black line at the top of the profile. The velocity mesh shown has been masked so that only nodes with derivative weight sum (DWS) values greater than two are shown. An initial, inclined Moho is shown with a thick, gray dashed line. The final Moho is shown in black - with a thick solid line where it is well-constrained by the data or with black dashes where it is inferred. The estimated error to Moho depth is shown with thin, dark gray dashes. **b)** Free air gravity anomaly (black) and bathymetry (red).

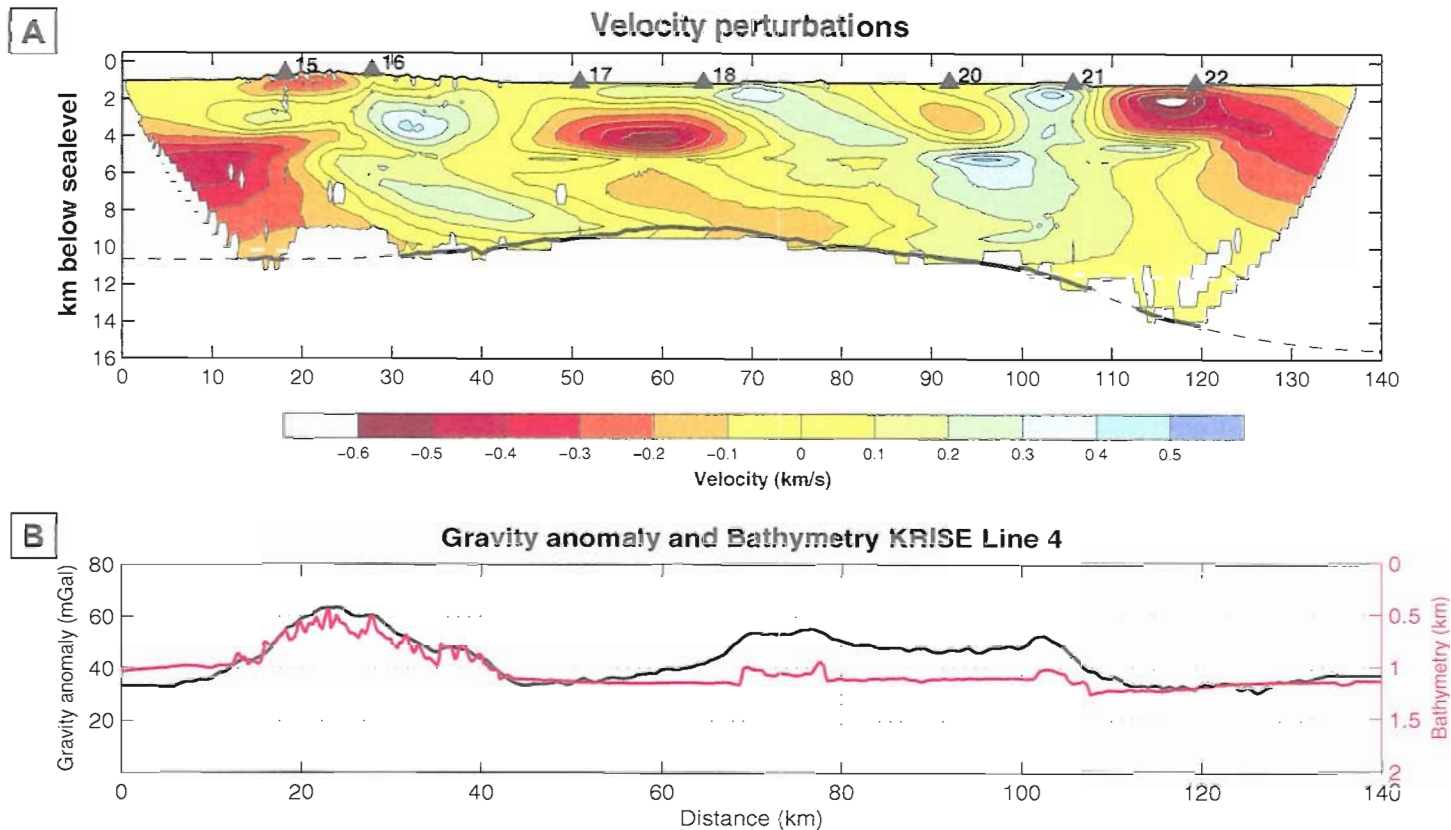


**Figure 4.7:** Perturbations to the starting velocity model, with free air gravity and bathymetry. **a)** Perturbations to starting velocity model. Station locations are indicated by black triangles. Bathymetry is shown by a thin, black line at the top of the profile. The velocity mesh shown has been masked so that only nodes with derivative weight sum (*DWS*) values greater than two are shown (see text). An initial, inclined Moho is shown with a thick, gray dashed line. **b)** Free air gravity anomaly (black) and bathymetry (red).

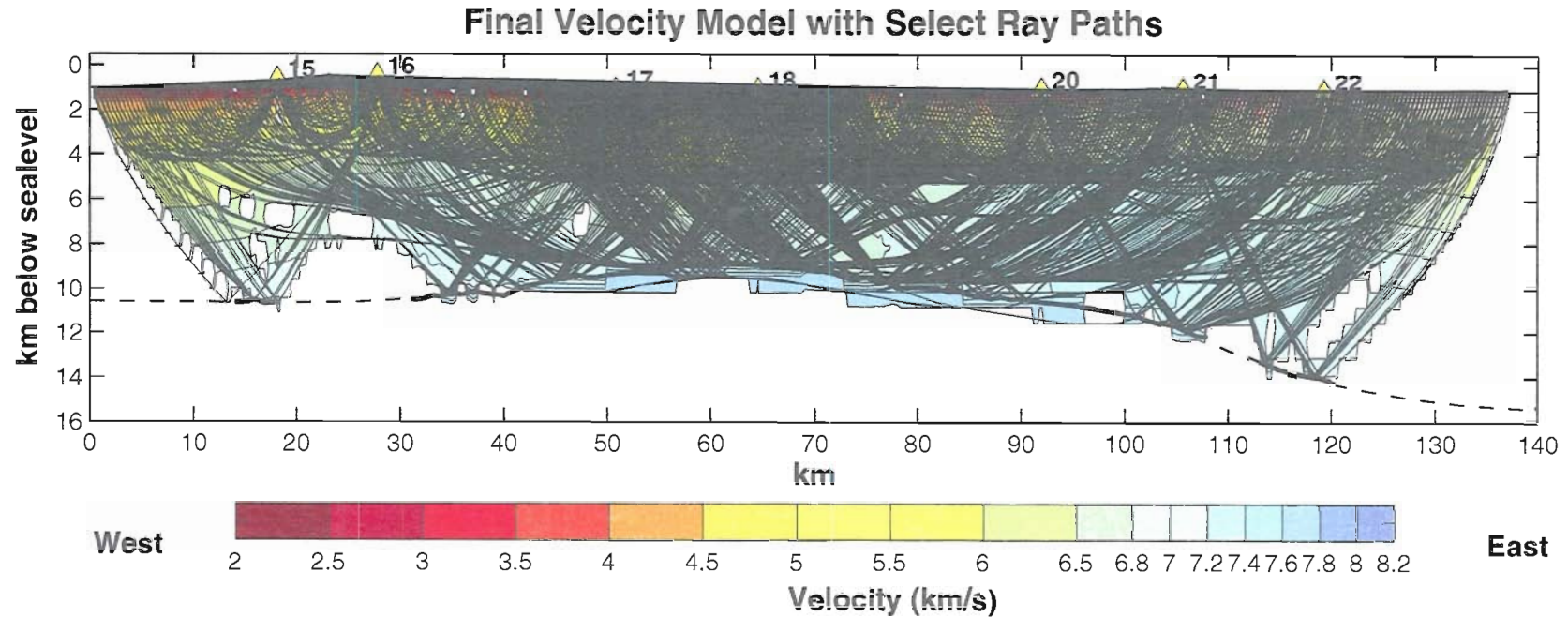


**Figure 4.8:** Final velocity model created by averaging the five best-fitting results, with select rays. Station locations are indicated by black triangles. Bathymetry is shown by a thin, black line at the top of the profile. The velocity mesh shown has been masked so that only nodes with derivative weight sum (DWS) values greater than two are shown. An initial, inclined Moho is shown with a thick, gray dashed line. The final Moho is shown in black - with a thick solid line where it is well-constrained by the data or with black dashes where it is inferred. The estimated error to Moho depth is shown with thin, dark gray dashes. This is overlain with rays estimated through forward modeling. Due to the density of the data, only every 2nd ray is shown.



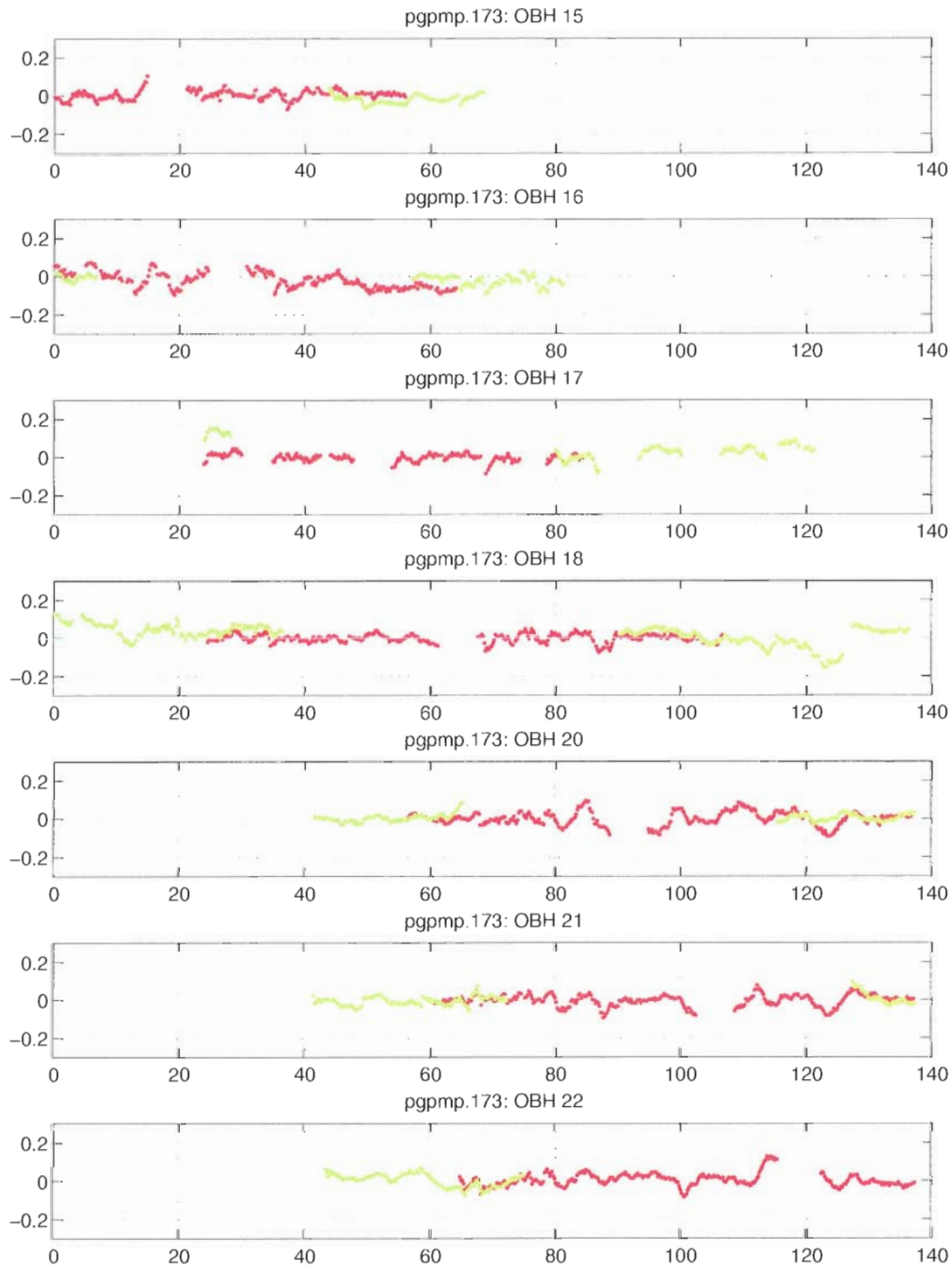


**Figure 4.9:** Travel time residuals for final velocity model. *Pg* residuals shown in red, *PmP* shown in green. Horizontal axis is distance (km) and vertical axis is travel time residual (s).

coverage due to the high number of crossing rays. For ease of discussion I will refer to the ridge axis as a point location 25 km east of the beginning of the profile. The actual lateral extent of the spreading center is estimated to be from 10 – 40 km from the zero point on the profile.

Due to the variability in velocity along the profile I will describe the final velocity model in five parts. The first extends from the western end of the profile to ridge axis, or from 0 to 25 km. The upper crust on this side of the ridge has slightly lower velocities than the starting model, with a minimum velocity of  $\sim 2.04$  km/s at 18.4 km distance along the profile. The lower crust has lower velocities than the starting model, with anomalies up to  $-0.5$  km/s making it as much as 8% slower. There is a  $\sim 1$  km thick layer of slightly elevated velocities separating the upper and lower crust.

The second region begins at the ridge axis and continues down the eastern flank, from 25 to 45 km along the profile. There are similar velocities in the upper 1 km of crust and the velocity increases slightly moving east from the ridge and has values similar to the starting model until distances greater than 25 km from the ridge axis. In the mid- to lower crust there is a region of anomalously high velocities,  $0.3 - 0.4$  km/s higher than adjacent material for a maximum *p-wave* velocity of 6.5 km/s.

East of the ridge the seafloor is fairly uniform until the first fault at 70 km along the profile. The velocities of the upper crust here are slightly faster than the starting model and as much as 0.6 km/s faster than those found on the ridge. Deeper than 1 km

below the sea floor there is a large region of low velocities. It is most pronounced to about 4 km depth, with velocities as much as 0.8 km/s lower than adjacent regions.

The area of the profile between the westernmost fault at 70 km and the eastern fault at 105 km is dominated by high velocity anomalies. The only exception is one small zone of low velocity beneath OBS 20. The high velocity anomalies extend obliquely from the sea floor beginning at 65 km and continue to meet a higher velocity region about 20 km further east at ~4 km depth. The upper portion of this high velocity region coincides with a seafloor offset seen in both the reflection section and the bathymetry and has velocities exceeding 4.7 km/s in the top 1 km. The lower part has velocities that are 0.4 – 0.5 km/s faster than neighboring material with a maximum velocity of ~7.4 km/s at 5 km depth. A fourth high velocity zone exists from 95 - 105 km along the profile. This area is also congruent with an offset structure on the seafloor. The high velocities found here may be explained by a higher amount of intrusives, as found in a seamount, or the uplift of less porous crust by faulting.

The eastern-most 25 km of the profile features anomalously slow velocities, up to 0.6 km/s lower, down to 3 km. East of 115 km on the profile there are no crossing rays so this area is less well constrained than that in the middle of the profile. However, these slow velocities persist even when excluding the arrivals from the closest station, OBS 22 at 119 km along the profile. This is an area that appears to have ~130 m of sediment on the sea floor and perhaps some small component of the slow velocities may be attributed to this. OBS 20 also sits on ~150 m of sediment but I do not see such a dramatic low velocity

anomaly there. A comparison of  $P_g$  arrivals from sources that were 3 – 10 km from the station shows that OBS 22 has much later  $P_g$  arrivals on both sides of the receiver, from 50 to 200 ms later than the other stations. The arrival times of the direct wave through the water column do not show the same timing difference, ruling out the possibility that it is merely a timing error on the station. Below the low velocity region there is a thin sill of high velocity and the lower crust has velocities comparable to the starting model.

Clear  $P_n$  arrivals were observed on four of the OBSs (**Figure 3.2 – 3.7**). Once a final model of 2-D velocity and Moho depth was created, a subsequent inversion was performed using only the  $P_n$  arrivals projected through the final model. Before running the inversion, I adjusted the final model by inserting a mantle  $p$ -wave velocity of 8 km/s at every velocity node below the final estimated Moho (**Figure 4.6**). The mantle velocities determined by the  $P_n$  arrivals range from  $\sim 7.85 - 7.93$  km/s everywhere sampled, from 35 – 90 km along the profile.

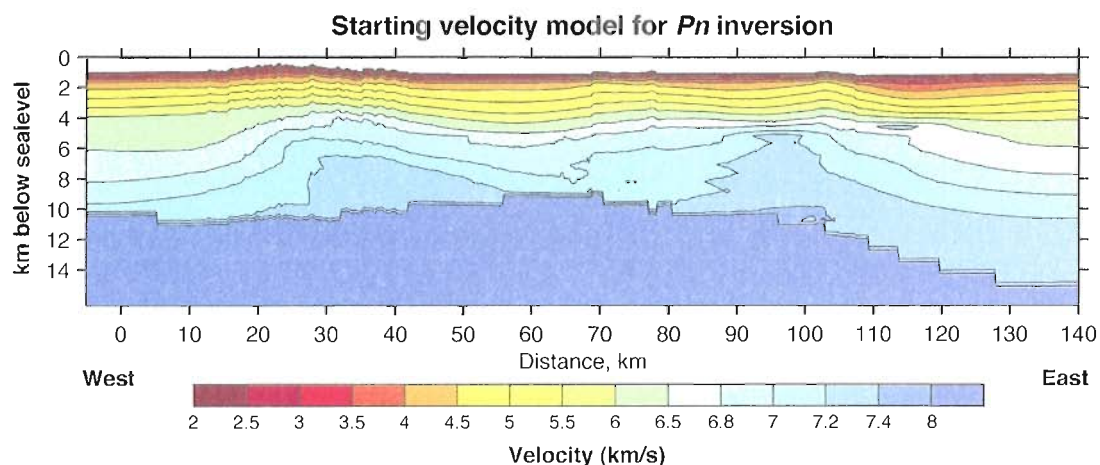


**Figure 4.10:** Starting velocity model used for  $P_n$  inversion. A mantle  $p$ -wave velocity of 8 km/s has been applied to every node deeper than the Moho.

## Section 4.4 Gravity inversion

The free-air gravity has a maximum anomaly of 60 mGal located at the ridge. This is followed by two smaller peaks of ~50 mGal that correspond to the locations of the elevated crust (**Figure 4.6 and 4.7**). Two plots were created comparing the observed free air gravity to the signal predicted by bathymetry, Moho topography, and two different crustal models created using empirically derived relationships between *p-wave* velocity and crustal density (Carlson and Raskin, 1984; Carlson and Herrick, 1990) (**Figure 4.11a, b**). In both of these figures the signal has been normalized by subtracting either the value at the western end of the profile (in the case of free air, seafloor contribution, and Moho contribution) or the mean of the entire prediction (both crustal models). Each predicted gravity signal was subtracted from the observed free air gravity to reveal the residual gravity anomalies (**Figure 4.12a, b**). The Bouguer anomaly is nearly flat across the ridge but remains elevated ~20 mGal in the region between the two faults. After removing the crustal component, the mantle Bouguer anomaly remains flat at the ridge and increases steadily to the east in progressively older crust. Accounting for the effects predicted by a lithospheric cooling model removes most of the signal on the eastern end of the profile but over-predicts the anomaly at the ridge. This is partly due to the bathymetric asymmetry of the spreading axis; the cooling model expects a symmetric ridge. The two gravity predictions made using the crustal models overestimate the signal measured at the ridge and underestimate those at the eastern and western ends of the profile. In the central portion of the profile, both models agree generally with the

measured values. Removing the effects of lithospheric cooling flattened the gravity anomaly at the eastern end of the profile but left a large residual anomaly west of the ridge. Since the gravity estimations are acquired by padding the eastern and western ends of the profile for 100 km with the same depth, rather than the actual bathymetry, some of the discrepancy may be attributed to the modeling technique.

#### **Section 4.5 Magnetic signal**

The highest magnetic values are located at the zone of crustal generation, with a strong positive anomaly of 2500 nT (**Figure 4.13**). This is followed by a strong negative anomaly reaching values  $\sim -2000$  nT. Beyond 1.5 Ma age crust the magnetic anomalies are clear but with lower amplitudes around  $\pm 1000$  nT. These amplitudes continue off axis for 60 km into 6.7 Ma crust, through chron 3A. Beyond this point, the signal is attenuated to the range of  $\pm 500$  nT. The best fit to the measured wavelengths was obtained by using a variable spreading rate. Two magnetic models with different variations in spreading rate were created (**Figure 3.5**). The best fit to the observed signal was achieved using the following half-spreading rates: 10 km/Ma for 0 – 1.2 Ma, 8.3 km/Ma for 1.2 – 7 Ma, 10.5 km/Ma for 7 – 8 Ma, and 6.5 km/Ma from 8 – 15 Ma. This extremely slow spreading rate in 8 – 15 Ma crust is in conflict with commonly accepted rates on the Kolbeinsey Ridge. To address this, an alternate magnetic model was created using a constant half rate of 8.5 km/Ma. Using this model, from the ridge to chron 3A, the peaks of the predicted anomalies are in general agreement with the locations of the peaks of the measured

anomalies. Beyond 3A, there is no match between the predicted and measured peaks and troughs. At the eastern extent of the profile, the anomalies appear anti-correlated with the predicted signal.

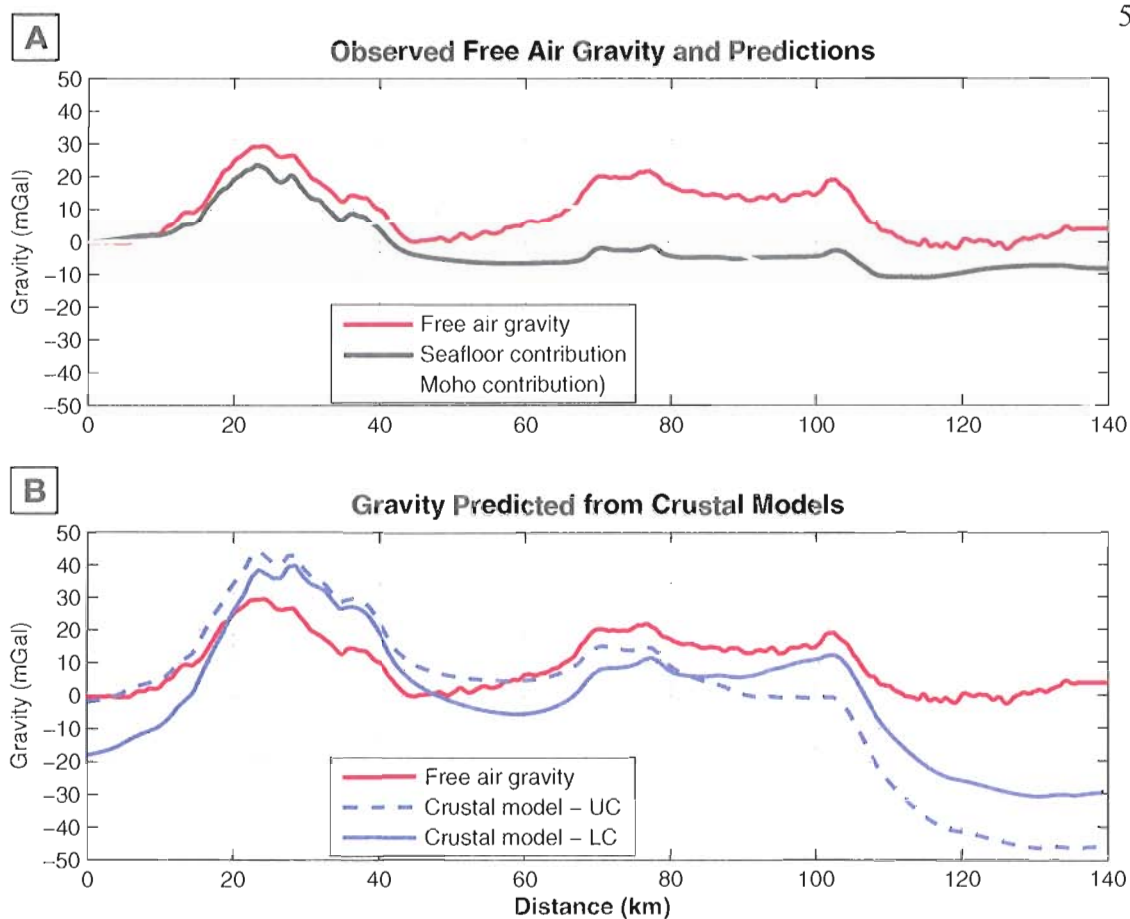


**Figure 4.11:** Observed and predicted gravity. **a)** Observed gravity, shown in bold red line, has been reduced by subtracting the value of the first measurement from the rest. Seafloor (black) and Moho topography (light blue) contribution estimated using Parker 2-D approximation, also reduced by subtracting the first value. **b)** Crustal models show gravity results from the laterally varying crustal models; UC - upper crustal values used for whole crust; LC - upper and lower crustal values used. Observed free air gravity shown in thick red line.



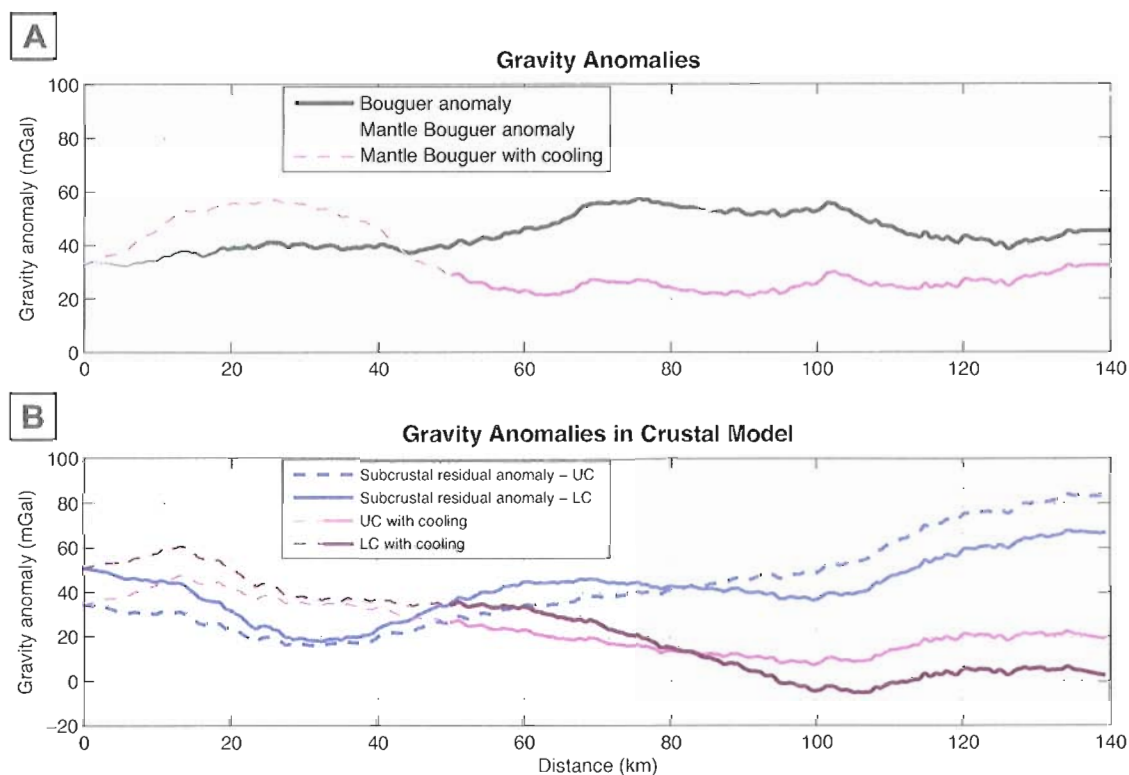


**Figure 4.12:** Gravity anomalies. **a)** Bouguer anomaly (black) and mantle Bouguer anomaly (light blue) estimated by removing predicted signal due to bathymetry and Moho topography. The signal is further reduced by subtracting the gravity anomaly predicted by a lithospheric cooling model from the mantle Bouguer anomaly (magenta). **b)** The Subcrustal residual anomalies estimated by removing signal predicted by laterally varying crustal models. The upper crustal density model (UC) is shown with a thick, dashed blue line. The model using both upper and lower crustal densities (LC) is shown as a thick blue line. These are both further reduced by removing signal predicted by a lithospheric cooling model (magenta for UC, purple for LC). In both figures, the gravity predicted including the cooling model is displayed by thinner, dashed lines at the ridge where the isotherms are inaccurately represented by the cooling equation.

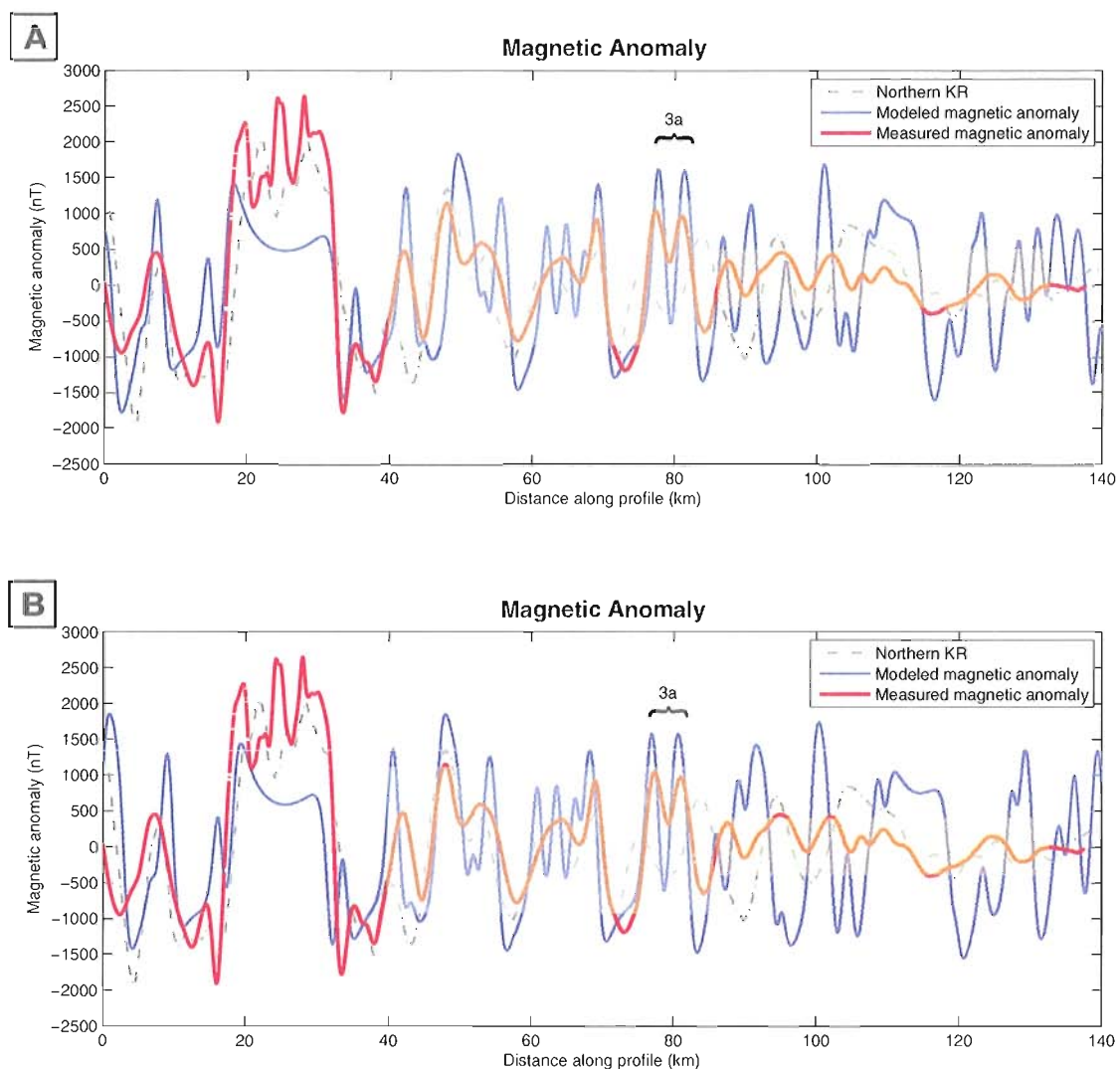


**Figure 4.13:** Observed magnetic anomalies on the southern Kolbeinsey Ridge plotted over two magnetic models created with different spreading rates. In both figures observed magnetic anomalies are shown in red, modeled anomalies in black, and the results shown in Kodaira et al (1998) in gray dashes for comparison. Blue box highlights region with stronger signal strength and yellow box highlights region with reduced signal strength. Magnetic chron 3a is labeled in both. **a)** The following half spreading rates were used: 10 km/Ma for 0-1.2 Ma; 8.3 km/Ma for 1.2 - 7 Ma; 10.5 km/Ma for 7 - 8 Ma; and 6.5 km/Ma beyond 8 Ma. **b)** This is a more simple model with a half rates of 8.5 km/Ma. See text for discussion.

## CHAPTER V

### DISCUSSION

#### Section 5.1 Crustal velocity structure

The lower *p-wave* velocities beneath the western side of the spreading center are in agreement with those expected in an area with extensive fracturing in the upper crust and a small percentage of melt. The higher velocities in the middle crust on the east side of the ridge may represent a large cooled intrusive body that has a lower porosity and/or a greater density than the neighboring crust. The broad region of high *p-wave* velocity extending from 65 to 105 km along the profile (45 to 80 km east of the ridge) may be explained by the presence of either faults or seamounts. If the offset is due to faulting, it has resulted in an uplift of ~150 m relative to the adjacent seafloor. The velocity gradient in the upper crust is quite steep and this small amount of uplift is sufficient to bring up higher velocity rocks with lower porosity and a higher intrusive content (**Figure 5.1**). The bathymetric offsets could also be small seamounts, which would have a high amount of intrusive material, and faster *p-wave* velocities.

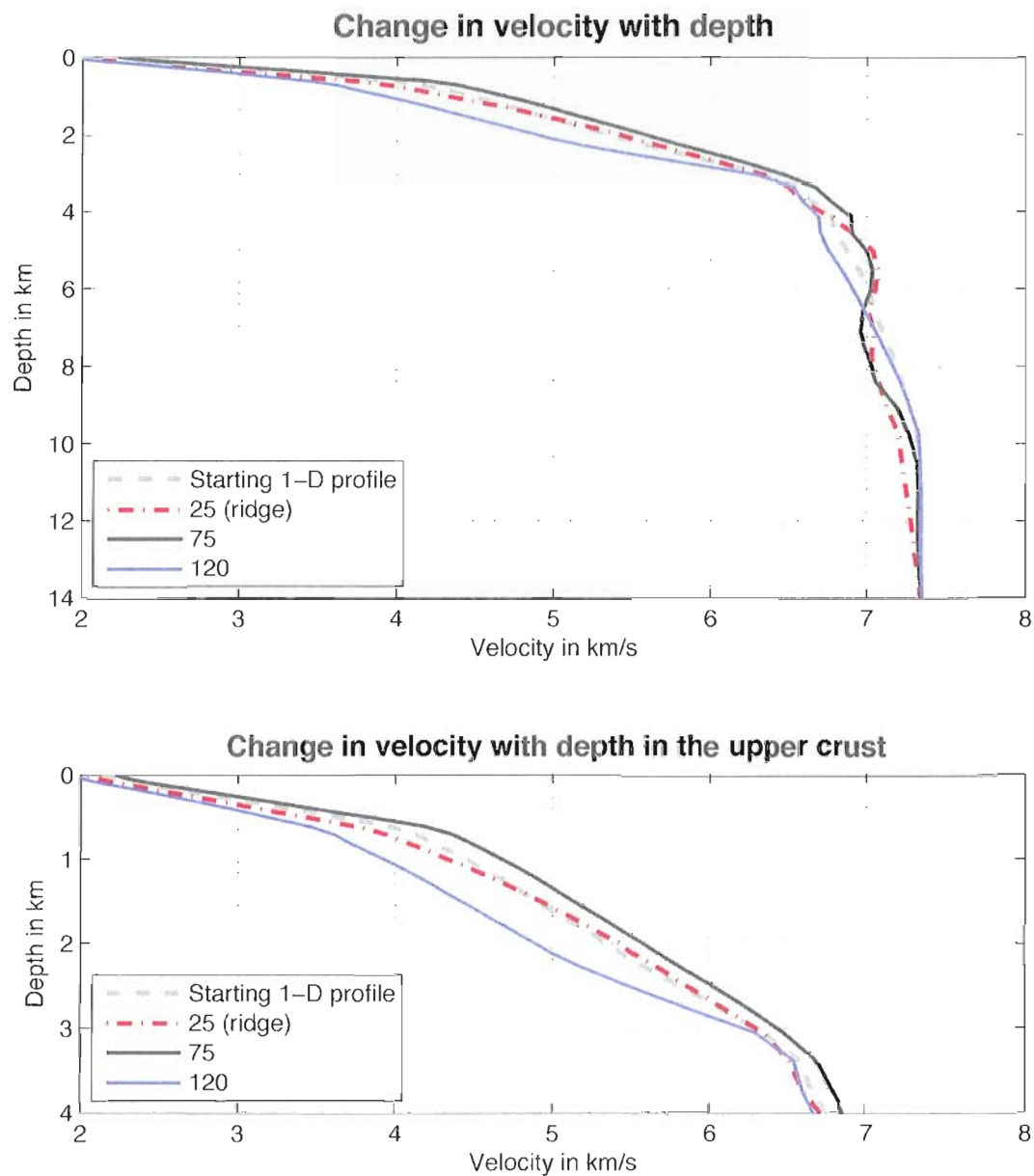


**Figure 5.1:** Plot of change in velocity with depth for final velocity model. Numbers indicate horizontal location along the profile in km. The velocities at the ridge are shown with red dashed line. The initial 1-D velocity model is shown in gray dashes. The black line shows velocities through the thin crust in the middle of the profile and the blue line shows those through the thickest crust at the eastern end. The lower plot is the same data, zoomed into the upper 4 km.

A portion of the large, low velocity region at the eastern end of the profile may be the result of a thicker than typical extrusive layer, however, the low velocities persist to 3 km depth, which is too thick to be excess extrusive material. I suggest that increased porosity due to extensive, post-emplacement faulting is the cause for these low velocities continuing to that depth. The higher porosity may have also allowed for a greater degree of hydrothermal alteration, further reducing velocities in the mid-crust. One mechanism for the proposed faulting is ongoing rotation of the crustal material, as is seen in overlap basins between the ends of offset ridge segments, either an OSC or NTO, discussed below.

In order to easily compare my final velocity model to Smallwood and White (1998) and Kodaira et al (1998), I adapted their velocity models into my plotting scheme. This was done by manually picking velocity contours from their images. I created a laterally homogeneous “starting” velocity model for each by subtracting basement elevation from the depth of the velocity contours and averaging the value at each depth node (**Figures 5.2, 5.3, 5.4**). Using this averaged model, I created plots of velocity perturbations to reveal regions with anomalous velocity. The range of velocity perturbations for all of the models is similar although there is some variety in the locations and ages of the anomalies. I have also included the free air gravity anomaly and bathymetry along each profile to facilitate comparison between crustal velocities, which are presumed to be indicative of density variations, and gravity anomalies.

On the Reykjanes Ridge, both CAM 72 and CAM 74 have high velocities at the east end, in the location of the gravity trough. CAM 72 has a mid-crustal high velocity anomaly that is similar to the one found on the eastern side of the ridge on KRISE Line 4; both may represent a cooled intrusive body formed at the ridge axis. On both profiles there is a good agreement between bathymetry and free air gravity. Since crustal thickness is not constrained on CAM 72, it is difficult to positively associate the gravity anomalies with crustal thickness variations. However, it is clear that they are correlated with bathymetric undulations.

On the northern Kolbeinsey Ridge, the L3 profile shows alternating regions of high and low velocity that appear to persist throughout the crustal column. Near the ridge axis, there is a good correlation between bathymetry and free air gravity. The high gravity anomaly between 140 and 160 km is not associated with elevated bathymetry but does correspond to a region of higher *p-wave* velocities, and presumed higher density crust. The two high gravity anomalies in the middle of the profile, from 60 - 80 km and 100 - 120 km, cannot directly be related to changes in bathymetry although there are nearby undulations that may be influencing the gravity signal. These two anomalies are in regions of lower velocity crust and so cannot be explained by the presence of higher density material. Kodaira et al interpreted these undulations in velocity as variations in thickness of layers 2A and 2B. Their study did not investigate the origin of the free air gravity anomalies on the northern Kolbeinsey Ridge.

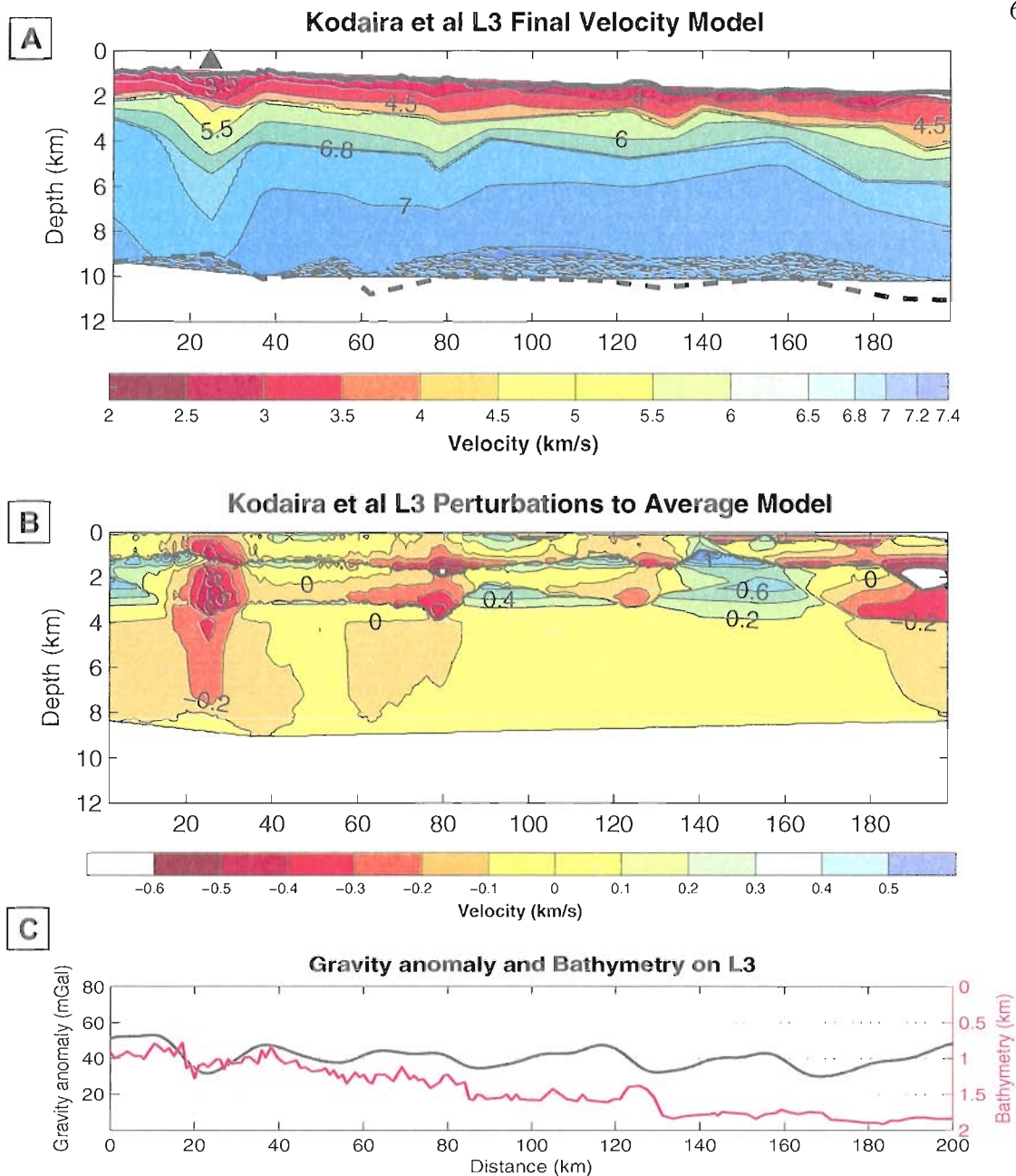


**Figure 5.2:** The 2-D velocity model with gravity and bathymetry for 200 km of Kodaira et al's L3 transect on the northern Kolbeinsey Ridge. **a)** Velocity contours were picked from the published image and plotted using the color scheme of my velocity models. A laterally homogeneous model was created by averaging values across the profile. The location of the ridge is indicated with a black triangle. **b)** The perturbations shown are to the average model. Due to the layered method that Kodaira used, there are sharp velocity contrasts across layer boundaries. **c)** Gravity (black) and bathymetry (red). Reproduced from Kodaira et al (1998). Gravity from Sandwell and Smith (1997).

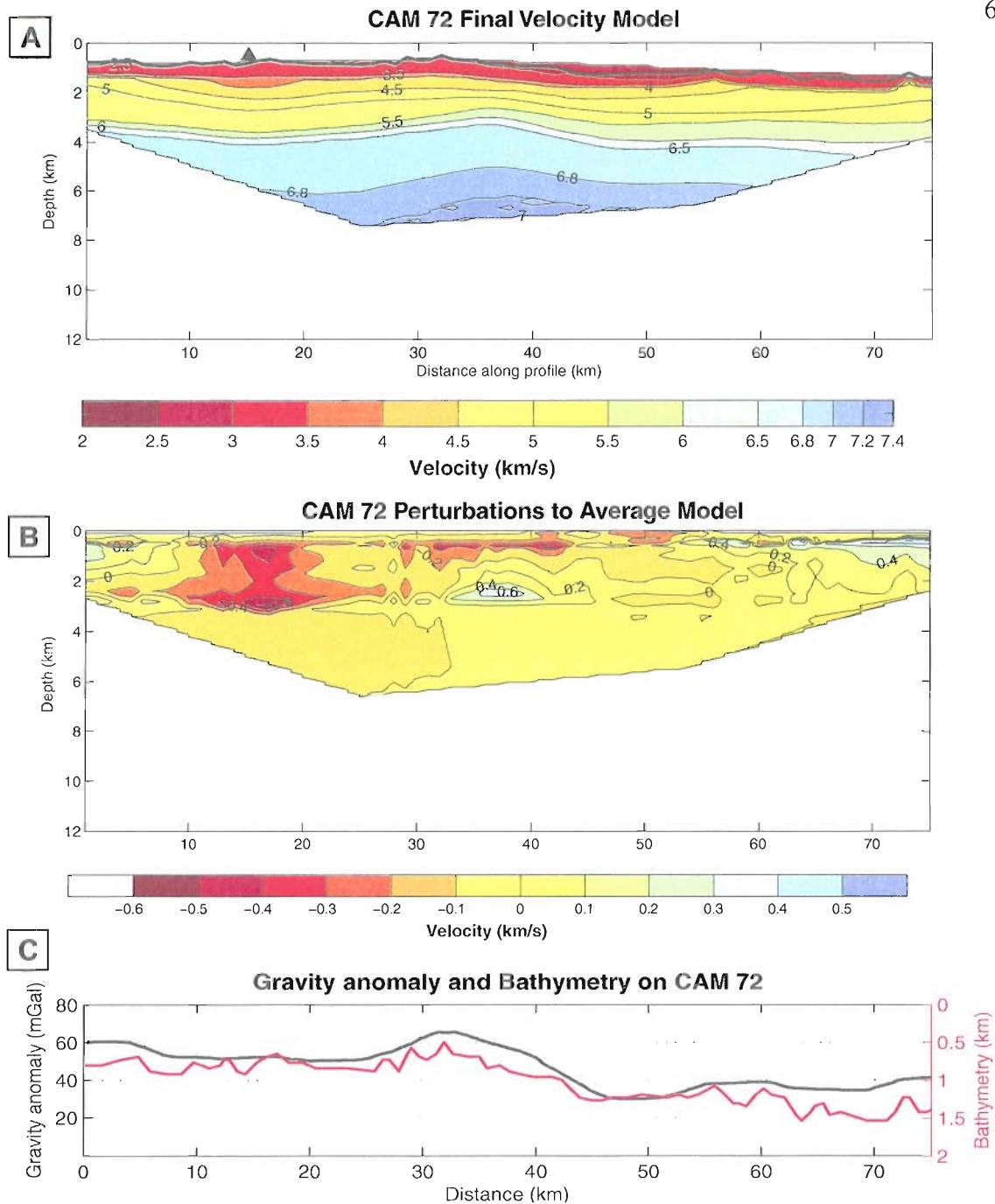


**Figure 5.3:** The 2-D velocity model with gravity and bathymetry for Smallwood and White (1998) CAM 72. **a**) Velocity contours were picked from the published image and plotted using the color scheme of my velocity models. A laterally homogeneous model was created by averaging values across the profile. The location of the ridge is indicated with a black triangle. **b**) The perturbations shown are to the average model. **c**) Gravity (black) and bathymetry (red). Reproduced from Smallwood and White (1998).



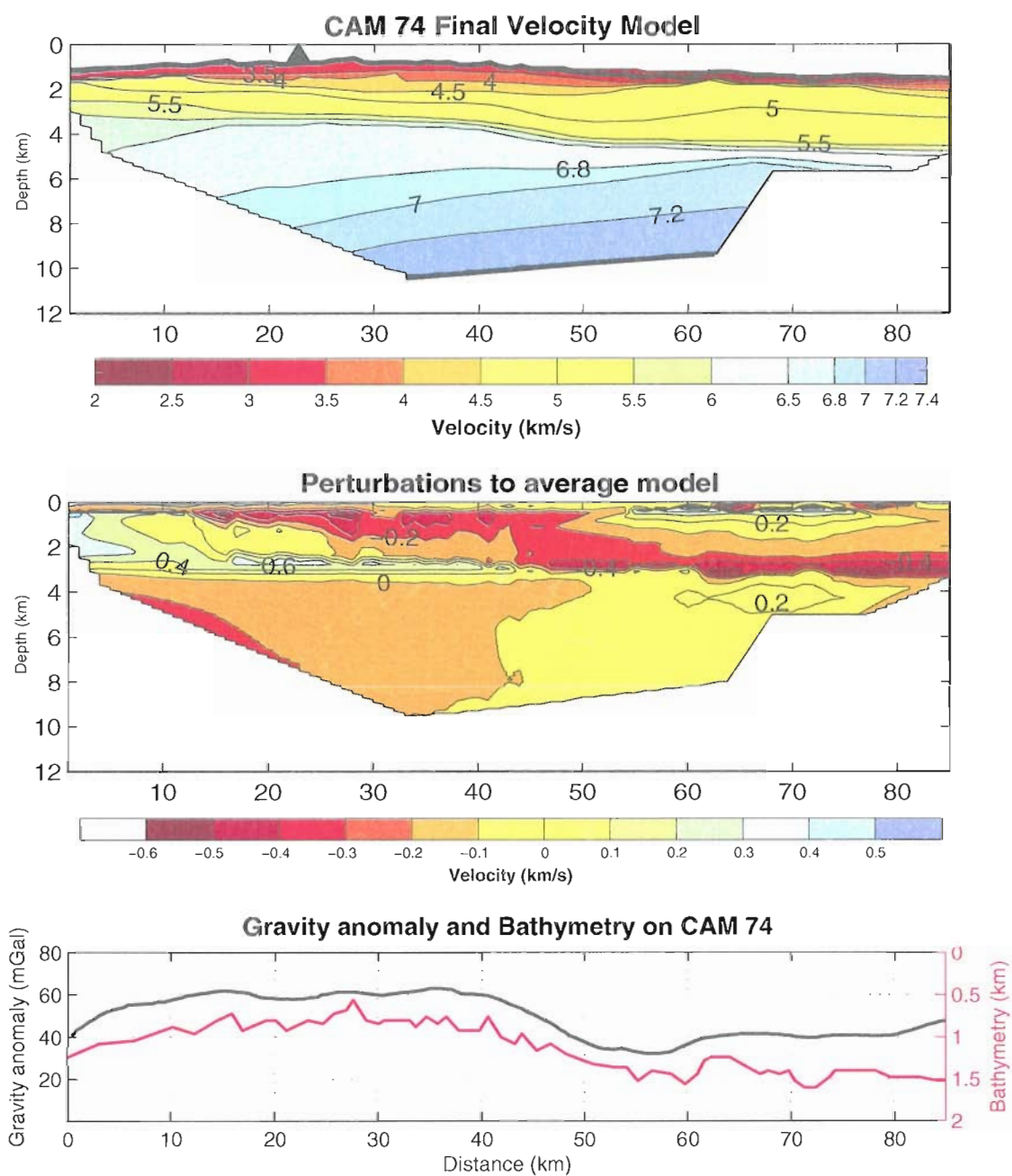


**Figure 5.4:** The 2-D velocity model with gravity and bathymetry for Smallwood and White (1998) CAM 74. **a)** Velocity contours were picked from the published image and plotted using the color scheme of my velocity models. A laterally homogeneous model was created by averaging values across the profile. The location of the ridge is indicated with a black triangle. **b)** The perturbations shown are to the average model. **c)** Gravity (black) and bathymetry (red). Reproduced from Smallwood and White (1998).

## Section 5.2 Topographic support

The large variation in crustal thickness at the eastern end of the profile does not have the expected compensatory variation in bathymetry. In order to calculate the expected bathymetry for my estimated crustal thickness and structure I created a 2-D model of crustal density variations predicted by *p-wave* velocities according to the relationships described by Carlson and Herrick (1990). I used the average density of the column of crust at each node with its thickness to predict the thickness of mantle below and water above. I used a depth of compensation of 30 km and a homogeneous mantle with a density of  $3300 \text{ kg/m}^3$ . I used different locations along the profile as the reference point in isostatic equilibrium; the result shown is calculated using 55 km as this point. The resultant plot of predicted bathymetry shows that the bathymetry at the eastern end of the profile should be ~550 m below sea level, 600 m shallower than the actual sea floor (**Figure 5.5**). I also created a prediction of Moho depth from the measured bathymetry and modeled crustal structure (**Figure 5.6**). The predicted crustal thickness at the eastern end of the profile is only about 8 km. I did not account for the change in density of the mantle lithosphere due to cooling. The ridge is also out of isostatic equilibrium but it is expected to be supported dynamically due to the ongoing uprise of new material generated by decompression melting.

The region of thickened crust is at the eastern end of my profile and the result is less well constrained than that from the middle of the profile due to fewer crossing rays. However, the *PmP* arrivals that suggest a deeper reflection are very clear and are

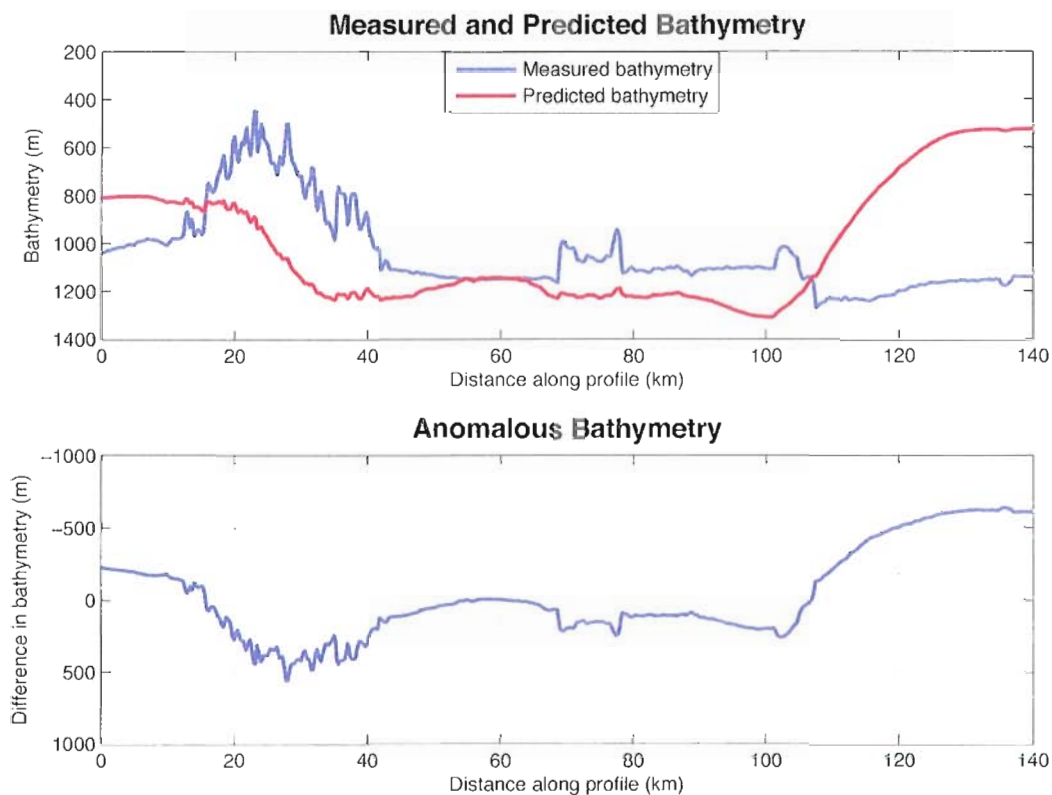


**Figure 5.5:** Observed, predicted, and anomalous bathymetry. **a)** The predicted bathymetry was calculated using the relationships between  $p$ -wave velocity and density described by Carlson and Herrick (1990) with modeled crustal velocities and thickness. **b)** A plot of the difference in observed and predicted bathymetry; negative anomaly indicates that the seafloor is deeper than predicted by crustal velocity structure and thickness alone.

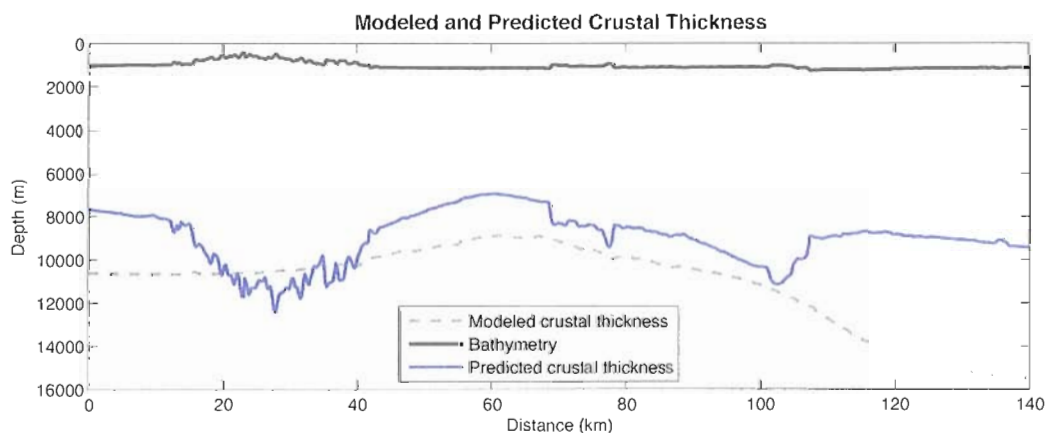


**Figure 5.6:** Crustal thickness predicted from bathymetry and crustal velocity. The final modeled Moho is included as gray dashes.

recorded on three stations. If the estimated crustal thickness is accurate, the bathymetric anomaly may be explained by dynamic support or lithospheric strength. The lack of data further to the east limits my ability to resolve the mechanism for this. If off profile bathymetry data revealed that the thickened crust was only a few 10s of kilometers in diameter, the low region might be supported by the strength of the lithosphere. Alternatively, anomalously dense material in the upper mantle below the thickened crust may serve to pull it out of isostatic equilibrium.

An alternative view may be taken if I accept that the crustal thickness for this part of the profile is overestimated. If the source of the reflected arrivals that are inferred to represent the Moho is actually within the upper mantle, the crust would appear unusually thick. The lack of reflection at a lesser depth suggests that the actual crust-mantle transition is gradual rather than distinct. If the crust has experienced significant fracturing due to rotation and/or shear, pathways may be opened into the mid- and lower-crust. This would allow fluids to permeate, resulting in alteration of the crust and, possibly, upper mantle. Alteration of basalt results in the formation of serpentinite with significant amounts of magnetite. If the new magnetite is formed during a period with the opposite magnetic polarity of the original basalt, the total observed magnetic anomaly would be lower. The lower velocities and decayed magnetic amplitudes in this region support this hypothesis.

### Section 5.3 V- shaped ridges

The free-air gravity anomalies from satellite altimetry along the Reykjanes and Kolbeinsey Ridges have similar values of  $\sim 50 - 60$  mGal (**Figure 1.3**). The troughs between the high gravity anomalies also have similar magnitudes north and south of Iceland, with values ranging from  $\sim 20 - 35$  mGal (Sandwell and Smith, 1997). On the Reykjanes, Smallwood and White (1998) report that both CAM 72 and CAM 74 show higher anomalies on either side of the ridge than at the ridge axis. It is generally believed that the peaks and troughs in the free-air gravity are associated with bathymetric undulations. On the Reykjanes Ridge, the V-shaped bathymetric and gravity anomalies are inferred to be isostatically supported by thicker crust and record changes in melt production due to the along-axis migration of a series of pulses of hot material from the Iceland plume (Smallwood and White, 1998; Jones et al, 2002; Poore et al, 2009).

On the northern Kolbeinsey Ridge there do not appear to be significant variations in crustal thickness (**Figure 2.3 and 5.2**) in the location of the high gravity anomalies (Kodaira et al, 1998) (**Figure 5.7**). The L3 profile crosses several gravity highs with values of  $40 - 50$  mGal but the correlation between these highs and bathymetry is inconsistent. There is general agreement between free air gravity and bathymetry from the west end of the profile to  $\sim 100$  km. There are fluctuations in bathymetry on the order of  $100 - 200$  m but they are not large enough to explain the entire gravity anomaly. The gravity high located between  $140 - 160$  km is in a region with relatively flat bathymetry; however, it is over a region with high *p-wave* velocities throughout the crust.

On the southern Kolbeinsey Ridge, I find that in the location where the V-shaped high gravity anomaly crosses my profile, from 70 – 105 km distance, the seafloor is offset vertically at 68 – 78 km and 100 – 108 km by faulting or the presence of volcanic features, with deeper sea floor between the offsets. The amount of offset, <200 m, can only be expected to result in a ~5 - 10 mGal anomaly (**Figure 4.9**). The Bouguer anomaly in this area is still 15 - 20 mGal greater than the rest of the profile (**Figure 4.10**). The Moho depth in this region ranges from 7.8 – 10.5 km with no apparent correlation between bathymetry and crustal thickness. In contrast to the Reykjanes Ridge, neither segment of the Kolbeinsey Ridge has thicker crust associated with the off-axis diachronous gravity anomalies.

A potential origin for the gravity anomalies is the presence of more dense material in the crust. Isotopic evidence suggests that the Tjörnes fracture zone serves as a mechanical boundary restricting direct access of plume material to the Kolbeinsey Ridge and prohibiting mixing (Mertz et al, 1991). An analysis of the geometric evolution of the Kolbeinsey Ridge reveals a potential relationship between the orientation of ridge segments and pulsation within the plume (Abelson and Agnon, 2001). During periods of increased flux, an instability may form in the plume, resulting in a secondary branch leaving the plume stem to the north (**Figure 5.8**). This secondary branch leaves the plume at a greater depth than the material supplied to the south and may be compositionally different. The authors discuss spatial trace element variability associated with proposed

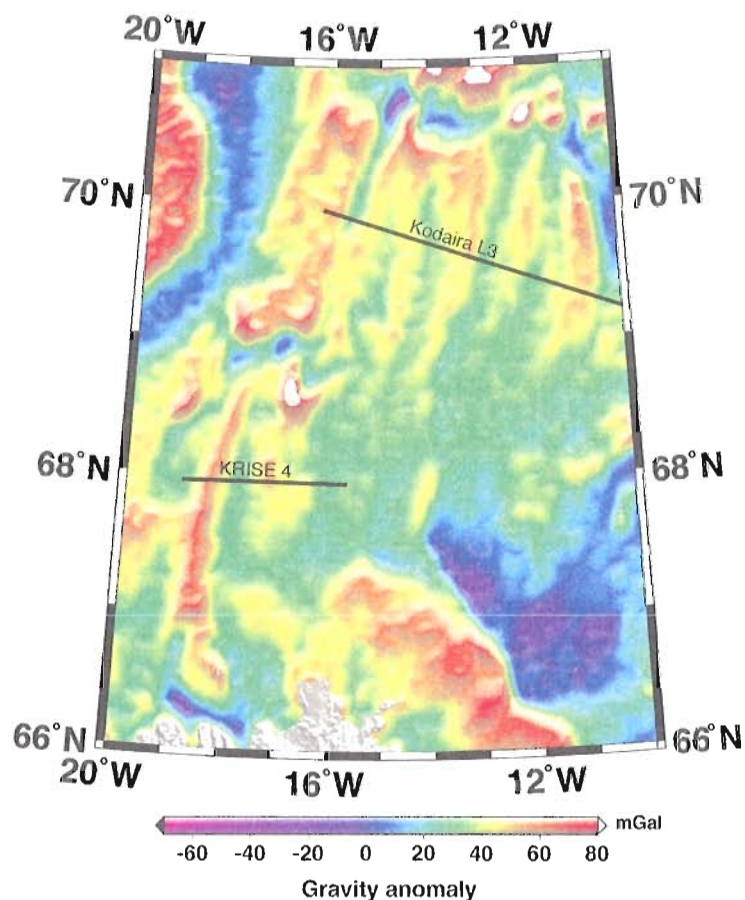


**Figure 5.7:** Gravity anomalies on the Kolbeinsey Ridge. The locations of KRISE Line 4 and Kodaira et al's L3 are included.

plume pulses but do not discuss changes in major element concentration. A deeper branch of the plume would be expected to source a more primitive mantle and result in basalt that is more enriched in magnesium than a basalt with a shallower source. The periods of plume pulsation are recorded on the Kolbeinsey Ridge by an end-to-end alignment of the ridge segments, while periods of normal flux are characterized by a counterclockwise

rotation of the ridge segments and more pronounced ridge segmentation (**Figure 5.9**). On the northern Kolbeinsey Ridge, two of the periods of pulsation identified by Abelson and Agnon appear to correlate with crust with higher *p-wave* velocities, from 40 – 60 km and 85 – 110 km. These higher velocity regions are located in gravity troughs, indicating that they are less dense than neighboring crust.

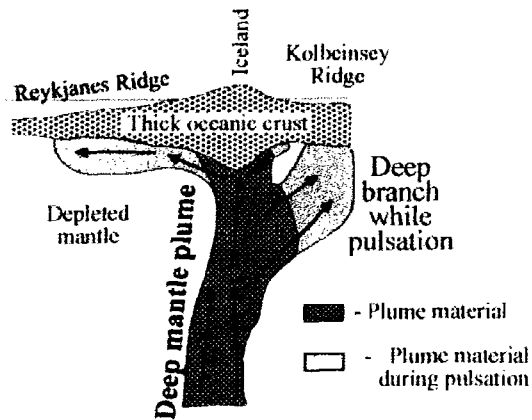


**Figure 5.8:** A schematic model for plume behavior beneath Iceland and the adjacent ridges. The time correlation between plume pulses at Iceland and ridge reorientation on the Kolbeinsey Ridge suggest that the two branches impinge the crust simultaneously. Lateral flow beneath the Reykjanes is inferred from the time lag between diachronous ridges. Reproduced from Abelson and Agnon (2001).



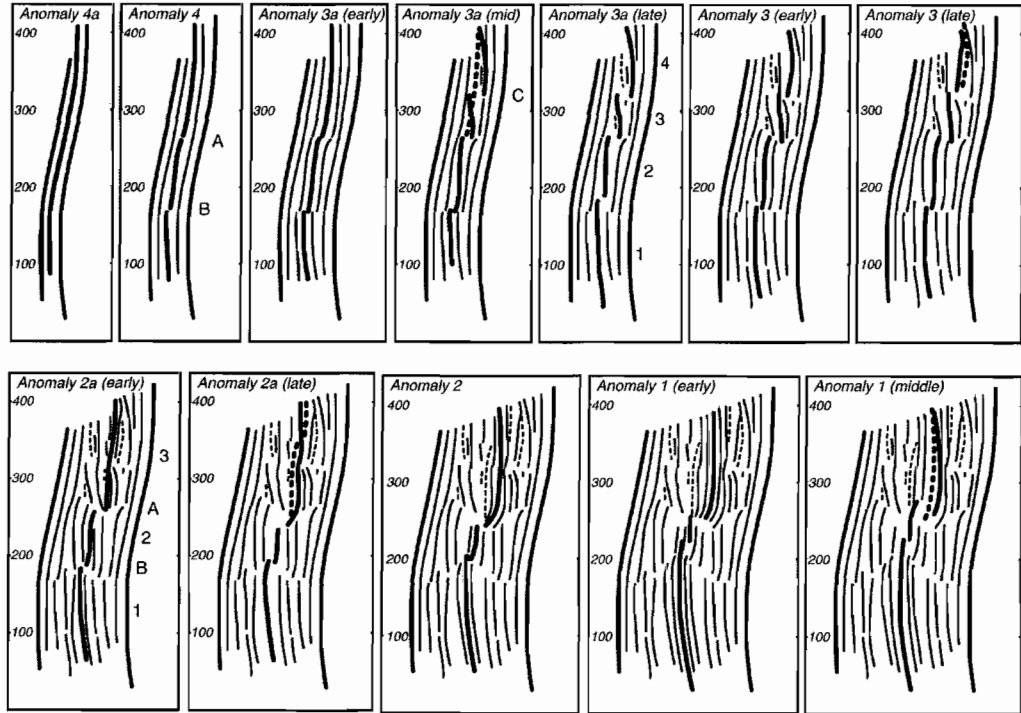


**Figure 5.9:** Tectonic reconstruction of the Kolbeinsey Ridge segments over the last 10 Ma. The bold lines show the active spreading axes. The outer, unsegmented lines represent magnetic anomaly 5. Lighter lines show positive magnetic anomalies. Dashed lines show abandoned spreading centers. Abelson and Agnon (2001) suggest that ridge geometry prior to anomaly 3a indicates a period of plume pulsation. The segment orientations from chron 2a to 2 are inferred to represent another period of increased plume influence on the Kolbeinsey. Reproduced from Applegate (1997) with additional interpretation from Abelson and Agnon (2001).

The high gravity anomaly recorded on my profile was formed at the ridge between ~5 - 9 Ma, encompassing the time that the segments of the Kolbeinsey Ridge began to rotate. Prior to the onset of segmentation around 7 Ma, the northern arm of the plume would have been able to influence the full length of the Kolbeinsey Ridge in a manner similar to the Reykjanes. After segmentation, the offset between the tips of ridge

segments may have served as a “valve”, slowing the plume material’s propagation north. This may also serve to regulate the thickness of crust generated on the northern Kolbeinsey segment. While the variable influence of the plume may explain some of the *p-wave* velocity anomalies, it is still unclear why there is not greater variability in crustal thickness on the northern Kolbeinsey segment and there is no consistent pattern linking free air gravity anomalies to changes in crustal thickness or crustal velocities.

Vogt (1971) proposed using the propagation rate of the V-shaped features down the ridge axis as a proxy for the apparent velocity of the down-axis component of asthenospheric flow. This propagation rate is estimated by  $v_a = S \cot \theta_R$ , where  $S$  is the half spreading rate and  $\theta_R$  is the angle between the V-shaped ridge and the spreading axis. This yields propagation velocities of 2.1 – 5.4 cm/yr and 2.2 – 6 cm/yr for the V-shaped ridges on the southern and northern Kolbeinsey Ridge segments, respectively (**Figure 5.10**). This value is much lower than the values estimated for the Reykjanes Ridge, with published estimates of 20 cm/yr (Vogt, 1971) and, more recently, between 8.7 and 28.2 cm/yr (Poore et al, 2009). The errors associated with this method are mainly due to the difficulty in determining exact locations in which to measure  $\theta_R$ , which may vary by as much as 15°. However, it is visibly clear that the angle between the V-shaped features and the spreading axis is much smaller on the Reykjanes Ridge than the Kolbeinsey Ridge, resulting in a much greater along axis distance. On the southern Kolbeinsey Ridge, the V-shaped ridge used to estimate asthenospheric flow corresponds to a positive gravity anomaly but it is not due to thickened crust. On the Reykjanes, Smallwood and

White (1998) show that the V-shaped gravity ridges are the result of changes in crustal thickness out to 7 Ma crust, supporting Vogt's hypothesis that the V-shaped features record the down axis migration of pulses of anomalously hot material from the plume. However, this relationship between the gravity anomalies and crustal thickness does not hold on either segment of the Kolbeinsey Ridge, suggesting the northward propagating V-shaped features are recording a different process. On the southern segment, the gravity anomaly appears to be the result of the northward migration of a non-transform offset between the tips of two ridge segments. On the northern segment, the processes recorded by the gravity anomalies are much less clear and appear to vary at each subsequent anomaly.

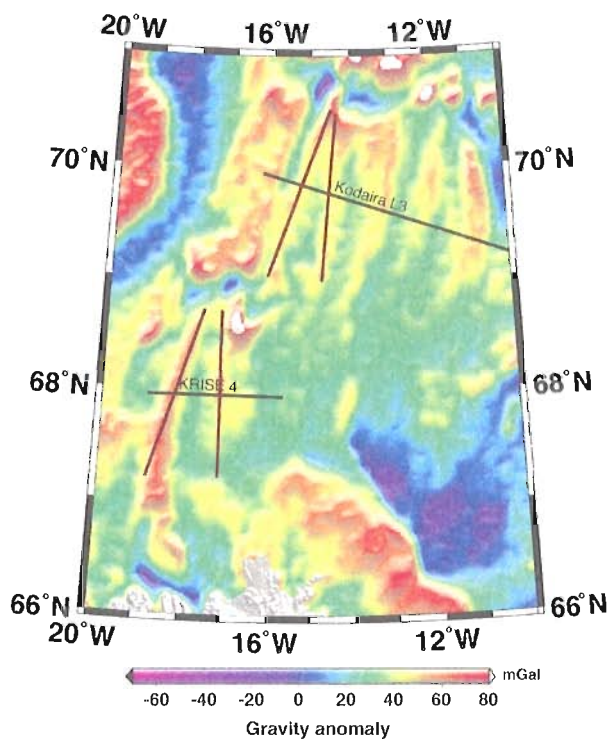


**Figure 5.10:** Gravity anomalies on the Kolbeinsey Ridge with the angle between the ridge and the V-shaped features highlighted. The red lines show the angles used to estimate the propagation rate of the process(es) recorded by the gravity anomalies. The estimated angles are  $18 \pm 7.5$  and  $17 \pm 7.5$  for the southern and northern segments, respectively. Gravity from Sandwell and Smith (1997).

#### **Section 5.4 Melt flux associated with crustal thickness**

Near the ridge axis, my crustal thickness of ~9.5 km is in agreement with the value estimated where KRISE Line 1 crosses Line 4. In order to estimate melt flux from this crustal thickness I used a full spreading rate of 19 mm/yr. The half spreading rate on the eastern side of the southern Kolbeinsey Ridge is closer to 8.5 mm/yr but the spreading is asymmetric; magnetic lineations indicate faster spreading occurring on the western side of the ridge (Mosar et al, 2002). I estimate a present day melt flux of  $1.8 \times 10^{-4} \text{ km}^2/\text{yr}$  per unit length of ridge. The thinnest crust of 7.8 km suggests that the melt flux at 4 Ma was  $1.5 \times 10^{-4} \text{ km}^2/\text{yr}$ , 17 % less than the current rate. For comparison, the estimated melt flux on the section of the Reykjanes Ridge described by Smallwood and White (1998) is  $2.02 \times 10^{-4} \text{ km}^2/\text{yr}$  for zero age crust and  $1.58 \times 10^{-4} \text{ km}^2/\text{yr}$  for crust aged 5 Ma. These values suggest that over the past 5 Ma, melt production on the Reykjanes has been ~6.0 - 6.5 % greater than that on the Kolbeinsey Ridge. The transects on the Reykjanes are 150 – 200 km further from the current plume location than KRISE Line 4; closer to the plume, the melt production rate on the Reykjanes Ridge may be even higher than that observed on the Kolbeinsey Ridge.

On the northern Kolbeinsey Ridge, Kodaira et al (1998) do not find variations in crustal thickness greater than ~1 km from the ridge east to ~18.5 Ma just west of the Jan Mayen Basin. Moving away from the ridge, increased sea floor depth is associated with a similar increase in Moho depth that is suggestive of a typical model of sea floor

subsidence with age, with an average thickness of ~8km. This suggests a fairly constant melt flux of  $\sim 1.5 \times 10^{-4} \text{ km}^2/\text{yr}$  over the last 10 Ma with a slight increase around 3.5 Ma.

### **Section 5.5 Non-transform offsets**

At the eastern end of my profile, the anomalously low *p-wave* velocities in the upper crust may indicate a thicker than typical layer of extrusive material. This has been observed in features on the flanks of the EPR that are identified as abandoned overlap basins that have been rafted off of spreading axes as the tips of ridge segments migrate along the ridge (Canales et al, 2003). These basins undergo significant post-emplacement microplate rotation (Hey et al, 2002), which may result in faults and fractures that persist into the mid- and lower crust, creating fluid pathways in what would otherwise be a relatively impermeable material. Another possible explanation for the slow velocities throughout the crustal section may be bookshelf faulting as seen between segments of a non-transform offset (NTO) (Hey et al, 2002; Wetzel et al, 1993). In this case, crustal blocks are sheared along parallel faults that are oblique to the direction of spreading. This results in rotation of the crustal blocks and extensive fracturing throughout the crust. I favor bookshelf faulting as the mechanism because I would expect to find an unaltered, or less altered, region in the middle if the mechanism was microplate rotation. Focal mechanisms from earthquakes in the present offset between ridge segments may help determine if the separation is accommodated by bookshelf faulting or microplate rotation; however there are few available for this region at this time.

My two magnetic models fit the observed signal fairly well out to the end of chron 3a, ~6.7 Ma. With the first model, using a combination of four different spreading rates, I am able to fit the data well to the end of the profile. This requires the use of a very slow spreading rate of 6.5 km/Ma for the eastern end of the profile. The other model, using solely the accepted spreading rate of 8.5 km/Ma for the last 10 Ma, does not fit the data at all beyond 6.7 Ma. This sudden change in apparent spreading rate occurs in conjunction with a decrease in signal strength from  $\sim \pm 1000$  nT to less than  $\pm 500$  nT. On both the northern Kolbeinsey Ridge and the Reykjanes Ridge, off-spreading axis magnetic anomalies had similar ranges of  $\sim \pm 1000$  nT out to chron 5, about 10 Ma. The peaks in the signal on the northern Kolbeinsey Ridge are consistent with a half spreading rate of 8.5 km/Ma for the last 5.5 Ma, with a rate of  $\sim 7.5 - 8$  km/Ma from 5.5 – 10 Ma. On the southern Kolbeinsey Ridge, the eastern end of the attenuated signal may be the result of post-emplacement fracture and rotation on the western limb of a northward propagating OSC or NTO. The fracturing would allow fluids to permeate the crust and may result in hydrothermal alteration of the magnetic layer, reducing the strength of the remanent magnetization. Although the apparent spreading rate at the eastern end of the profile is lower than the generally accepted rate for the southern Kolbeinsey Ridge, there have been rates as low as 7.5 km/Ma reported (Mosar et al, 2002). The mismatch in the signal further east may be because remanent magnetization of the magnetic layer there has been rotated from its emplacement orientation. As with the anomalously low *p-wave* velocities, this can be explained by rotation accommodated by rigid rotation or bookshelf faulting between the ends of two ridge segments. This sort of rotation would make the

magnetic anomalies wider and result in an increase in apparent spreading rate. I believe it is difficult to accurately match the magnetic anomalies to the correct chron due to rotation and the reduction in magnetic signal strength on this portion of the profile. On a regional magnetic map, magnetic anomaly 5 does not appear continuous across my profile (**Figure 5.11**). It is possible that the peak in magnetic signal that is correlated with anomaly 5 is actually the record of a later magnetic chron.

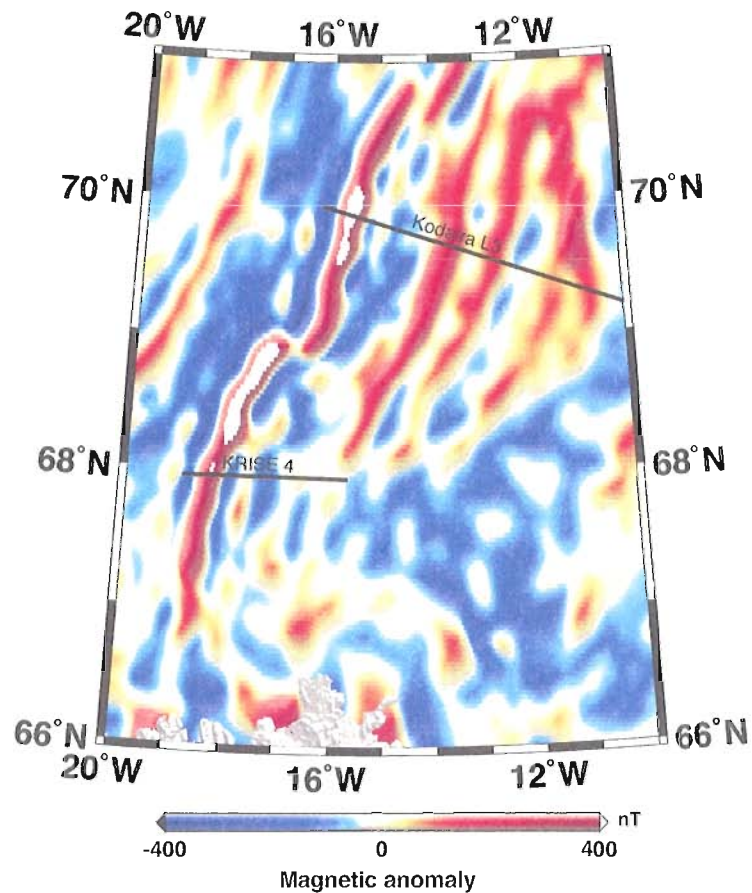


**Figure 5.11:** Magnetic anomalies on the Kolbeinsey Ridge. KRISE Line 4 and Kodaira et al's L3 are indicated with black lines (Maus et al, 2009)

Canales et al (2003) made a detailed study of the variations in crustal thickness and structure around the 9°03'N OSC on the East Pacific Rise (EPR). They find large negative velocity anomalies in the upper and mid-crust associated with three relict overlap basins, up to ~1 km/s slow at one basin. This large anomaly may be explained by a thicker than typical extrusive section due to ponding of lavas within the active overlap basin. As spreading continues, the overlap basins experience rotation which may cause fracturing in the mid to lower crust. These fractures can lower porosity throughout the crust and open pathways for water flow, which in turn, can result in lowered densities and lower velocities due to hydrothermal alteration. Additionally, Canales et al find the thickest off-axis crust just north of the trace of the southward migrating 9°03'N OSC. The dramatic increase in crustal thickness suggests that KRISE line 4 may cross the southern end of the relict overlap basin, where thicker crust might be expected for a northward propagating OSC. This interpretation is consistent with both magnetic map evidence (**Figure 5.11**) and with Applegate's (1997) assessment of the disrupted magnetic fabric in this region (**Figure 1.2**).



## CHAPTER VI

### CONCLUSION

Interaction between the Mid-Atlantic ridge and the Iceland mantle plume results in the generation of thicker than typical oceanic crust. Here I assess whether melt production along the Kolbeinsey ridge, north of Iceland, has varied with time in a similar way to at the Reykjanes ridge south of Iceland. A seismic refraction experiment on the southern Kolbeinsey ridge, 180 km north of the Icelandic coast, constrains temporal variations in crustal thickness generated at the ridge over the past 12 Ma. I observe significant undulations in Moho depth moving east away from the ridge. I estimate a Moho depth of ~10 km beneath the ridge, which decreases to a minimum depth of 7.8 km at a distance of 35 km from the ridge axis underlying 4 Ma crust. Continuing east, the crustal thickness appears to increase significantly to a depth of 12.5 km in 11 - 12 Ma crust. Although this crust does not appear to be isostatically supported, it is possible that the uppermost 1 – 2 km have been removed by glacial scour. Alternatively, the reflected arrivals supporting this depth could be from an upper mantle reflector rather than the

Moho. The gravity anomaly predicted using this crustal thickness is much lower here than the observed values.

The ~2.5 km decrease in crustal thickness from the spreading axis to 4 Myr old crust is similar to that observed on the Reykjanes Ridge by Smallwood and White (1998). However, unlike at the Reykjanes ridge, this thin crust does not correspond with deeper seafloor and a low free air gravity anomaly. Instead, the thin crust corresponds to slightly elevated bathymetry (~150 – 200 m) and elevated free air and Bouguer gravity anomalies. I suggest that the V-shaped gravity anomaly on the southern Kolbeinsey Ridge is the result of slightly elevated bathymetry due to faulting, combined with the closer proximity of the mantle to the seafloor due to thinner crust. On the northern Kolbeinsey Ridge, the gravity anomalies are not easily characterized. Near the ridge, the gravity anomalies correspond with bathymetry, however, elsewhere there is a mismatch between the locations of the gravity and bathymetric highs. The observation that the gravity ridges are not due to thickened crust, suggests that the gravity anomalies observed at the Kolbeinsey ridge are fundamentally different from those seen on the Reykjanes Ridge. On the southern Kolbeinsey Ridge, the region of thinned crust may record the location of the tip of a ridge segment 5.6 Ma. When associated with a gravity low, the higher velocity crust on the northern Kolbeinsey Ridge is inferred to reflect interaction with a compositionally different material supplied by a transient northern branch of the Iceland mantle plume.

The eastern 40 km of the profile have several interesting features: anomalously slow *p-wave* velocities throughout the crust, a rapid increase in apparent crustal thickness of nearly 5 km, and a 50 % reduction in magnetic signal coupled with an anomalously slow spreading rate. I argue that this crustal thickness is overestimated, particularly since it is not compensated by elevated bathymetry and has no associated gravity anomaly. I suggest that the reduced magnetic signal is due to rotation of the crust in this area and hydrothermal alteration of the rocks in the magnetized layer. This rotation may have also altered the width of the magnetic lineations, but it appears that a half spreading rate of  $\sim 7.5$  km/Ma is a more accurate estimation. *P-wave* velocities in this region are up to 13% slow in the upper crust and 5% slow in the lower crust, consistent with higher porosity and/or hydrothermal alteration due to faulting throughout the crust. Faulting may have allowed fluids to permeate into the upper mantle as well, with the subsequent alteration diminishing the transition from crust to mantle and effectively removing the Moho reflector. The deeper reflected arrivals may originate from a density contrast within the upper mantle, perhaps the base of the alteration zone. This would also resolve the disparity between the seismically derived crustal thickness and the lack of accompanying topography. I interpret this combination of characteristics to be the result of post-emplacment rotation of the oceanic crust between the tips of two offset ridge segments, either by microplate rotation or bookshelf faulting. In either case, the ridge offsets tend to be unstable features, with the location of the break between ridge segments migrating along the ridge through time. As this happens, the overlap basin or zone of bookshelf faulting is cut off from the supply of new oceanic crust and is moved off axis with

continued spreading, resulting in a V-shaped “wake” marking the location of the ridge offset through time.

The V-shaped gravity features on the Reykjanes Ridge, and the variations in crustal thickness that they are inferred to represent, have been used to create models of plume-ridge interaction (Ito and Jin, 1995; Ito, 2001; Vogt, 1971). Smallwood and White (1998) and Poore et al (2009) both find good correlation between bathymetry and gravity anomalies in the proximity of the ridge. This correlation breaks down with distance from the spreading center and Poore et al (2009) find a significant mismatch in 8 – 12 Ma crust in several locations on both sides of the Reykjanes. A similar discrepancy between gravity and bathymetry is found on the Kolbeinsey Ridge. On the southern segment, the high gravity anomaly may be completely explained by seafloor and Moho topography. The northern segment is much more complicated and the source of at least two of the gravity ridges remains unclear. Additional seismic studies on the both the Reykjanes and Kolbeinsey Ridges would help clarify the structure of the V-shaped gravity ridges and their relationship to temporal variations in plume-ridge interaction north and south of Iceland.

## REFERENCES

- Abelson, M., and Agnon, A. (2001). Hotspot activity and plume pulses recorded by geometry of spreading axes. *Earth and Planetary Science Letters*, 189, 31-47.
- Albers, M. and Christensen, U.R., (2001). Channeling of plume flow beneath mid-ocean ridges, *Earth and Planetary Science Letters*, 187, 207-220.
- Applegate, B., (1997). Modes of axial reorganization on a slow-spreading ridge: The structural evolution of Kolbeinsey Ridge since 10 Ma, *Geology*, 25(5), 431-434.
- Brocher, T., (2008). Key Elements of regional seismic velocity models for long period ground motion simulations, *Journal of Seismology*, 12, 217-221.
- Canales, J.P., Detrick, R.S., Lin, J., and Collins, J.A., (2000). Crustal and upper mantle seismic structure beneath the rift mountains and across a nontransform offset at the Mid-Atlantic Ridge (35°N), *Journal of Geophysical Research*, 105, 2699-2719.
- Canales, J.P., Detrick, R.S., Toomey, D.R., and Wilcock, W.S.D., (2003). Segment scale variations in the crustal structure of 150-300 kyr old fast spreading oceanic crust (East Pacific Rise, 8°15'N - 10°5'N) from wide-angle seismic refraction profiles, *Geophysical Journal International*, 152, 766-794.
- Carbotte, S.M., and Scheirer, D.S., (2004). Variability of ocean crustal structure created along the global mid-ocean ridge. In E.E. Davis and H. Elderfield (eds.) *Hydrogeology of the Oceanic Lithosphere*, (pp 59-107). Cambridge: Cambridge University Press.
- Carlson, R.L., and Herrick, C.N., (1990). Densities and Porosities in the Oceanic Crust and Their Variations With Depth and Age, *Journal of Geophysical Research*, 95, 9153-9170.
- Carlson, R.L., and Raskin, G.S., (1984). Density of the ocean crust, *Nature*, 311(5986), 555-558.

- Christeson, G.L., Kent, G.M., Purdy, G.M., and Detrick, R.S., (1996). Extrusive thickness variability at the East Pacific Rise, 9°-10°: Constraints from seismic techniques, *Journal of Geophysical Research*, *101*, 2859-2873.
- Christeson, G.L., Purdy, G.M., Fryer, G.J., (1992). Structure of young upper crust at the East Pacific Rise near 9°30'N, *Geophysical Research Letters*, *19*(10), 1045-1048.
- Condie, K.C., (2001). *Mantle Plumes and Their Record in Earth History*. Cambridge: Cambridge University Press.
- Creager, K.C., and Dorman, L.M., (1982). Location of Instruments on the Seafloor by Joint Adjustment of Instrument and Ship Positions, *Journal of Geophysical Research*, *87*, 8379-8388.
- Crosby, A.G., and McKenzie, D., (2009). An analysis of young ocean depth, gravity and global residual topography, *Geophysical Journal International*, *178*, 1198-1219.
- Forsyth, D.A., Morel-à-l'Huissier, P., Asudsen, I., and Green, A.G., (1986). Alpha Ridge and Iceland: Products of the same plume?, *Journal of Geodynamics*, *6*, 197-214.
- Haase, K.M., Devey, C.W., and Wieneke, M., (2003). Magmatic processes and mantle heterogeneity beneath the slow-spreading northern Kolbeinsey Ridge segment, North Atlantic, *Contributions to Mineral Petrology*, *144*, 428-448.
- Hardarson, B.S., Fitton, J.G., Ellam, R.M., and Pringle, M.S., (1997). Rift relocation – a geochemical and geochronological investigation of a palaeo-rift in northwest Iceland, *Earth and Planetary Science Letters*, *153*, 181-196.
- Hey, R.N., Martinez, F., Diniega, S., Naar, D.F., Francheteau, J. and the Pito93 Scientific Team, (2002). Preliminary attempt to characterize the rotation of seafloor in the Pito Deep area of the Easter Microplate using a submersible magnetometer, *Marine Geophysical Researches*, *23*, 1-12.
- Hooft, E.E.E., Detrick, R.S., Toomey, D.R., Collins, J.A., and Lin, J., (2000). Crustal thickness and structure along three contrasting spreading segments of the Mid-Atlantic Ridge, 33.5°-35°N, *Journal of Geophysical Research*, *105*, 8205-8226.
- Hooft, E.E.E., Brandsdóttir, B., Mjelde, R., Shimamura, H., and Murai, Y., (2006). Asymmetric plume-ridge interaction around Iceland: The Kolbeinsey Ridge Iceland Seismic Experiment, *Geochemistry, Geophysics, Geosystems*, *7*(5).
- Ito, G., and Lin, J., (1995). Oceanic spreading center-hotspot interactions: Constraints from along-isochron bathymetric and gravity anomalies, *Geology*, *23*(7), 657-660.
- Ito, G., (2001). Reykjanes 'V'-shaped ridges originating from a pulsing and dehydrating mantle plume, *Nature*, *411*, 681-684.

- Johnson, G.L., Southall, J.R., Young, P.W., and Vogt, P.R., (1972). Origin and structure of the Iceland Plateau and Kolbeinsey Ridge, *Journal of Geophysical Research*, 77(29), 5688-5696.
- Jones, S.M., White, N., and MacLennan, J., (2002). V-shaped ridges around Iceland: Implications for spatial and temporal patterns of mantle convection, *Geochemistry, Geophysics, Geosystems*, 3(10).
- Kharin, G.S., (1991). Igneous Activity and the Evolution of the Atlantic Ocean's Lithosphere, *Oceanology*, 31(5), 600-606.
- Kharin, G.S., (1980). The Basalts of the Kolbeinsey Submarine Ridge (Norwegian-Greenland Basin), *Oceanology*, 20(1), 50-55.
- Kodaira, S., Mjelde, R., Gunnarsson, K., Shiobara, H., and Shimamura, H., (1997). Crustal structure of the Kolbeinsey Ridge, North Atlantic, obtained by use of ocean bottom seismographs, *Journal of Geophysical Research*, 102, 3131-3151.
- Kodaira, S., Mjelde, R., Gunnarsson, K., Shiobara, H., and Shimamura, H., (1998). Evolution of oceanic crust on the Kolbeinsey Ridge, north of Iceland, over the past 22 Myr, *Terra Nova*, 10, 27-31.
- Korenaga, J., Holbrook, W.S., Kent, G.M., Kelemen, P.B., Detrick, R.S., Larsen, H.-C., Hopper, J.R., and Dahl-Jensen, T., (2000). Crustal structure on the southeast Greenland margin from joint refraction and reflection seismic tomography, *Journal of Geophysical Research*, 105, 21,591-21,614.
- Litvin, V.M., Suzyumov, A.Y., and Mirlin, Y.G., (1980). Results of magnetic and geomorphic surveys of the southern part of the Kolbeinsey Ridge, *Doklady Akad. Nauk SSSR*, 240, 230-233.
- Martínez, F., Hey, R.N., Johnson, P.D., (1997). The East ridge system 28.5-32°S East Pacific rise: Implications for overlapping spreading center development, *Earth and Planetary Science Letters*, 151, 13-31.
- Maus, S., Barckhausen, U., Berkenbosch, H., Bournas, N., Brozena, J., Childers, V., Dostaler, F., Fairhead, J. D., Finn, C., von Frese, R. R. B., Gaina, C., Golynsky, S., Kucks, R., Lühr, H., Milligan, P., Mogren, S., Müller, D., Olesen, O., Pilkington, M., Saltus, R., Schreckenberger, B., Thébault, E., and Caratori Tontini, F. (2009). EMAG2: A 2-arc-minute resolution Earth Magnetic Anomaly Grid compiled from satellite, airborne and marine magnetic measurements, *Geochemistry, Geophysics, Geosystems*, under review.
- Mertz, D.F., Devey, C.W., Todt, W., Stoffers, P., and Hoffman, A.W., (1991). Sr-Nd-Pb isotope evidence against plume-asthenosphere mixing north of Iceland, *Earth and Planetary Science Letters*, 107, 243-255.

- Mosar, J., Lewis, G., Torsvik, T.H., (2002). North Atlantic sea-floor spreading rates: implications for the Tertiary development of inversion structures of the Norwegian-Greenland Sea, *Journal of the Geological Society, London*, 159, 503-515.
- Moser, T.J., (1991). Shortest path calculations of seismic rays, *Geophysics*, 56, 59-67.
- Parker, R.L., (1973). The Rapid Calculation of Potential Anomalies, *Geophys. J. R. astr. Soc.*, 31, 447-455.
- Poore, H.R., White, N., Jones, S., (2009). A Neogene chronology of Iceland plume activity from V-shaped ridges, *Earth and Planetary Science Letters*, 283, 1-13.
- Ritsema, J., van Heijst, H.J., and Woodhouse, J.H., (1999). Complex Shear Wave Velocity Structure Imaged Beneath Africa and Iceland, *Science*, 286, 1925-1928.
- Sæmundsson, K., (1979). Outline of the geology of Iceland, *Jökull*, 29, pp. 7-28.
- Sæmundsson, K., (1978). Fissure swarms and central volcanoes of the neovolcanic zones of Iceland. In Bowes, D.R., and Leake, B.E. (eds.) *Crustal Evolution in northwestern Britain and adjacent regions*, *Geological Journal special issue*, 11, 415-432.
- Sæmundsson, K., (1974). Evolution of the axial rifting zone in northern Iceland and the Tjörnes fracture zone, *Geological Society of America Bulletin*, 85, 495-504.
- Schilling, J.-G., Kingsley, R., Fontignie, D., Poreda, R., and Xue, S., (1999). Dispersion of the Jan Mayen and Iceland mantle plumes in the Arctic: A He-Pb-Nd-Sr isotope tracer study of basalts from the Kolbeinsey, Mohns, and Knipovich Ridges, *Journal of Geophysical Research*, 104, 10,543-10,569.
- Schilling, J.-G., (1991). Fluxes and excess temperatures of mantle plumes inferred from their interaction with migrating mid-ocean ridges, *Nature*, 352, 397-403.
- Schilling, J.-G., (1973). Iceland mantle plume: geochemical study of Reykjanes Ridge, *Nature*, 242, 565-571.
- Schouten, J., (1971). A Fundamental analysis of magnetic anomalies over oceanic ridges, *Marine Geophysical Researches*, 1, 111-144.
- Smith, W. H. F. and Sandwell, D., (1997). Global seafloor topography from satellite altimetry and ship depth soundings, *Science*, 277, 1956-1962
- Shaw, P.R., (1994). Age variations of oceanic crust Poisson's ratio: inversion and a porosity evolution model, *Journal of Geophysical Research*, 99, 3057-3066.
- Smallwood, J.R., and White, R.S., (1998). Crustal accretion at the Reykjanes Ridge, 61°-62°N, *Journal of Geophysical Research*, 103, 5185-5201.



Smallwood, J.R., and White, R.S., (2002). Ridge-plume interaction in the North Atlantic and its influence on continental breakup and seafloor spreading. In Jolley, D.W. and Bell, B.R. (eds.) *The North Atlantic Igneous Province: Stratigraphy, Tectonic, Volcanic and Magmatic Processes* (pp. 15-37). London: Geological Society, London, Special Publications, 197.

Talwani, M., and Endholm, O., (1977). Evolution of the Norwegian-Greenland Sea, *Geological Society of America Bulletin*, 8, 969-999.

Toomey, D.R. and Foulger, G.R., (1989). Tomographic Inversion of Local Earthquake Data From the Hengill-Grensdalur Central Volcano Complex, Iceland, *Journal of Geophysical Research*, 94, 17,497-17,510.

Trønnes, R.G. (2002). Field trip: Introduction. Geology and geodynamics of Iceland. In: S. Planke (ed.) *Iceland 2002 – Petroleum Geology Field Trip Guide (prepared for Statoil Faroes License Groups by Volcanic Basin Petroleum Research, Nordic Volcanological Institute and Iceland National Energy Authority)*, (pp. 23-43).

Turcotte, D.L. and Schubert, G., (2002). *Geodynamics 2<sup>nd</sup> ed.*, Cambridge: Cambridge University Press.

Vink, G.E., (1984). A Hotspot model for Iceland and the Vøring Plateau, *Journal of Geophysical Research*, 89, 9499-9959.

Vogt, P.R., (1971). Asthenosphere motion recorded by the ocean floor south of Iceland, *Earth and Planetary Science Letters*, 13, 153-160.

Weir, N.R.W., White, R.S., Brandsdóttir, B., Einarsson, P., Shimamura, H., Shiobara, H., and the RISE Fieldwork Team, (2001). Crustal structure of the northern Reykjanes Ridge and Reykjanes Peninsula, southwest Iceland, *Journal of Geophysical Research*, 106, 6347-6368.

Wetzel, L.R., Wiens, D.A., and Kleinrock, M.C., (1993). Evidence from earthquakes for bookshelf faulting at large non-transform ridge offsets, *Nature*, 362, 235-237.